6. THERMAL HYDROLOGIC MEASUREMENTS AND ANALYSIS

6.1 THERMAL HYDROLOGIC MEASUREMENTS

The thermal hydrologic measurements include the determination of the spatial distribution and the temporal variation of the bulk air permeability and the moisture content in the block. Both single-hole injection and cross-hole flow measurements were used to determine the bulk air permeability. Tracer tests were also conducted to determine the flow paths in the block. The air permeability was determined before the heating and at the end of the heating phase. The moisture content was also determined before the heating, during the heating, and during the natural cooling phases. Both the pre-heat and in-heat measurements are presented in this section.

6.1.1 Bulk Air Permeability and Flow Path Measurements

6.1.1.1 Pre-heating Permeability Measurements

6.1.1.1.1 LLNL Single Hole Permeability Test

To estimate bulk permeability, air-injection tests were conducted after the first vertical borehole (N1, as shown in Figure 2-7 of Wilder, et al. [1997]) was drilled. (Note that N1 later became TH1, as shown in Figure 3-7, after the installation of instruments in the block.) Curve D in Figure 6-1 shows the air permeability as a function of depth. Most of the sampled depths have a permeability greater than 10^{-11} cm^2. It should be noted that the permeability is dominated by the fractures that intersect the injection borehole. Because of the high fracture density in the block, the bulk permeability is likely to be more homogeneous.

Wang and Ahlers (1996) compared the results of the air-permeability tests with those conducted within the ESF for the Single Heater Test (SHT). They noted that the permeability results were more heterogeneous for the LBT than for the SHT (see Figure 2-18 of the LBT Status Report). As they noted, it is possible that the near-surface exposure does not generate sufficient stress to close up the larger fractures. In contrast, at the repository level, the stress may be sufficiently large that the apertures of the fractures would tend to be reduced. It is of interest to note that the LBT rock in general is much tighter than that of the SHT, but the LBT's more permeable zones are more permeable than those of the SHT. A possible implication is that after the air permeability tests were completed and the block was isolated by saw-cut and excavation, these fractures may have opened more, although the stresses near the surface may be so low that isolation of the block would have little effect.

As shown in Figure 6-1, permeability tests conducted in 1997 (curve B) prior to instrumentation is not much different from the pre-cut measurement in 1993 (curve D), and therefore do not support the hypothesis of further opening of fractures after the block was isolated.

6.1.1.1.2 Lawrence Berkeley National Laboratory Cross Hole

Air-injection tests were conducted, after all instruments were installed and the boreholes were sealed (except the heater boreholes and hydrology boreholes, which had packers in them), with injections of a gas tracer at a controlled flow rate into packed borehole intervals. Cross-hole transient pressure responses were simultaneously measured in surrounding boreholes. Figure 6-2

shows the heterogeneous pneumatic permeability variation along five heater boreholes. High permeability zones were present near the block boundaries. In the block interior, two heater boreholes (EH-2 and EH-3) penetrated low-permeability zones in the first half of the boreholes. The heterogeneous permeability variation within the block indicates that the heater-induced vapor-flow processes can be very different in different zones in the block, with vapor flowing easily near the northern and eastern boundaries and in the back (western side) of the block away from the bottom of the boreholes. A "hard core" with low permeability and low vapor convection exists southeast, off center in the block.

Figure 6-3 illustrates the air-permeability variations along three horizontal hydrologic monitoring boreholes. Two hydrologic boreholes are located on the western side of the block with WH1 1.5 m (5 ft) and WH2 0.5 m (1.5 ft) above the heater plane. Two sets of tests were conducted at WH1, as shown in Figure 6-3. The third hydrologic borehole NH1 from the north face is 0.3 m (1 ft) above the heater plane. The air-permeability variations along these three hydrologic monitoring boreholes do not exhibit the high permeability (10^{-11} to 10^{-10}m^2 or 10 to 100 darcy) leaky boundary effects observed in some of the heater boreholes. Localized tight zones with air-permeability values one to two orders of magnitude lower than the average permeability in the 10^{-12} m^2 (1 darcy) range were identified along the boreholes. The horizontal permeability profiles in Figure 6-3 supplement the vertical permeability profile previously measured along vertical borehole TH1 (Wilder et al. 1997).

6.1.1.1.3 Lawrence Berkeley National Laboratory Trace Test

Tracers were released in the heater boreholes at different intervals and detected at other locations above and below the heater plane. Figure 6-4 shows the tracer breakthrough detected at borehole WH1, 1.52 m above the heater plane and 3.35 m above the ground. The tracers were released from both the middle interval (interval 3) of borehole EH-2 south of the block center and borehole EH-5 near the northern boundary. Borehole EH-5-3 has the highest permeability measured in the block. Potential leakage through the north shield could have contributed to the high value. Compared to the tracers released at EH-2-3 near the center of the block, the tracer released at this interval moved easily to borehole WH1. Both breakthrough curves also had long tails, indicating that many other pathways in the block contributed to the tracer transport at different rates. The tracer breakthrough results substantiated the pneumatic test results with respect to high permeability zones enhancing flow and transport through heterogeneous, fractured rock media in the block. Comparison of TH analyses and heater test results can assess the importance of block-scale heterogeneity in determining near-field, heater-induced impacts.

6.1.1.2 Post-Heating Air Permeability Measurement

Air injection permeability measurements along Borehole TH1 were repeated in February 1998 while the block was still heated, shortly before the cool-down phase started. The purpose was to observe any effects of heating on rock fracture permeability in the block by comparing the hot permeability profile with the preheating profile measured after the block was constructed 1997. As with the previous tests, air was injected into packed-off sections of the borehole, and bulk permeability of the rock adjacent to the packed-off section was calculated from the gas pressure and temperature measured in the test zone, ambient pressure, and the mass flow rate of injected air. Air viscosity and density in the calculations were adjusted for temperature. The hot

permeability profile was limited to a depth of 3.29 m, because blockage in the borehole prevented deeper penetration by the packer probe. The preheating permeability profile went down to a depth of 4.72 m.

Figure 6-5 compares the preheating and hot permeability profiles. The figure shows substantially higher permeability in the hot rock at depths above 1.83 m. The greatest difference occurs at a depth of 1.22 to 1.3 m, where the hot permeability is about two orders of magnitude greater. From 1.83 m to 3.17 m, differences between the two permeability profiles are much smaller. Higher permeability values in the hot rock closer to the top of the block may suggest that movement along fractures, due to thermal expansion, was probably more pronounced in that region. Such movement could reopen healed fractures and cause aperture increases in existing fractures. This is in agreement with the deformation of the block observed during the test (see Section 7 for details).

6.1.2 Moisture Content Measurements

The moisture content in the block was determined by using ERT and neutron logging. Neutron logging provides very accurate determination of the moisture content within a region of about 10 cm radius distance from a borehole. The ERT provides 2-D distribution of the moisture content with less accuracy. The two methods were used to complement each other.

6.1.2.1 Electrical Resistance Tomography

6.1.2.1.1 ERT Methodology

ERT is a geophysical imaging technique that can be used to map subsurface resistivity (Daily and Owen 1991). The ERT measurements consist of a series of voltage and current measurements from buried electrodes using an automated data collection system. The data are then processed to produce electrical resistivity tomographs. ERT was proposed independently by Henderson and Webster (1978) as a medical imaging tool and by Lytle and Dines (1978) as a geophysical imaging tool. The technique has been actively developed for medical imaging (Isaacson 1986; Barber and Seager 1987; Yorkey et al. 1987). Early adaptations of the technique to the field of geophysics were by Pelton et al. (1978), Dines and Lytle (1981), Tripp et al. (1984), Wexler et al. (1985), Oldenburg and Li (1994), Sasaki (1992), Daily and Owen (1991), and LaBrecque et al. (1996a).

Here we describe briefly some of the important features of the 2-D algorithm used for ERT. The algorithm (see LaBrecque et al. 1996b) solves both the forward and inverse problems. The forward problem is solved using a finite element technique in two dimensions. The inverse problem implements a regularized solution that minimizes an objective function. The objective of the inverse routine is to minimize the misfit between the forward modeling data and the field data, and a stabilizing functional of the parameters. The stabilizing functional is the solution roughness. This means that the inverse procedure tries to find the smoothest resistivity model that fits the field data to a prescribed tolerance. Resistivity values assigned in this way to the finite element mesh constitute the ERT image. Although the mesh is of a large region around the electrode arrays, only the region inside the ERT electrode array is used in the calculations of

moisture content and reported here, because the region outside the array is poorly constrained by the data.

To calculate the changes in the rock's electrical resistivity we compared a data set obtained after heating started, and a corresponding data set obtained prior to heating. One may consider subtracting, pixel by pixel, images from these two different conditions. However, this approach could not be used because the resistivity structure is three-dimensional. The finite element forward solver cannot generate a model that will fit the data, so the code chooses a solution with a poor fit. Our experience is that these effects can be reduced by inverting the quality:

$$\frac{r_a}{r_b} \times r_h \qquad \text{(Eq. 6-1)}$$

where:

r_a is the measured transfer resistance after heating started,
r_b is the transfer resistance before heating, and
r_h is the calculated transfer resistance for a model of uniform resistivity.

This approach tends to reduce the effects of anomalies that do not satisfy the 2-D assumptions of the resistivity model because the 3-D effects tend to cancel in the ratio because they are contained in both terms r_a and r_b.

6.1.2.1.2 Changes in Moisture Content

Resistivity of the rock is influenced by changes in moisture content, porosity, cation exchange capacity, solutes in the pore water, and temperature. In the following analysis we assume that only moisture content and temperature are important. An increase in temperature or moisture causes a resistivity decrease. However, near the heater there may be regions where the increasing temperature and decreasing pore water resistivity is opposed by the rockmass drying, which increases the resistivity. Our goal in this section is to use the images of resistivity change near the heater, along with the measured temperature field and what is known of initial conditions, in the rockmass to estimate moisture change during heating.

To estimate moisture content changes, we need to account for both the effects of temperature, measured at many points by temperature sensors, and resistivity changes, measured by ERT. This is possible by either using laboratory data establishing the relations among moisture, temperature, and resistivity or by using a suitable model of electrical conduction in porous media. Roberts and Lin (1997b) have published data on the resistivity of Topopah Spring tuff as a function of moisture content. There is, however, limited (unpublished) data on temperature dependence (only below 95°C) so that direct use of this data is not possible.

On the other hand, Waxman and Thomas (1974a,b) describe a model for electrical conduction in partially saturated shaly sands typical of oil reservoirs (intended for oil field data), which accounts for conduction through the bulk pore water as well as conduction through the electrical double layer near the pore surface (see also Vinegar and Waxman 1984). This model can predict temperature dependence of the resistivity, but several of the model parameters are empirically

determined and not available for tuff. Roberts and Lin (1997b) suggest that the Waxman model provides reasonably good estimates of resistivity for saturations greater than 20%. For saturations less than 20%, their data shows that the Waxman Smits model substantially underpredicts the resistivity. We will use this model to account for the temperature effects on the resistivity changes and to estimate changes in rock saturation.

Waxman and Thomas (1974a,b) begin with a parallel circuit model for conductance:

$$C = \frac{1}{F^*}(C_W + BQ_v) \qquad \text{(Eq. 6-2)}$$

where:

C is the conductivity or 1/R where R is the resistivity,
F^* is the formation factor or f^{-m} where f is the porosity and m the porosity exponent,
C_W is the pore water conductivity,
B is the equivalent conductance of counterions on the double layer, and
Q_V is the effective concentration of exchange cations.

The first term represents conductance through the bulk pore water while the second term is the conductance along the double layer. This expression can be modified for partially saturated media by realizing that the first term is just Archie's equation and $Q/S = Q_V$ where S is the fractional saturation. In terms of resistivity, Equation 6-2 can be re-written as:

$$R = \frac{R_W{}^{-m} S^{1-n}}{S + R_W BQ} \qquad \text{(Eq. 6-3)}$$

where:

n is approximately 2, the saturation index in Archie's modified equation, and R_W is the water resistivity.

Waxman and Thomas (1974a,b) reported results that suggest that *m* is approximately equal to *n*. When $R_WBQ >> S$, the electrical double layer is the primary conduction pathway. When $R_WBQ << S$, the primary conduction pathway is through the open pore space.

We can use Equation 6-3 in ratio form in order to calculate resistivity changes in the form of resistivity ratios. When the primary conduction pathway is the through the water in the open pore space, the resistivity ratio can be calculated as:

$$\frac{R_a}{R_b} = \frac{R_{w,a}}{R_{w,b}}\left(\frac{S_b}{S_a}\right)^2 \qquad \text{(Eq. 6-4)}$$

where:

R_b and R_a are the resistivities before and after heating started,
$R_{w,b}$ and $R_{w,a}$ are the water resistivities before and after heating, and
S_b and S_a are the saturations before and after heating started; we will refer to this case as model 1.

This equation implies that the temperature dependence of the resistivity change is proportional to the change in water resistivity caused by temperature increases.

When the primary conduction pathway is through the electrical double layer, the ratio form of Equation 6-3 simplifies to:

$$\frac{R_a}{R_b} = \frac{S_b}{S_a}\frac{B_b}{B_a} \qquad \text{(Eq. 6-5)}$$

where:

B_b and B_a are the equivalent conductances of counter-ions in the electrical double layer.

We will refer to this case as model 2. This equation implies that the temperature dependence of the resistivity ratio is caused by changes in counter-ion conductance due to temperature changes. Comparing Equations 6-4 and 6-5, we see that the resistivity changes caused by saturation changes are largest for model 1 where the primary conduction pathway is through the pore space. We note that neither of these two models accounts for changes in water resistivity caused by rock/water chemical interactions. If chemical reactions cause changes in the concentration or types of ions in the water, or change the porosity due to mineral precipitation or dissolution, the estimated saturation changes will be in error.

We used the available temperature data to construct temperature maps along each ERT image plane. It is necessary to have a reliable temperature measurement for each area (each tomograph pixel) where we wish to calculate the saturation change.

The ERT images provide a measure of change from baseline resistivity R (through the resistivity ratio). Equations 6-4 and 6-5 can be used to relate electrical resistivity changes to changes in saturation when the temperatures are known and the temperature dependence of R_W and B can be calculated.

Calculation of changes in volumetric water content requires rock porosity and initial saturation values. Initial values of block saturation were calculated from neutron logs in four boreholes. The water saturation from all of these holes agrees and shows values ranging from about 60% to 90% by pore volume (Wilder et al. 1997). We assume a uniform initial saturation of 75% and a porosity of 12%.

Since the magnitude of RwBQ (see Equation 6-3) is changing in space and time, we have chosen to estimate the changes in saturation by using both model 1 and 2. This approach should provide bounds to the domain of possible saturations that may be present. However, there is some reason

to believe that welded tuff should show behavior closer to model 2 than to model 1. This can be seen by assuming average values of cation exchange capacity for welded tuff of about 3 meq/100 g, porosity of 0.10 (porosity is used to calculate Q), and Rw =39 ohm m at 25°C (resistivity of J-13 water). For these values RwBQ is about 23 at 25°C, and it increases with temperature. Since S is bounded by 0.0 and 1.0, then RwBQ is >> S, and the primary pathway for conduction is the electrical double layer. However, if the cation exchange capacity, porosity, or water resistivity varied significantly across the ERT image plane, it is possible that model 1 results are closer to reality.

In fact, we believe that model 1 is more representative of the rock mass for two reasons. First, the saturation estimates based on this model are in better agreement with those of the neutron log where that data are available. Second, the saturation estimates based on model 2 occasionally predict S> 1.0, which, of course, are nonphysical.

6.1.2.1.3 ERT Results

ERT data were taken from four planner arrays in the block before the heaters were turned on. Two horizontal planes of electrodes were arranged on the surface, azimuthally around the block. One plane was approximately 1.25 m above the heater plane and the other was approximately 1.25 m below the heater plane. The two other planes were vertical, dividing the block into four quadrants. The vertical planes were sampled from electrode arrays on the side of the block and a single vertical array at the center of the block. The electrode arrangement is shown in Figure 6-6.

At the intersection of these ERT planes, there should be agreement, and this is the case for the vertical planes because they share a common electrode array along that intersection. Such agreement is not very good for the intersection of the vertical and horizontal planes. Complete agreement cannot be expected in these cases for two reasons.

First, the spatial distribution of sensitivity and resolution is different for the vertical and horizontal planes because of the difference in how they are sampled by the electrodes. Therefore, the two planes will tend to resolve features differently. The common electrode array in the vertical planes produces good resolution where they intersect, and this is why they tend to agree. In general, two-sided sampling, as in the vertical planes, leaves a low-sensitivity region along the top and bottom. On the other hand, the all-around sampling of the horizontal planes leaves a low-sensitivity region in the center, where we shall see that agreement with the vertical planes is poorest.

Second, in all of these images we are trying to reconstruct a 3-D target using a model that is strictly 2-D. This means that the ERT algorithm finds the best finite element model for the resistivity structure of the block that fits the data within a given criterion. Unfortunately, it can only choose from models where the resistivity is constant orthoganal to the image plane. It picks the best model, but it cannot be the correct model. That model chosen for two different planes will be different, especially if the planes are perpendicular as the vertical and horizontal planes are here.

We note here that some of the resistivity images reconstructed late in the experiment (and the moisture changes inferred from them) are questionable because of the sparse data. As the

rockmass dehydrated and the resistivity increased dramatically, the data quality declined. Fewer usable data results in a poorly constrained reconstruction that might look smeared or washed out. This is particularly noticeable in the vertical planes beginning early in 1998.

The results of interpreting the changes in the resistivity tomographs in terms of moisture content changes are shown in Figures 6-7 and 6-8. Blank image planes indicate data that did not converge to an ERT solution or where no data were collected. The 2-D orthogonal planes shown in Figure 6-7 and 6-8 don't provide a full description of the 3-D block, but they do show considerable detail that would be otherwise unavailable with only point temperature data or even with one-dimensional neutron data.

We will first discuss the results in terms of conceptual behavior—rock drying, condensate accumulation in fractures, and loss of condensate out of the block. The goal is to determine the impact that heterogeneieties (such as fractures) have on the distribution and fate of water in the block. We begin with a discussion of the horizontal planes.

6.1.2.1.3.1 Horizontal Planes

The obvious result shown in the horizontal planes (see Figure 6-7) is that changes in moisture content initially are very small and increase in magnitude and extent as the test proceeds. Notice, however, that there are some asymmetries between the two cases. Through June 25, 1997 (117 days into heating) the upper plane (plane above the heater elevation) shows significantly less change from initial conditions than the lower plane. As early as April 22, 1997 (53 days into heating), a strong and compact wetting anomaly appears below the heaters. It remains visible at May 22, 1997 (30 days later) but then disappears from subsequent images until November 19, 1997, when it reappears and persists to the end of the test on March 19, 1998. We believe that this feature resulted from a major fracture, or fracture system, intersecting the image plane and that in April and May condensate from the heated region found its way to this fracture and moved by gravity down the conduit and out of the block. Once the source is drained, the anomaly goes away. The source of the water from November 1997 through March 1998 is less certain but may be condensate from above the heaters that were turned off on March 10. As the thermal field collapsed, condensate may have been able to drain through the heater plane and again into this conduit, reestablishing the anomaly late in the test.

There are only two other strong indications of saturation increasing in these planes. The one on August 26, 1997 (perhaps persisting to September 24, 1997) near the north edge of the lower image plane also behaves like a water-wet fracture—spatially compact, developing quickly and then going away. The other anomaly, on February 24, 1998, in the northwest corner of the upper image plane, does not look like the draining of water through a fracture. We do not know the cause of this feature.

The other characteristic of images in both planes are zones of drying that start to appear as early as May 27, 1997, in the lower plane. Clearly, this drying is a result of the high temperatures, but the effects recorded in these images appear different above and below the heater plane. Above the heater, drying appears later and appears to form anomalies with rounded outlines. Below the heater, the anomalies appear as early as May, are more localized, and are linear in shape. The linear shape may be caused by the matrix drying around a planar fracture that cuts through the

image plane. A good example of this is the feature running diagonally from the southwest corner to the northeast corner between May 22, 1997, and March 19, 1998. Even though the anomaly changes character throughout this period, it probably arises from the same structure in the rockmass—a fracture or system of fractures.

Other anomalies of dehydration occur in both planes; some are quite prominent and some are minor. They all support the notion that the dehydration front is steadily advancing from the heater plane into both image planes but that the process is heavily controlled by rockmass heterogenieties.

6.1.2.1.3.2 Vertical Planes

The vertical image planes (see Figure 6-8) intersect the heater plane and even more clearly delineate the effects of heating the block. As expected, the most obvious feature is the drying zone surrounding the heaters. Although drying is not clearly associated with the heaters until May 22, 1997 (about 83 days into heating), once formed, the dry zone is the dominant feature in either image plane all the way through the last data of cool-down (March 19, 1998). Drying was not observed early in the test because the temperatures were not hot enough. It takes a lot of energy to remove the pore water from this rock because of the extremely low hydraulic permeability and high suction potential of the rock matrix. Initial evidence of drying can be observed adjacent to the heaters. On May 22 and June 25, 1997, in the south-to-north plane, zones of drier rock are centered on two heaters. After June 25 these individual zones have coalesced into a single continuous dehydrated zone that grows in size, with some locations eventually losing 85% of the original water content (saturation ratio 0.15). This large dry zone around the heater persists until late cool-down in March 1998, when it appears to be breaking up.

Once formed, the heater dry zone is not a smooth planer anomaly reflecting the heater geometry. Instead it is very irregular in shape with many appendages. There is also a tendency for the dry zone to be relatively flat on top and bottom early in the test but convex on top and concave on the bottom late in the test. We do not have a hypothesis for this behavior. We believe that this rugose image of the heated zone is the result of rock heterogeneities such as fractures. Consider, for example, the part of the block located above the heaters in the western half of the west-to-east plane. By May 22, 1997, there is a vertically oriented dry zone forming between the heater plane and the top of the block. Four months later (September 24, 1997) it is a very linear anomaly that looks a lot like dehydration along a vertical fracture intersecting both the heater plane and the image plane. In Figure 6-9, the interpolated temperature field is superimposed on the July 23, 1997, and the January 23, 1998, saturation images. Notice that this linear-looking zone in the ERT reconstruction corresponds to a high temperature anomaly—additional evidence for drying along a vertical fracture or fractured zone. This figure also demonstrates an approximate correspondence between the dehydration as defined by the ERT data and the 100°C isotherm.

During one month of high block temperatures—August 26, 1997, to September 24, 1997—there is a saturation anomaly adjacent to the dryer feature discussed above. We believe that this combination could be from drying along a nearly vertical fracture zone and wetting of adjacent rock that may be evidence for a heat pipe effect.

Rain fell twice during the test: on June 12, 1997 (Day 104) and on September 2, 1997 (Day 186). The amount and duration of rain that fell in each of these events is unknown so that the more important data, how much rainwater got through the covering and onto the block itself, is also unknown. However, the temperature data offer good evidence that some rainwater reached the block during the June 12, 1997, event because on that date a RTD 5 cm above the heater registered a sharp drop in temperature from about 120°C to 100°C. No such temperature drop was observed below the heaters. This temperature data is consistent with rainwater moving quickly along a fracture from the top to deep within the block.

The RTD that experienced the temperature excursion possibly linked to the rain infiltration is only about 50 cm from the west-east ERT image plane and 25 cm from the south-north ERT plane. In the June 25, 1997, data there is no clear evidence of increased saturation at this location in the west-east plane. In the closer south-north plane, however, the projection of that RTD location onto the plane correlates precisely with the bottom of the strong moisture anomaly in the image (see Figure 6-8). Unfortunately, this identification is not so simple, because this same anomaly appears in the March 22, 1997, image, before the rainfall, and appears to evolve in the July, August, and September images, after the rainfall. It is possible that these ERT anomalies represent a region of fractured rock where both condensate (in May) and meteoric water (in June) collected and that the July, August, and September images show this trapped moisture being driven out the top of the block (September 24, 1997 image).

6.1.2.1.4 Comparison of ERT with Other Data Sets

6.1.2.1.4.1 Comparison of ERT and Fracture Distribution

The ERT images show ample evidence that the block is behaving like a heterogeneous system and that the most obvious source of heterogeneity is fracturing. Of course, the block is heavily fractured, and those fractures were mapped at the five exposed surfaces. Unfortunately, a search for fractures that might be responsible for the ERT anomalies is complicated by two problems. First, fractures are not planar so that the surface expression may be only a guide to the fracture location inside the block. Second, the fracture density is so high that almost any anomaly can be matched with a fracture, making such an association of little value.

Undaunted by these facts, we made an attempt to see a correlation between fractures and anomalies in the ERT images. We chose ERT anomalies that were large in magnitude and persistent over several months and tried to match these with fractures that mapped continuously on two or more faces of the block and that appeared approximately planar. We could not see a consistently convincing correlation between the surface fractures and ERT image anomalies.

6.1.2.1.4.2 Comparison of ERT and Neutron Logs

Neutron logs were made in five vertical holes in the block, and from this data the moisture content was calculated along each borehole at 12 times during heating. In Figure 6-10 we compare the ERT moisture estimates with the neutron log data from the vertical borehole nearest to the west-to-east vertical ERT plane. Of course, the main feature in both data is the development of a large dehydrated zone around the heater that grows from 1 m to 2 m thick in the six months covered by the data. Notice that from both of these measurements a maximum

change in water content near the heaters is calculated to be about 70%. This close agreement is significant because the neutron log and ERT are two completely independent measurements.

There are also differences in the inferences about moisture content from the two methods. For example, the neutron data seems to indicate a slightly thicker dry zone around the heaters. Less subtle, however, are the comparisons outside the heated region. The neutron log does not indicate any significant wetting above the baseline condition anywhere in the block. On the other hand, ERT points to several zones of enhanced wetting. This difference implied by the two results is important because the fate of condensate water is important to understanding the water budget of the block during the test.

We believe that some condensate is stored in the block. However, while the neutron probe is insensitive to it, ERT is probably overly sensitive to its presence. This is because of how the water is distributed in the rockmass. As a matrix block dries, the steam moves into a fracture, then down the pressure gradient along the the fracture until it reaches the dew point, where it condenses. Since the matrix there is already nearly saturated (typically 80%) and also has a very low permeability (typically a few μDarcey), the condensate remains in the fracture aperture. Because the fracture porosity is small compared to the matrix porosity, the neutron probe correctly measures very little increase in moisture content at the location of this condensate. On the other hand, electric current can easily sample fracture networks because, when wet, they act as a network of highly conducting pathways. Therefore, ERT is overly sensitive to this small volume fraction of water and may overestimate the saturation when it is present in a fracture network.

Both methods are sensitive to dehydration of the block. The heat load drives large volumes of vapor from the pores of matrix blocks. This changes the amount of water in volumes comparable to the integration volume of the neutron probe so that this log is sensitive to the change. Matrix water loss also affects electrical current flow that happens along paths through the connected pore water in the matrix.

In Figure 6-10, the neutron log shows slight drying relative to baseline in the top two meters of the block. This may be a response to the vertically oriented drying zone seen in the ERT images only 50 cm from the neutron logging hole.

6.1.2.1.5 Summary and Discussion

We believe that the ERT images, along with the other data we have discussed, support a simple and physically realistic conceptual model for the TH behavior of the system during the LBT.

Dehydration around the heaters is progressive, producing first a small hot zone that grows larger and drier as time progresses. This is the principal process observed and is driven by the imposed heat load. This thermally driven dehydration is the central theme of Figure 6-8. The effect is approximately one dimensional, evolving with time along the vertical axis of the block. However, deviation from a uniformly one-dimensional moisture distribution is significant and appears to be controlled by heterogeneity in the block—probably fractures. For example, the heated zone is not imaged by ERT as a strictly planar anomaly. Even more obvious is the especially strong feature in the west-to-east plane forming as early as May 1997 and persisting to

February 1998. This is a large, strong, and persistent dry zone extending from the heater plane upward to the top of the block.

Water in matrix pores vaporizes as temperature rises. Evaporation must occur even below boiling but becomes especially rapid at the boiling point that is about 96°C.

Water vapor first leaves pores adjacent to fractures because the pressure gradient is steepest there. The drying front then progresses into the matrix block until the whole block is in equilibrium between the suction potential and the vapor pressure. ERT sees many linear features of high resistivity that are likely dehydration along fractures and systems.

Once in the fracture, the water vapor is highly mobile and moves quickly down the pressure gradient. Some of this vapor will exit the block, especially through the top because it is not sealed like the block sides.

That portion of the vapor that remains in the block will move down the pressure gradient, losing heat as it goes, until the dew point is reached, at which point it condenses. This condensate rapidly fills the fracture aperture. Such saturated fractures provide a network of conducting pathways for electrical current in the rock that weren't initially present, and ERT sees this network as an increase in electrical conductivity. Interpretation of this change results as an unnecessarily large moisture increase. This water is detected as a small perturbation by neutron probe because the fracture porosity accounts for a small part of the rock, and the tool is insensitive to it because of the volumetric averaging of the measurement.

The behavior and fate of this condensate that forms in fractures is the key to repository performance, because it is this water, if it can seep back into the emplacement drift, that is most likely to determine the useful lifetime of the canisters—the longer this water can be kept away from the canisters, the longer they will survive.

There are several potential fates for the condensate:

- This water may drain out of the system—through the bottom of the block. This is especially likely below the heaters. Notice the moisture anomaly below the heater near the center of the west-to-east plane in July 1997. It becomes weaker in January 1998, as though it is a fracture draining. However, drainage may also occur for water above the heaters, especially during the early part of the test before the boiling isotherms coalesce from individual heaters. In fact, even a well-developed boiling isotherm may be overwhelmed by large water volumes moving in fractures. This possibility is equivalent to the seepage of water back into the emplacement drift of the repository. Rainwater may have provided such an event on June 12, 1997, and August 2, 1997. Notice that in the July 1997 south-to-north plane there is a linear feature of high saturation—rain water and/or condensate—that is poised above a gap in the dehydration zone forming around the heated plane. The arrangement suggests fracture drainage may be keeping this zone near the heaters from drying.

- This water may participate in a heat pipe. During August and September of 1997, directly above the heaters, there is a persistent wet anomaly adjacent to a persistent dry anomaly in the west-to-east plane. This may be the ERT signature for a heat pipe.

- This water may remain immobile, held by capillarity. There are several persistent wet zones imaged in Figure 6-8 that may exemplify this effect.

- This water may be imbibed into the matrix by the forces of capillary suction. (This seems unlikely to be an important fate of free water because of the short lifetime of this test because of the very small permeability of the matrix and the relatively low suction potential of the initially wet matrix.)

6.1.2.2 Neutron Logging

6.1.2.2.1 Pre-Cut and Post-Cut Moisture Contents

Scoping calculations determined that a minimum initial moisture content of about 50% was required for the block to be suitable for the test of coupled THMC processes. Neutron logging was conducted in four vertical boreholes E2, E3, E4, and E9 (as shown in Figure 2-7 of Wilder, et al. [1997]) before (in December 1993) and after (in March 1994) the sawing, but before the drilling of any horizontal holes. The neutron logging was conducted in bare holes without Teflon lining. The neutron tool was calibrated in a 3.81-cm-diameter hole without the Teflon liner and cement grout for the pre-cut and post-cut measurements. Figure 6-11 shows the water saturation as a function of depth, as determined by neutron logging, in hole E4 in December 1993 (pre-cut) and March 1994 (post-cut). The water saturation determined in other holes agrees well with the values shown here. The background moisture saturation levels were determined to be about 60 to 80%, for a laboratory-determined porosity of about 11% (as shown in Figure 6-11). As shown in Figure 6-11, sawing of the block boundary using water was found to have no significant effect on the moisture content of the block (Lin et al. 1995).

Neutron logging was performed again to estimate the initial moisture content of the block after the installation of the instruments was completed, but before the heating was started. The pre-heat baseline neutron logging was conducted in all holes with the Teflon liner and the cement grout to seal the annular space between the borehole wall and the liner. The result of the pre-heat baseline moisture content will be presented in the following section.

6.1.2.2.2 Pre-Heat Baseline Moisture Content

As mentioned above, the pre-heat baseline moisture content in all neutron holes (both the five vertical and the ten horizontal holes) was measured after the completion of the installation of instruments (pre-heat) in February 1997. The pre-heat baseline moisture content was determined with both the Teflon liner and the cement grout in place. The pre-heat moisture content was determined to establish the baseline so that the effect on its moisture content of heating the block can be determined. The neutron tool was calibrated in a 3.81-cm-diameter hole with the Teflon liner/grout assembly exactly the same as in the neutron holes of the LBT. It was determined that the Teflon liner/grout assembly may have changed the moisture content by no more than 4 to 6%

of the determined value. This is not surprising because the neutron holes in the LBT are designed in such a way that the thickness of the annular cement grout is minimal, only about 0.3 cm.

Figures 6-12 through 6-16 show the pre-heat baseline fraction volume water content in the five vertical holes TN1 to TN5 as a function of depth from the top of the block, respectively. Generally, the initial moisture content in those holes increased with depth and ranged between 0.08 and 0.1. A region at about 0.5 m depth in TN1 to TN3 had a fraction volume water content greater than 0.1, which may be caused by a horizontal fracture intersecting those holes. There is a region at about 4 m depth in TN5 where the initial moisture content was greater than 0.14. The average porosity of the core samples of the large block was determined to be 10.4 ± 1.3%, with a range of 8.2 to 13.6% (Table 3-4). The fraction volume water contents shown in Figures 6-12 through 6-16 correspond to a range of saturation levels between 77 and 96%. The high moisture content at about 4-m depth in TN5 may be caused by a localized greater-porosity rock. As shown in Table 3-5, the porosity determined by mercury porosimetry reached 20% at one location.

Figures 6-17 to 6-22 show the baseline moisture content in holes NN1 to NN6 as a function of depth from the north face of the block. Generally, the initial fraction volume water content in these holes ranged between 0.04 and 0.1. The moisture content increased with respect to depth quickly in the first 0.5 m from the collar, then remained almost constant.

Figures 6-23 to 6-26 show the initial moisture content, in terms of fraction volume water, in holes WN1 to WN4 as a function of depth from the west face of the block. The initial fraction volume water content in these holes ranged from about 0.04 to about 0.11. Similar to the north face horizontal holes, the baseline moisture content first quickly increased with depth, then remained almost constant in the deeper part of the holes.

As mentioned earlier, the purpose of conducting the neutron logging was to study the effect of heat on the moisture content in the block. The neutron counts of the pre-heat logging were subtracted from the in-heat neutron counts, and calibration data were used to convert the difference in the neutron counts into the difference in volume water content. The variation in the water saturation level can be determined by dividing the difference fraction volume water content by the porosity of the rock mass. However, for this report, the difference fraction volume water content, instead of water saturation, during the heating phase of the LBT is presented. The baseline fraction volume water presented so far will help determine the changes in the absolute water content, if necessary.

6.1.2.2.3. Heating Phase and Cooling Phase Moisture Content

The neutron logging results in both the heating phase and the cooling phase will be presented in this report. The neutron logging was conducted in the five vertical holes (TN1 to TN5), six horizontal holes from the north face (NN1 to NN6), and four horizontal holes from the west face (WN12 to WN4). The location of these neutron holes is given in Section 3.2 and in Appendix A of this report. The x-y-z coordinates of the collar of those neutron holes are shown in Table 6-1 to facilitate the discussion of the moisture variation in each hole. The origin of the coordinates is the south-west corner of the top of the block, and x and y directions are east-west and north-south respectively. For reference, the heater plane was at z=-2.743 m. During each of the neutron logs, neutron counts were obtained in each hole at intervals of 10 cm, starting from the bottom of

the hole. The raw neutron counts, the location of measurements in each hole, and the converted difference fraction volume water content are all included in the spreadsheets in the data base at.

LLNL, as well as in the TDMS with DTN LL971204304244.047 (Table 1-1). The difference fraction volume water content in each hole during the test are presented in this section in graphical form, so that the process of the moisture movement can be analyzed. The difference fraction volume water was calculated by subtracting the baseline fraction volume water from that measured during the test. The baseline fraction volume water content in each hole was presented in the previous section. The fraction volume water content can be used to calculate the water saturation by dividing it with the porosity of the rock.

Table 6-1. X-Y-Z Coordinates of the Collar of the Neutron Holes

Hole #	X(m)	Y(m)	Z(m)
TN1	1.219	0.61	0
TN2	1.829	0.61	0
TN3	1.219	1.2119	0
TN4	2.438	1.829	0
TN5	1.219	2.438	0
NN1	2.134	3.048	-0.914
NN2	2.134	3.048	-1.981
NN3	2.134	3.048	-3.81
NN4	0.914	3.048	-0.914
NN5	0.914	3.048	-1.981
NN6	0.914	3.048	-3.81
WN1	0	2.134	-0.762
WN2	0	2.134	-1.676
WN3	0	1.676	-3.962
WN4	0	0.914	-1.676

NOTE: With respect to the southwest corner of the top of the block.

Figures 6-27 to 6-36 show the difference fraction volume water in holes TN1 to TN5 as a function of depth from the top of the block. The neutron results in each hole are divided into two figures so that the figures are not too crowded. The portion of TN2 below about 3.8 m from the top was not available for the logging (Figures 6-29 and 6-30). In these figures, the positive fraction volume water means gaining moisture content; the negative fraction volume water means losing moisture content. Generally speaking, these figures show that a well-defined dryout zone developed since the 48 days of heating at the heater plane, which was at about 2.74 m from the top of the block. One exception was TN4, in which the dryout zone did not develop until sometime between the 48th day and the 60th day of heating. The dryout zone widened with time, and the extent of the drying also increased with time, due to the continuous heating. The widths of the maximum dryout zones, as measured at the half of the extent of the dryness, were 1.66, 1.5, 1.69, 1.49, and 1.59 m for TN1 to TN5 respectively. It is fair to say that the width of the dryout zone is quite uniform. There was not much change in the extent of the dryness since Day 361 of heating. In TN4, however, there was a decrease of the dryness by about 0.05 after Day 361, and it remained unchanged subsequently. There were some variations in the shape of the tip

of the dryout zone as shown in these figures. The dryness in those five vertical holes ranged from –0.07 to –0.09 fraction volume. Those variations among the five vertical holes illustrate the effect of heterogeneity in the block on the movement of moisture. Those figures do not show significant rewetting during the cool-down phase, i.e., after Day 376. The measured change in the moisture content agreed well with what had been predicted in the scoping TH calculations, as shown in Figure 3-3 of the Large Block Test Status Report (Wilder et al. 1997).

Figures 6-37 to 6-48 show the difference fraction volume water content in the six horizontal holes drilled from the north face of the block. Again, the neutron results in each hole are divided into two figures so that each figure is not too crowded. Generally, the variation of the moisture content was uniform across the block. The neutron results in those holes show decrease in moisture content with time, as expected. The variation of the moisture content in those holes depends on the vertical location of the hole. Holes NN1, NN3, and NN4 showed little change in the moisture content, about –0.02 in the entire test period. The moisture content in holes NN2 and NN5 showed the extent of dryness comparable to that near the heater plane in the vertical holes, to about –0.07 fraction volume. This is expected because, as shown in Table 6-1, NN2 and NN5 were the closest, among those six holes, to the heater plane, only about 0.76 m above the heater plane. The neutron results in NN6 showed some abnormal responses relative to the other holes. The measurements on July 8, 1997, November 6, 1997, and January 29, 1998, showed significant increase in the moisture content. This was probably related to the TH events shown by the temperature fluctuations, as discussed in Section 5.4.3. This seemed to be isolated to this hole; therefore, the moisture was probably related to a fracture zone in the block. Careful examination of Figures 6-40, 6-42, and 6-44 indicated that there were some indications of moisture refluxing. For example, the moisture content measured on July 8, 1997, was greater than that measured on the previous days in some locations in those holes. However, the amplitude of the variation was very small. Again, as mentioned above, there was no indication of re-wetting based on the moisture measured in those horizontal holes.

Figures 6-49 to 6-56 show the moisture content measured in the four horizontal holes drilled from the west face of the block, WN1 to WN4. Similar to the horizontal holes from the north face, the variation in the moisture content in these four holes from the west face showed uniform decrease of the moisture with time across the block. The extent of the moisture decrease depended on the vertical location of the hole. Generally, the vertical distance of these holes from the heater plane was greater than that of those holes from the north face. Therefore, it is expected that the variation in the moisture in the WN holes would be less than that in the NN holes. Figures 6-55 and 6-56 show an abnormal case. In this hole, WN4, there was a zone at about 1.3 m from the collar where significant gainings of moisture were measured on Days 74, 88, and 103 (May 13, 1997; May 27, 1997; and June 11, 1997). The moisture seemed to have refluxed during this period. This period was before the TH event as registered by the temperature measurement. The moisture might have been the condensed water channeled to the neutron hole by a fracture system. Drying began to develop on July 8, 1997 (Day 130) in a zone at about 0.8 m from the collar of this hole. This dryout zone continued to develop throughout the remainder of the test. This hole was in parallel with the heaters and was about 1.07 m above the heater plane. The distinguished dryout zone was probably caused by a fracture zone that intersected with the hole, which may have provided a flow path to facilitate the dryout. Those neutron results show no significant rewetting in the cool-down phase.

In summary, the moisture content measured by neutron logging showed that the moisture movement in the block was almost one-dimensional. A well-defined dryout zone was developed at the heater plane. The neutron results did not show significant rewetting during the cool-down phase. Fractures have important roles in the localized movement of the moisture, and a discrete fracture model may be needed to analyze the process.

6.2 THERMAL-HYDROLOGICAL ANALYSIS

6.2.1 In-Test Thermal-Hydrological Model

Three-dimensional TH analysis of the LBT during the early stage of the test was reported in Section 3.1.3 of the LBT Status Report (Wilder et al. 1997). The calculations modeled the as-built block geometry. In the calculations, the block was heated at 450 W per heater for six months (182.5 days), after which the heaters were turned off, and the cool-down was simulated for an additional six months. Equivalent Continuum Model (ECM) was used in the model calculations, and the power outages were included. Seven model calculations were conducted for the in-test TH analysis. The first case was designated as Case A; the rest were called Case 1 to Case 6. Case A modeling used rock properties from the Reference Information Base (RIB) (DOE 1995), except that the bulk air-permeability was adjusted to approximate the median value obtained by the pre-heat single-hole air-injection (Figure 6-1). The Case A rock properties are shown in Table 6-2 as the TSw2 unit. The bulk permeability value of 9.87×10^{-14} m^2 is the value in the RIB; the value of 3.3×10^{-15} m^2 was the median value of the measured permeability (Figure 6-1). The initial moisture saturation for Case A was assumed to be 92%. Case A did not include the power outage information.

Figure 6-57 shows one example of the calculated temperature and liquid saturation distributions on the block in Case A modeling. Figure 6-57 agrees well with the preheat predictions, as shown in Figure 3-26. As indicated in Section 5.3.2 and Section 6.1.2.2.3, the predictions agree well with the measured data.

Case 1 through Case 6 used the rock properties listed in Table 6-2, with various initial water saturation values. These modelings were to investigate the effects of rock property and the initial water saturation on the predicted temperature. Cases 1–3 used the TSw2 properties in Table 6-2 with initial water saturation of 92%, 70%, and 65% respectively. Cases 1 and 2 used the greater bulk permeability in Table 6-2 for TSw2; Case 3 used the smaller bulk permeability value for TSw2 in Table 6-2. Cases 4–6 used the tsw34 rock properties in Table 6-2 with initial water saturation of 92%, 70%, and 80% respectively. For a node at the heater level, adjacent to the heater midpoint and 35 cm from the center heater, the temperature history of those models show substantially higher temperatures for TSw2, compared with tsw34 (Figure 3-7 of Wilder et al. 1997). This difference may be partially explained by the lower permeability of TSw2, relative to that of tsw34, as shown in Table 6-2. The temperature for a smaller bulk permeability was greater than that for a model with greater bulk permeability; it was also true for the initial water saturation level. Cases 2 and 3 showed no sign of boiling due to the smaller level of initial water saturation. Case 1 showed some signature of rapid evaporation but not as rapid as boiling. Case 5 showed signatures of boiling. Case 6 showed prolonged boiling. The temperature in Case 4 stayed at boiling for the entire heating period of modeling, 180 days. The differences among Cases 4–6 were due to different initial water saturation.

Table 6-2. Hydraulic and Thermal Properties of Rock Units

Properties	TSw2	tsw34
Bulk permeability (m^2)	9.87×10^{-14} 3.30×10^{-15}	1.59×10^{-12}
Matrix permeability (m^2)	4.00×10^{-18}	1.01×10^{-15}
Fracture permeability (m^2)	8.33×10^{-10}	6.55×10^{-9}
Matrix van Genuchten a (1/Pa)	6.40×10^{-7}	7.72×10^{-7}
Fracture van Genuchten a (1/Pa)	1.34×10^{-3}	6.86×10^{-4}
Matrix porosity	0.11	0.11
Fracture porosity	1.19×10^{-4} 3.96×10^{-6}	2.34×10^{-4}
Matrix van Genuchten b (1/Pa)	1.47	1.47
Fracture van Genuchten b (1/Pa)	3.00	1.48
Wet thermal conductivity (W/m·C)	2.10	2.33
Dry thermal conductivity (W/m·C)	2.10	1.56
Specific heat (J/kg·C)	928	948

6.2.2 Post-Test Analysis

6.2.2.1 Purpose

The Thermal Test TH AMR (Section 6.2.4 of CRWMS M&O 2000c) reported post-test modeling of the TH processes in the LBT with NUFT 3.0.1s (STN 10130-3.0.1s-00) code using the implicit dual-permeability model with the active fracture concept. Two TH property sets were used in the model analyses. Those are the drift-scale (DS) and the mountain-scale (MS) property sets, as shown in Table 5-1 (extracted from Table 7 of CRWMS M&O 2000c), which includes the thermal properties of the insulation materials on the block sides. This section compares the results of TH calculations with the liquid-phase saturations measured in the block. Simulation results using the DS rock property set are first compared with field data to evaluate how well they match. Simulation results using the DS property set are then compared to results generated using the MS property set, and the two sets of results compared to field data. It is understood that the LBT was not designed to evaluate various TH property sets used in the YMP. However, it is interesting to see how well those property sets work.

6.2.2.2 Numerical Model

The model geometry, boundary and initial conditions, and heater power history are identical to those presented in Section 6.1.4 of the Thermal Test TH AMR for the DS property set. The DTN for heater power histories used in the analysis is LL980918904244.074.

6.2.2.3 Rock Property Data Sets

Hydraulic and thermal properties of the tsw34 unit of the DS base case property set (DTNLB990861233129.001) and the MS base case property set (DTN LB997141233129.001) were used in model calculations (Table 5-1). The tsw34 unit was used because the hydrogeologic

unit of the LBT area is equivalent to the tsw34 model unit (Tptpmn) of the site-scale unsaturated zone (UZ) flow model. The only difference between the DS and MS properties for the tsw34 unit is a higher fracture permeability of 1.70×10^{-11} m^2 for the MS versus 2.76×10^{-13} m^2 for the DS.

6.2.2.4 Drift-scale Simulation Results Versus Field Data

Figure 6-58 shows the liquid-phase saturation profile along TN3, a vertical borehole used for neutron probe measurements of water content. Model results are compared to liquid-phase saturations measured by neutron probe (DTN LL971204304244.047, LL980919304244.075). The field measurement times, 103, 361, and 501 days are compared at model times of 100, 365, and 500 days. The small differences between model and field times should have a negligible effect on the comparisons since saturation changes develop relatively slowly. The simulated dryout zone develops slowly and remains smaller than the field zone at all three times. At about 100 days, the model dryout zone is poorly developed, with no point on the profile having a liquid saturation less than 0.375, half the initial saturation. Note that a locale where the liquid saturation is less than half the initial value is defined to be included in the dryout zone. In contrast, the field dryout zone is well developed at 100 days, showing a thickness of about 0.75 m and a minimum liquid saturation of about 0.12. The field data also show a distinct recondensation zone approaching full saturation about 1.3 m below the heater horizon, and a small recondensation zone about 0.5 m below the upper surface of the block. The field data show sharp fluctuations in saturation not observed in the model results. This difference is probably due to heterogeneities in the TH properties of the fractured rock not incorporated into the property set. At about 365 days (10 days before power shutdown) the model dryout zone is fully developed, with a thickness of 1.4 m, but continues to lag the field zone that now has a thickness of 1.9 m. The recondensation zones above and below the heater horizon are still evident at 365 days, and the geometry is very similar to that observed at 100 days. At 500 days (125 days after power shutdown), the model dryout zone thickness is 1.25 m, a reduction of only 11% from the 365-day thickness, and the field dryout zone thickness is 1.6 m, a reduction of 16% from the 365-day value. The field recondensation zones above and below the heater horizon persist at 500 days, while the model shows no significant recondensation.

6.2.2.6 Drift-scale Versus Mountain-scale Simulation Results

A comparison of the liquid saturation profiles for the two property sets, shown in Figure 6-59, will shed some light on the differences observed between the two temperature profiles, as shown in Figure 5-35. In Figure 6-59 liquid saturation profiles for the DS and the MS models are shown at 100, 200, and 300 days. The dominant feature of the profiles at all three times is a substantially larger dryout zone for the MS set. Note that the MS property set has a fracture permeability that is nearly two orders of magnitude greater than the fracture permeability for the DS property set. The higher permeability permits more rapid vapor flow from the hot zones to the cold zones, causing faster drying in the hot zones. The drier hot zones, with a lower thermal conductivity, then transfer heat by conduction at a slower rate and therefore experience a greater temperature rise. The higher fracture permeability therefore explains the reason why simulations with the MS property set consistently predict higher temperatures in and adjacent to the heater horizon, as shown in Figure 5-35.

6.2.3 Summary

Water saturation, calculated in TH models using both DS and MS property sets, is compared with the LBT data measured by neutron logging. This comparative analysis is to assess the performance of the TH model in general, and the performance of the DS and MS property sets in particular. The results of the comparison are summarized as follows:

The movement of water in the LBT as predicted by the TH model is qualitatively consistent with the measured field data. In other words, both model predictions and field data show drying at the heater horizon. Quantitatively, the model-predicted dryout zone developed slower than the dryout zone in the field test, and the predicted dryout zone is smaller than the field data. The size of a dryout zone and the timing of developing a dryout zone are probably affected by rock properties, including heterogeneity. The dryout zone modeled using the DS property is significantly smaller than that modeled using the MS property. This is probably due to the greater fracture permeability in the MS property set. As mentioned earlier in this section, the LBT was not designed to test a rock property set, due to its size and the near-surface setting. Therefore, the effect of the property set on the predicted moisture movement as inferred from this comparison should be considered as for reference only.

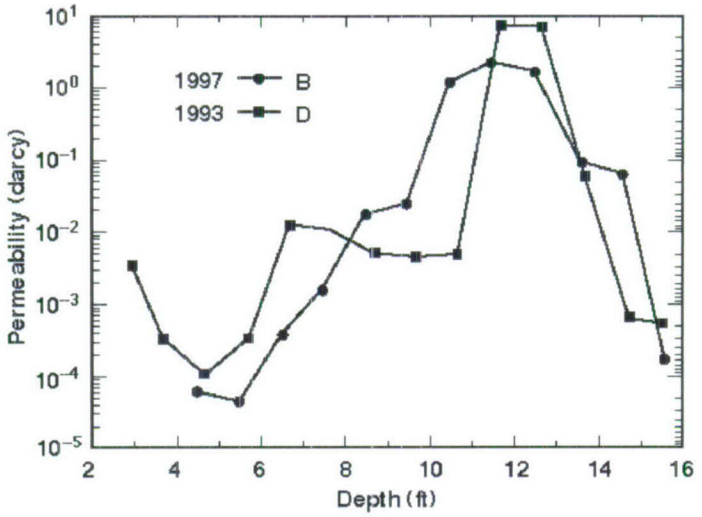

Figure 6-1. Air Permeability Measured in a Single Hole Before Cutting (D) and After Cutting (B) the Block as a Function of Depth.

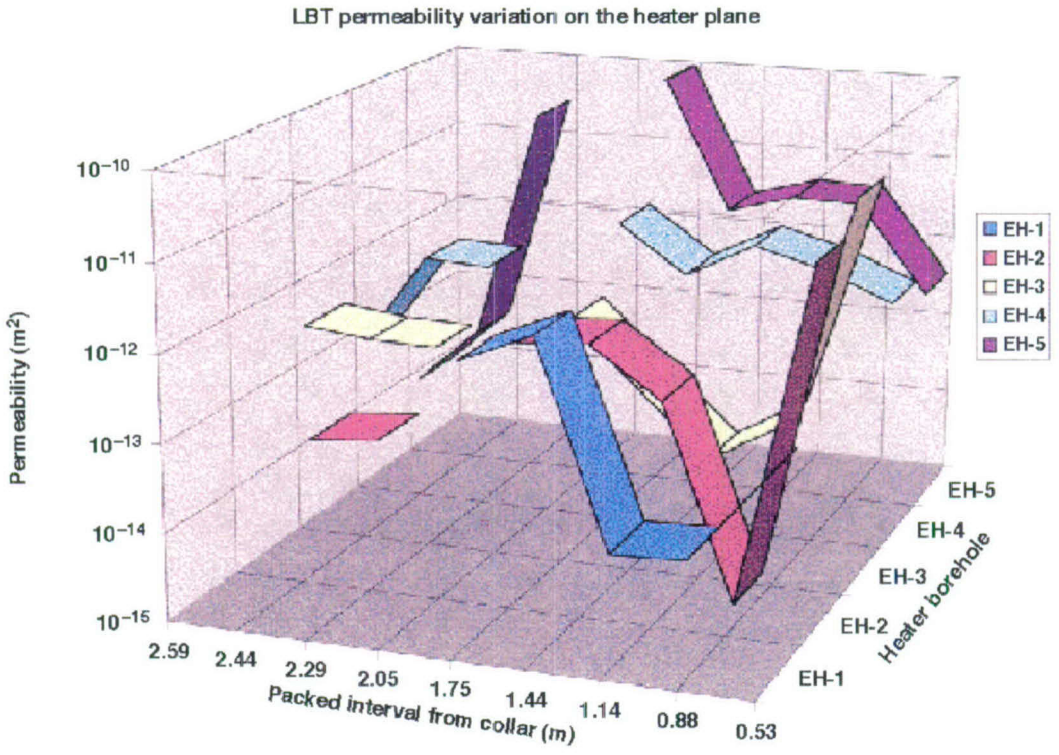

Figure 6-2. Air Permeability Variations Along Five Heater Boreholes at the LBT Site

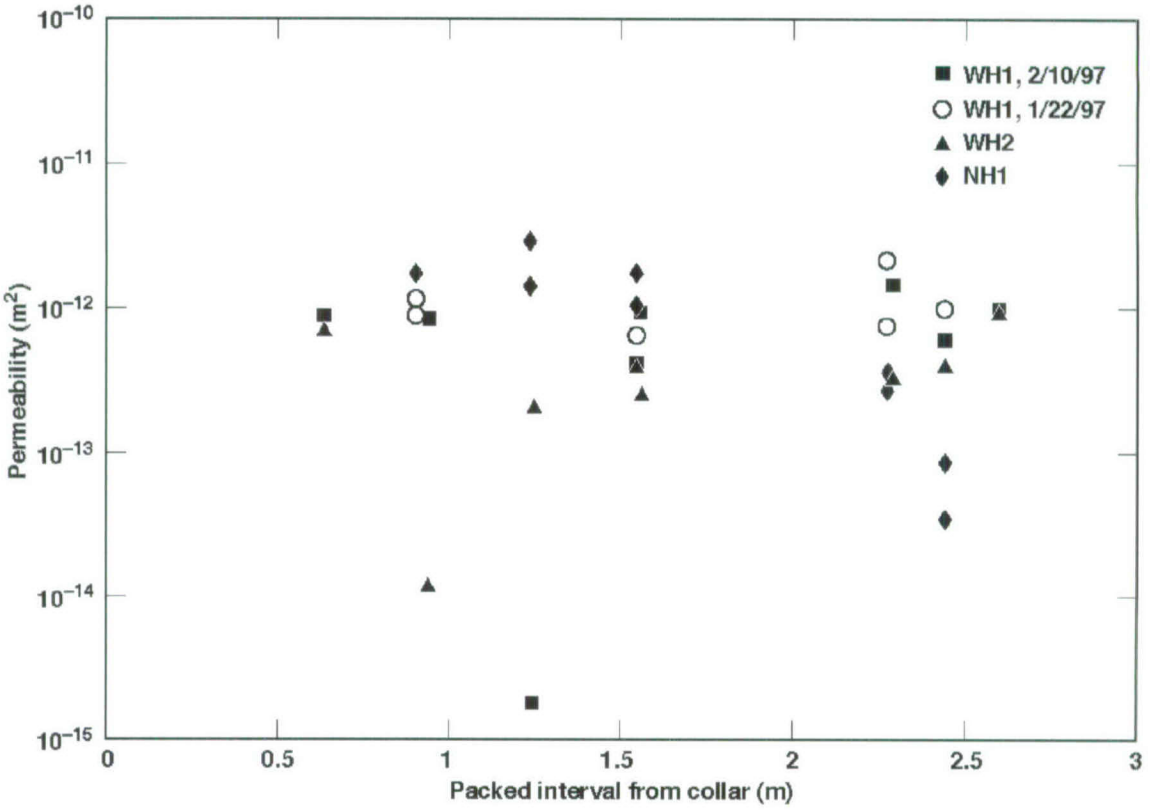

Figure 6-3. Air Permeability Variations Along Three Horizontal, Hydrologic, Monitoring Boreholes at the LBT Site

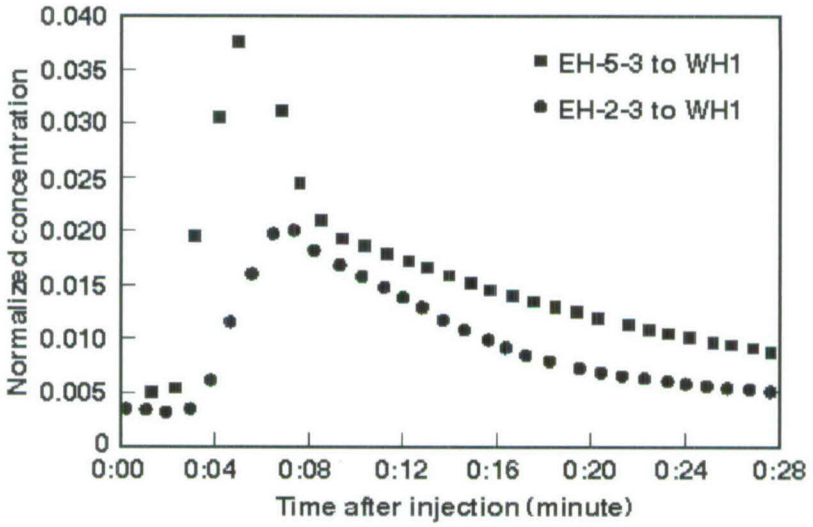

Figure 6-4. Tracer Breakthrough Curves from Heater Borehole Intervals to a Hydrologic, Monitoring Borehole WH1 at the LBT Site

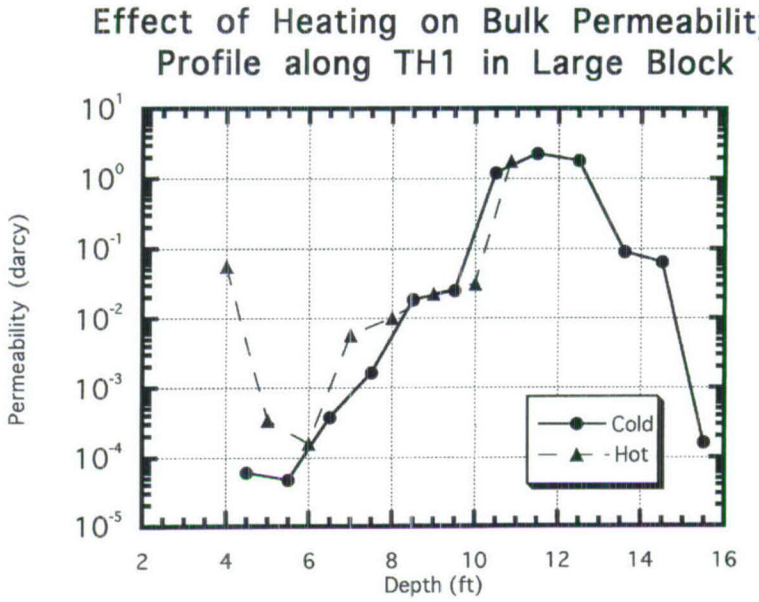

NOTE: The "cold" curve is the same as the "B" curve in Figure 6-1.

Figure 6-5. Air Permeability Measured by Single-hole Injection Along Hole TH1 in the Block Before Heating (Cold) and During Heating (Hot)

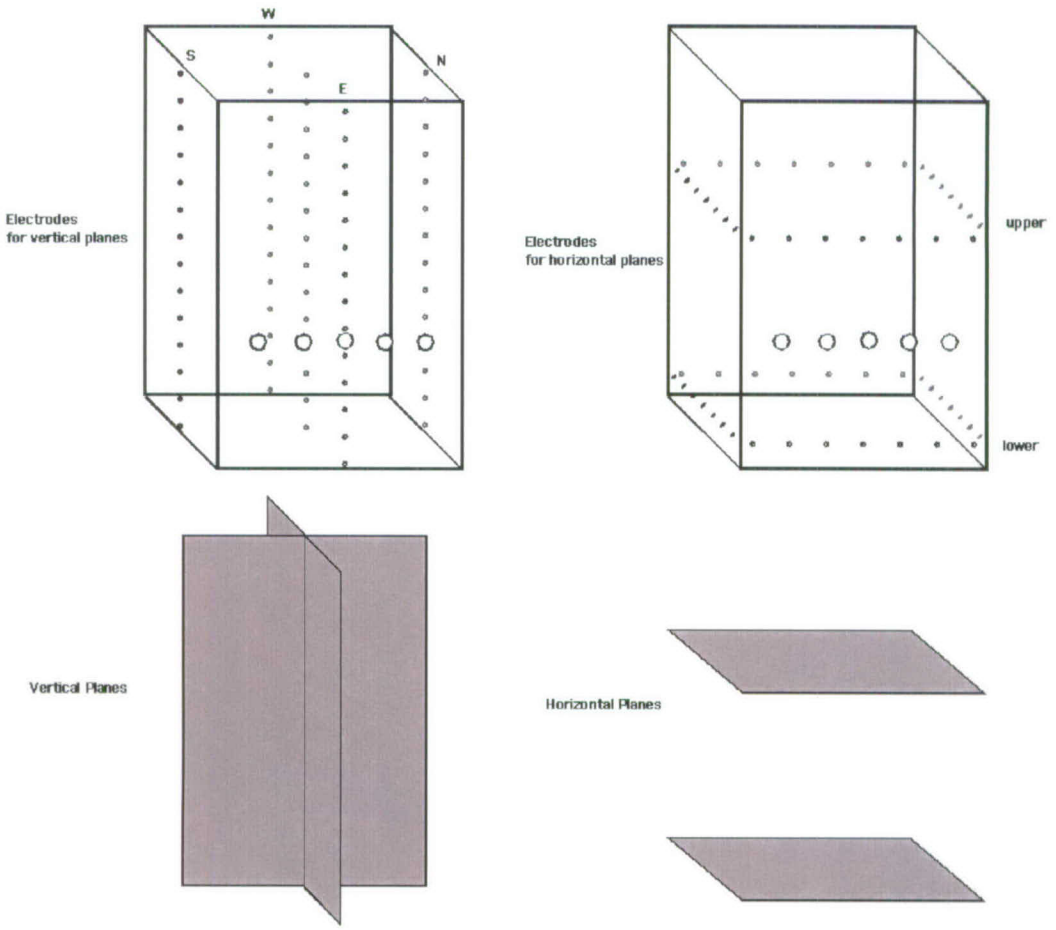

NOTE: All electrodes are on the surface of the block except the array in the center where the two vertical planes intersect. The heater hole locations are shown for reference.

Figure 6-6. Layout of ERT Electrodes for the Large Block Test

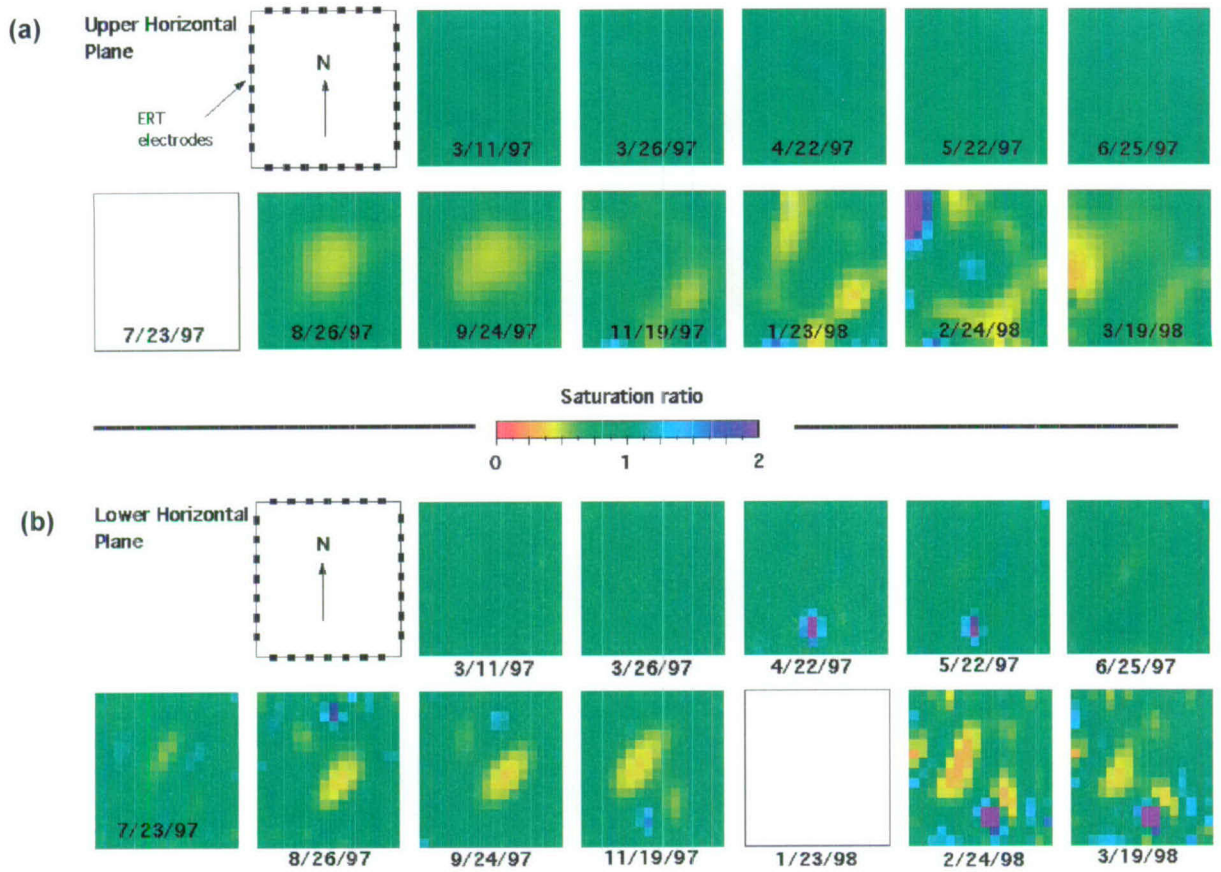

NOTE: Blank spaces indicate data sets that did not converge. The saturation ratio is (moisture content)/(initial moisture content). (a) The upper plane, (b) The lower plane.

Figure 6-7. Changes in the Distribution of Moisture Content in Two Horizontal Image Planes

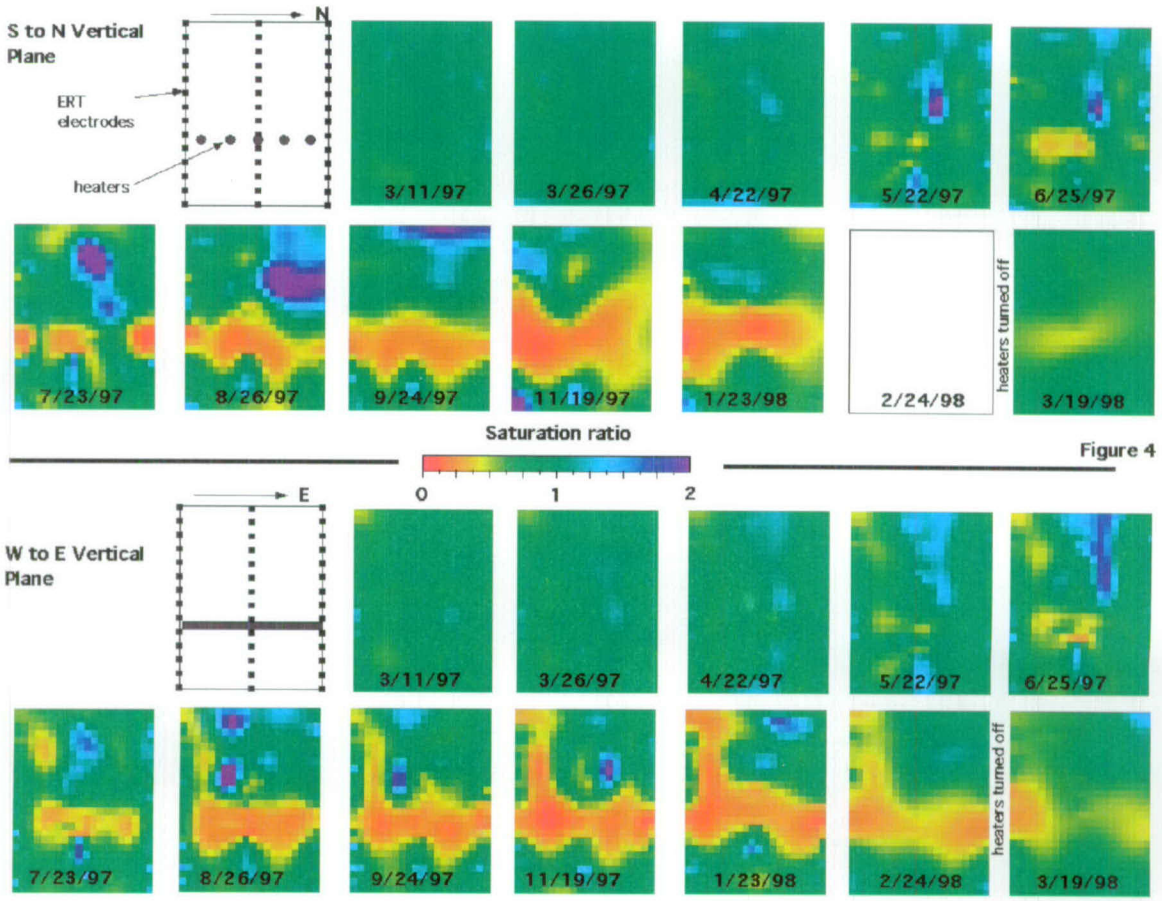

NOTE: Blank spaces indicate data sets that did not converge. The saturation ratio is (moisture content)/(initial moisture content). (a) The upper plane. (b) The lower plane.

Figure 6-8. Changes in the Distribution of Moisture Content in Two Vertical Image Planes

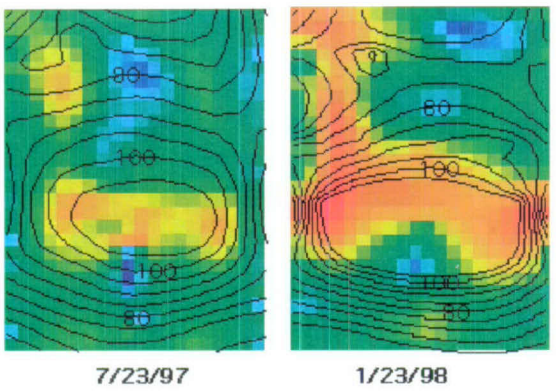

NOTE: The change in water content was calculated assuming a porosity of 0.12 and an initial saturation of 0.75.

Figure 6-9. Interpolated Temperature Isotherms (°C) Superimposed on ERT-Derived Images of Volumetric Water Change in the West-to-East Plane

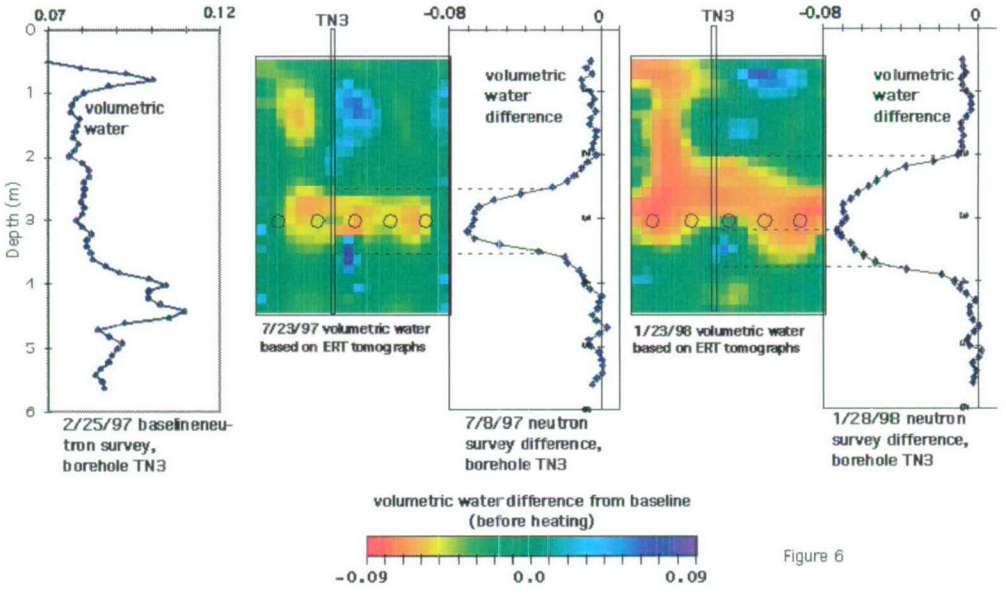

Figure 6-10. Comparison of Neutron Log and ERT Measurements of Changes in Moisture Content

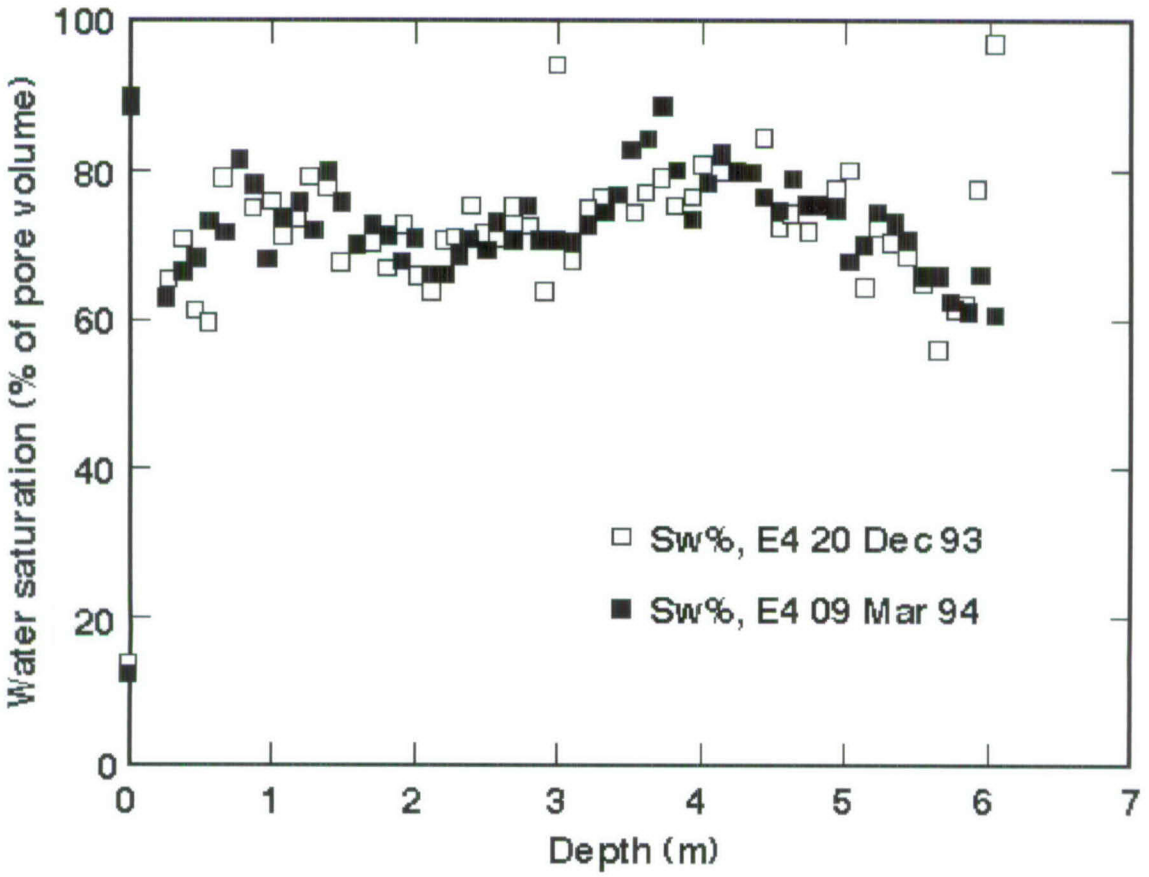

Figure 6-11. Pre-Cut and Post-Cut Water Saturation as a Function of Depth

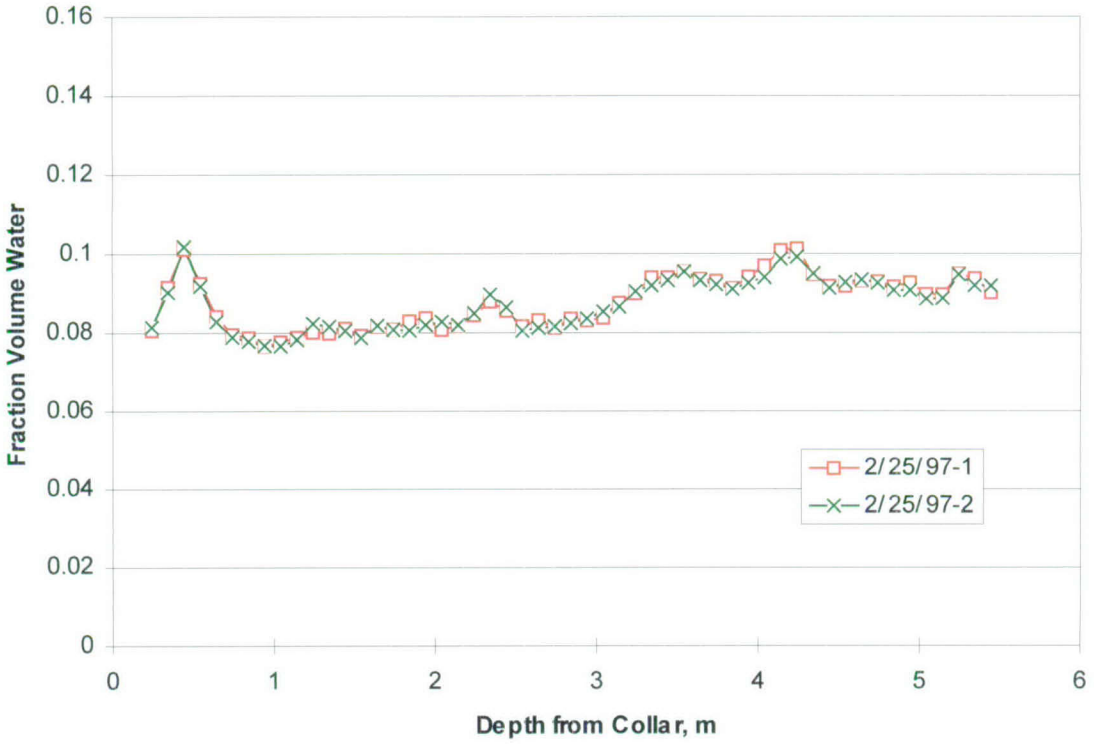

NOTE: As a function of depth from top of the block.

Figure 6-12. The Baseline Moisture Content Measured in Hole TN1

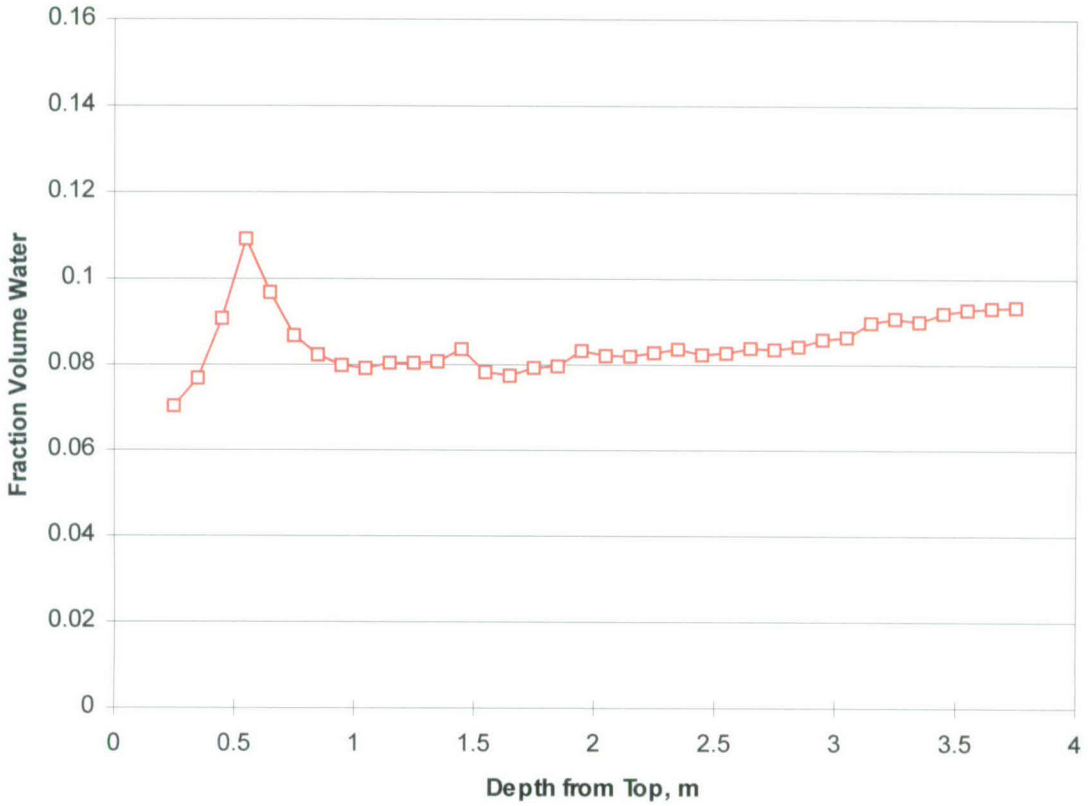

NOTE: As a function of depth from top of the block.

Figure 6-13. The Baseline Moisture Measured in Hole TN2

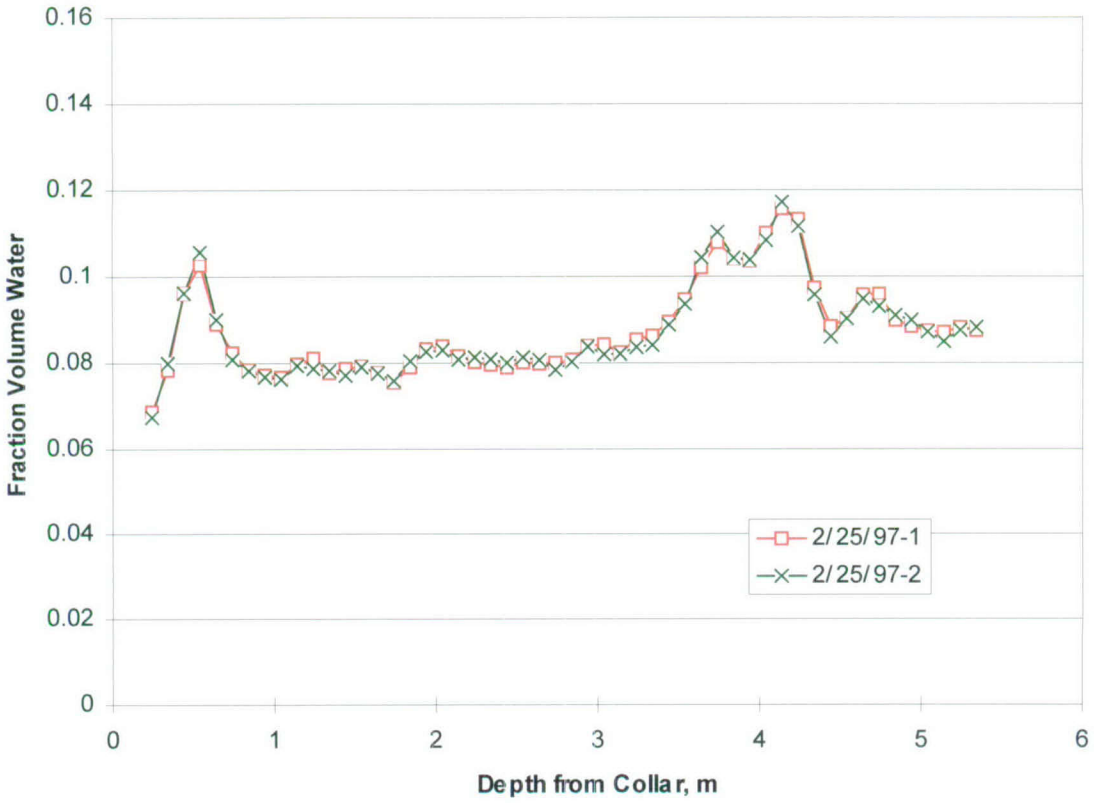

NOTE: As a function of depth from top of the block.

Figure 6-14. The Baseline Moisture Content Measured in Hole TN3

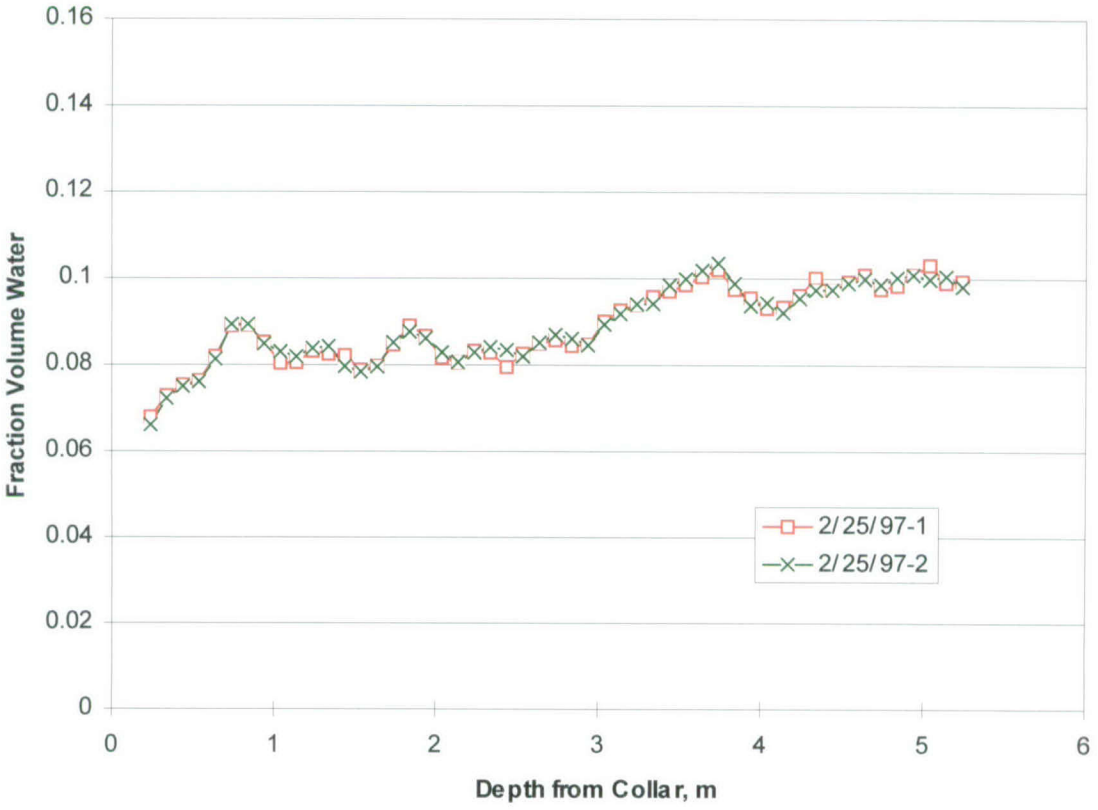

NOTE: As a function of depth from top of the block.

Figure 6-15. The Baseline Moisture Content Measured in Hole TN4

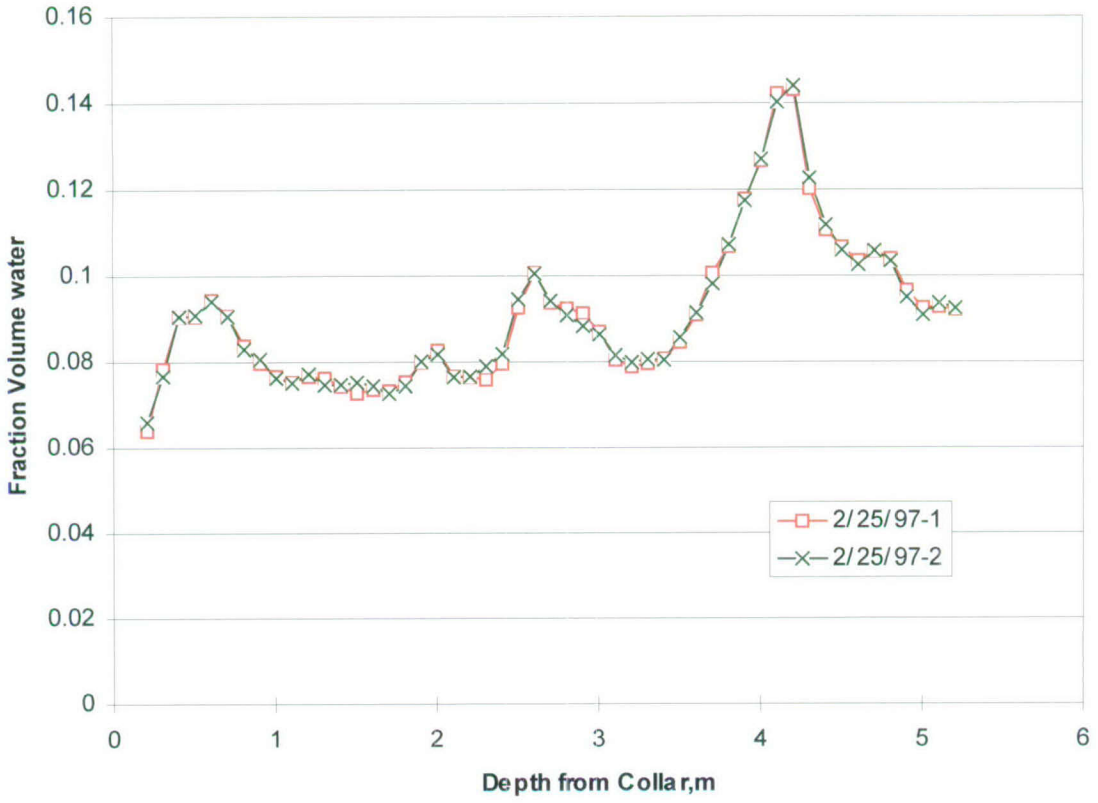

NOTE: As a function of depth from north face of the block.

Figure 6-16. The Baseline Moisture Content Measured in Hole TN1

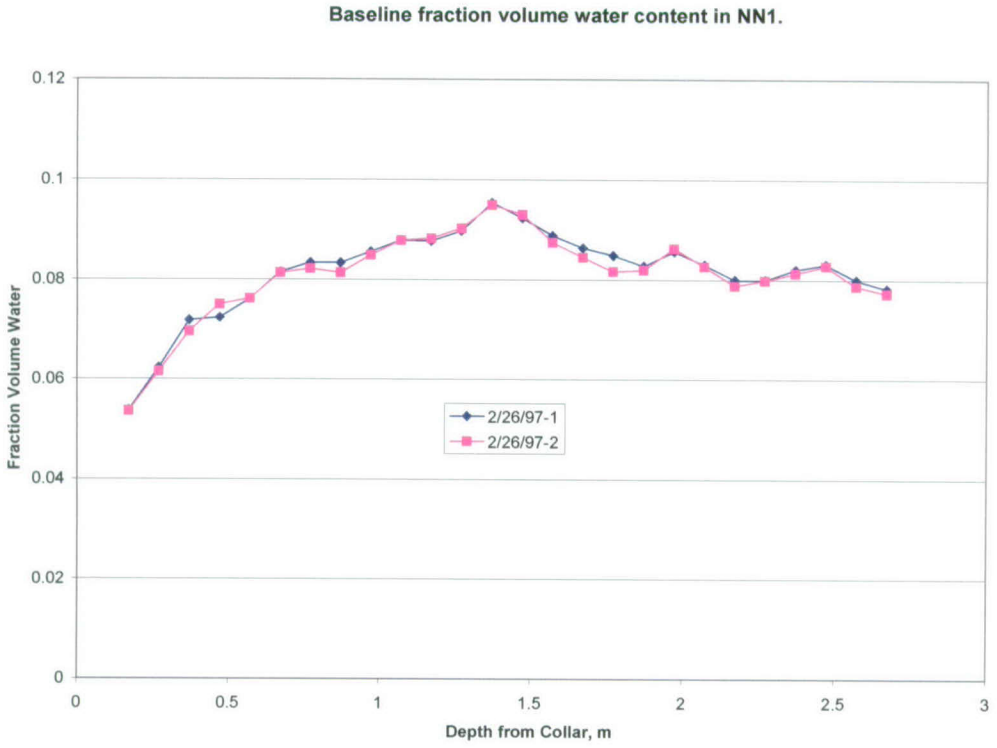

NOTE: As a function of depth from north face of the block.

Figure 6-17. The Baseline Moisture Content Measured in Hole NN1

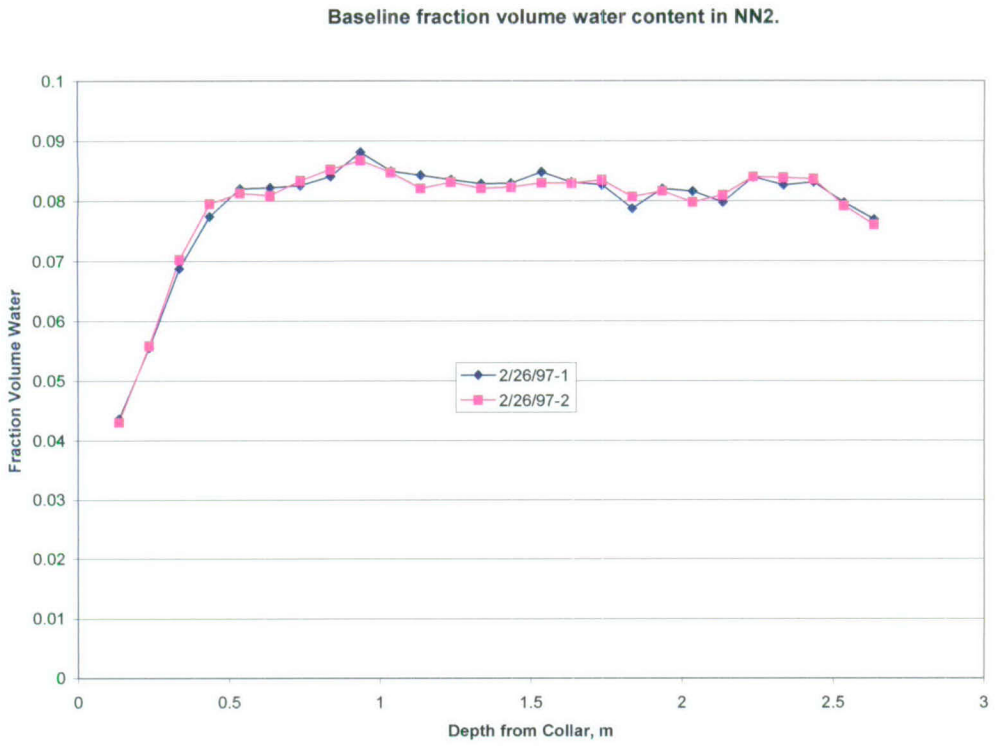

NOTE: As a function of depth from north face of the block.

Figure 6-18. The Baseline Moisture Content Measured in Hole NN2

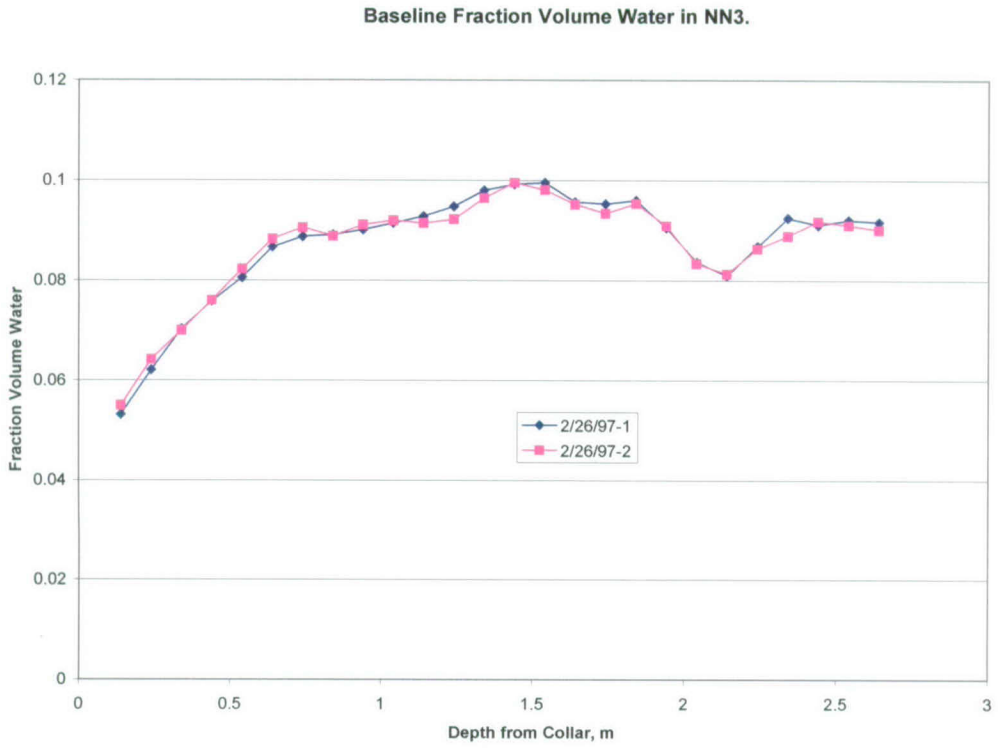

NOTE: As a function of depth from north face of the block.

Figure 6-19. The Baseline Moisture Content Measured in Hole NN3

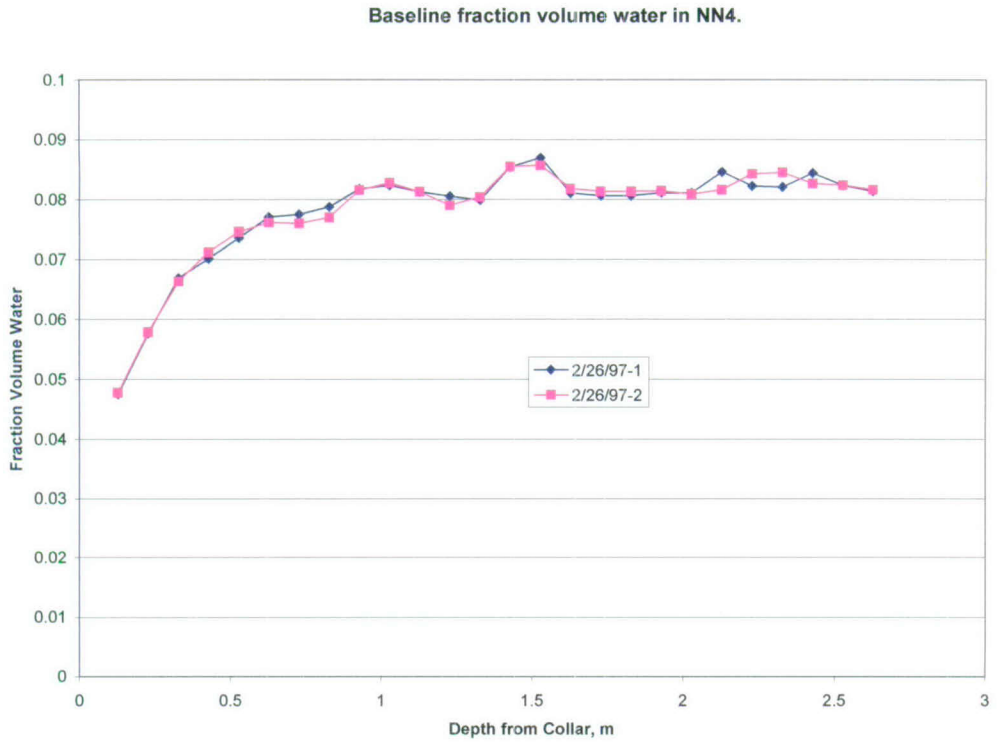

NOTE: As a function of depth from north face of the block.

Figure 6-20. The Baseline Moisture Content Measured in Hole NN4

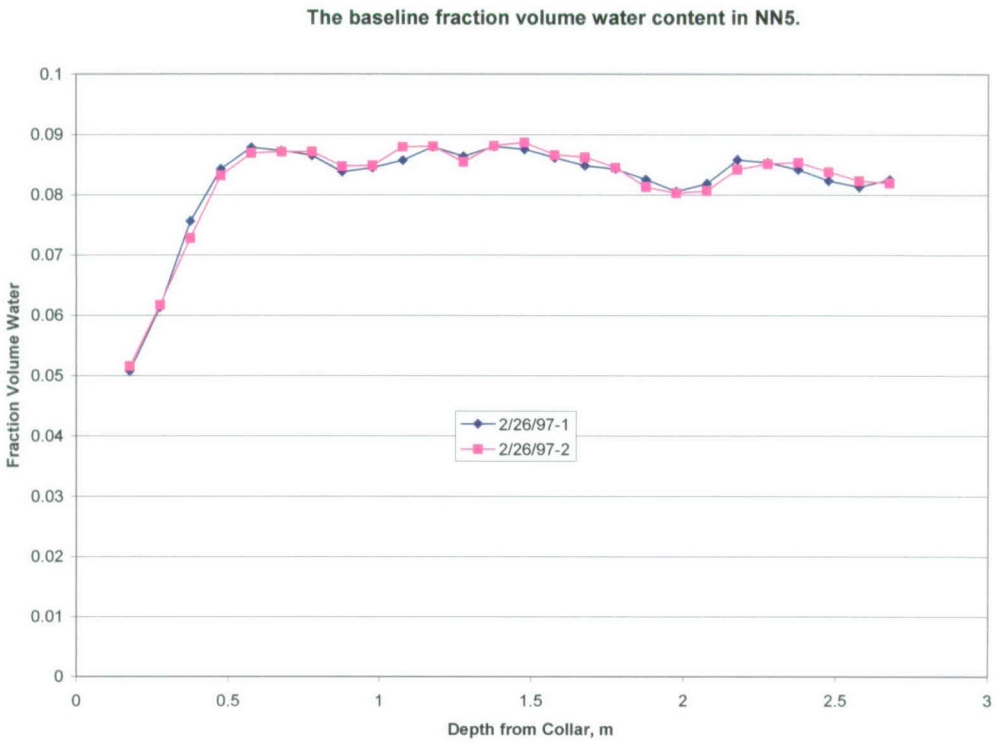

NOTE: As a function of depth from north face of the block.

Figure 6-21. The Baseline Moisture Content Measured in Hole NN5

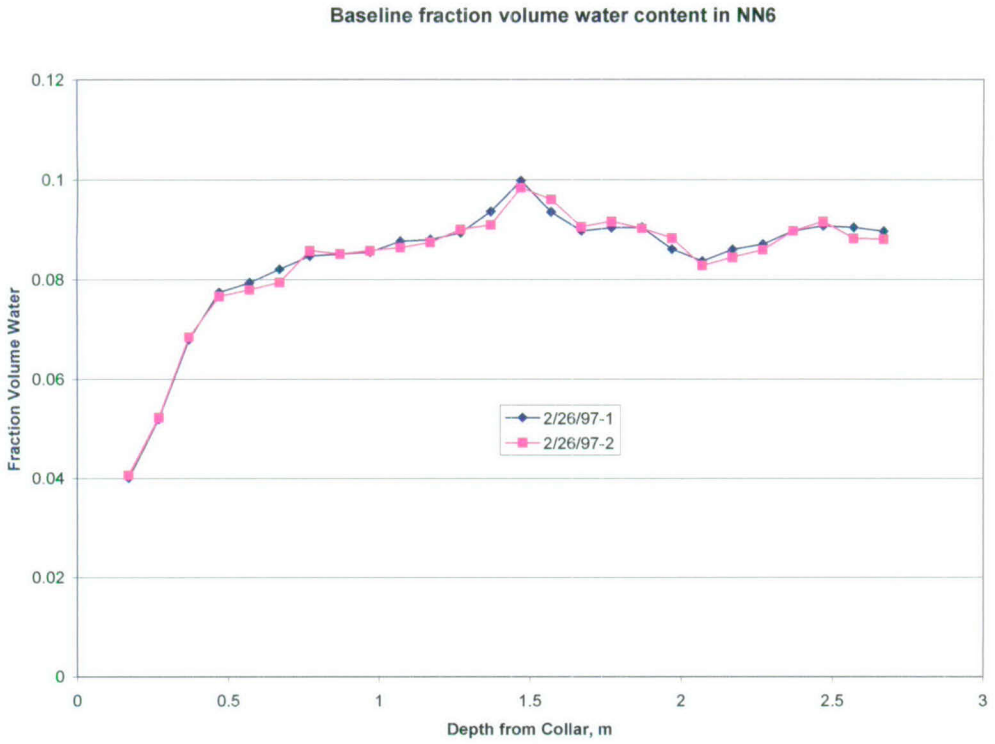

NOTE: As a function of depth from north face of the block.

Figure 6-22. The Baseline Moisture Content Measured in Hole NN6

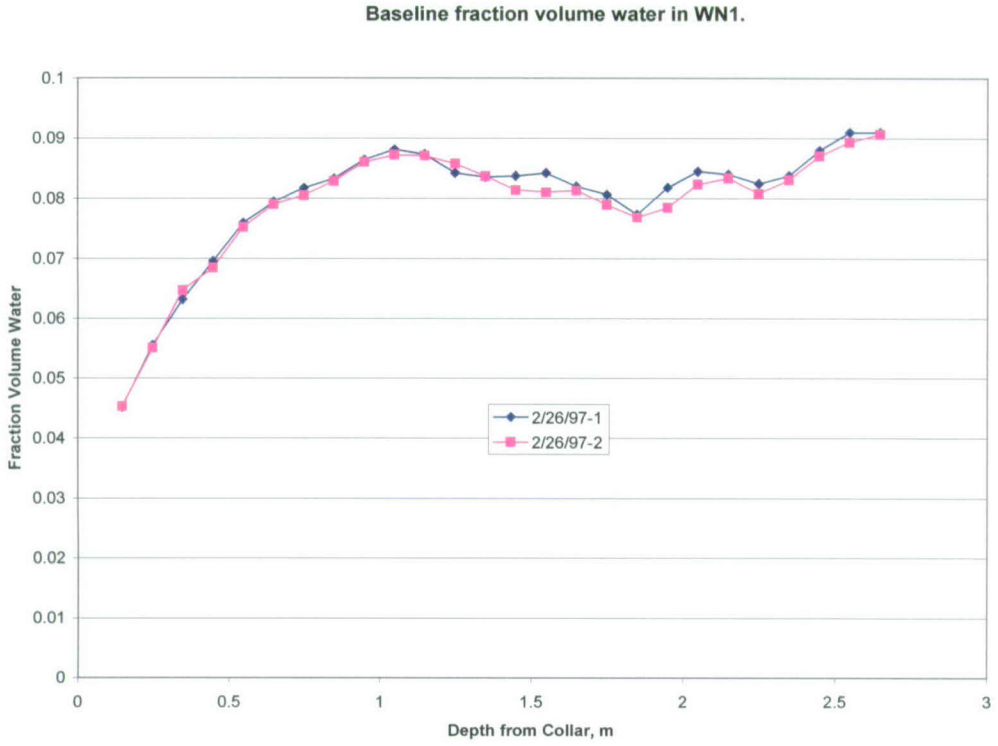

NOTE: As a function of depth from west face of the block.

Figure 6-23. The Baseline Moisture Content Measured in Hole WN1

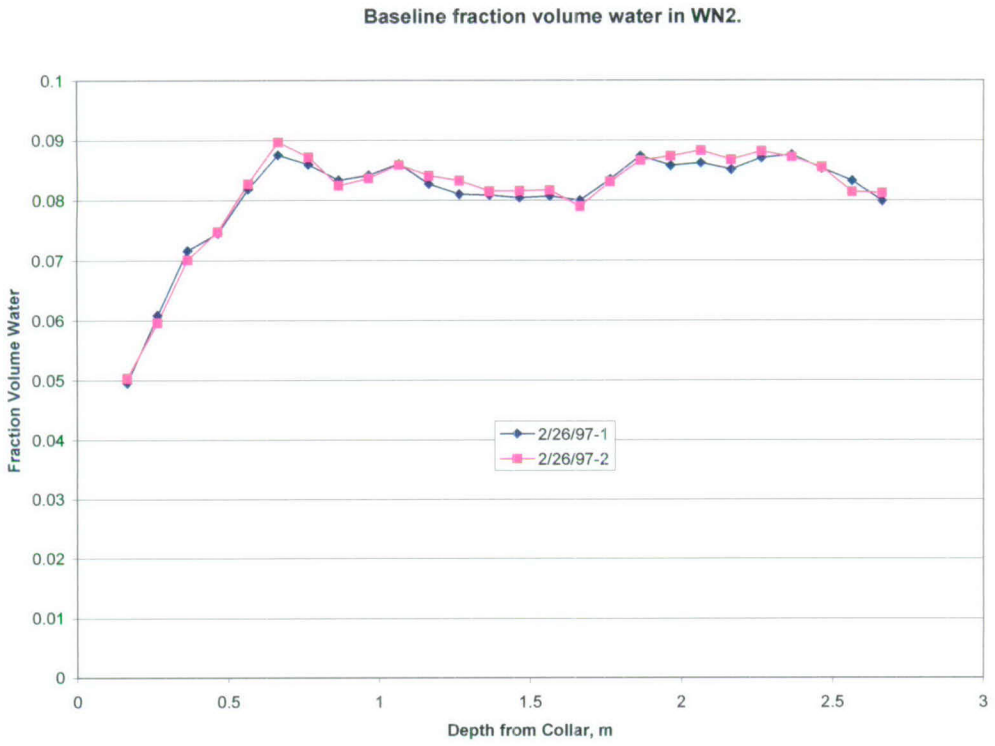

NOTE: As a function of depth from west face of the block.

Figure 6-24. The Baseline Moisture Content Measured in Hole WN2

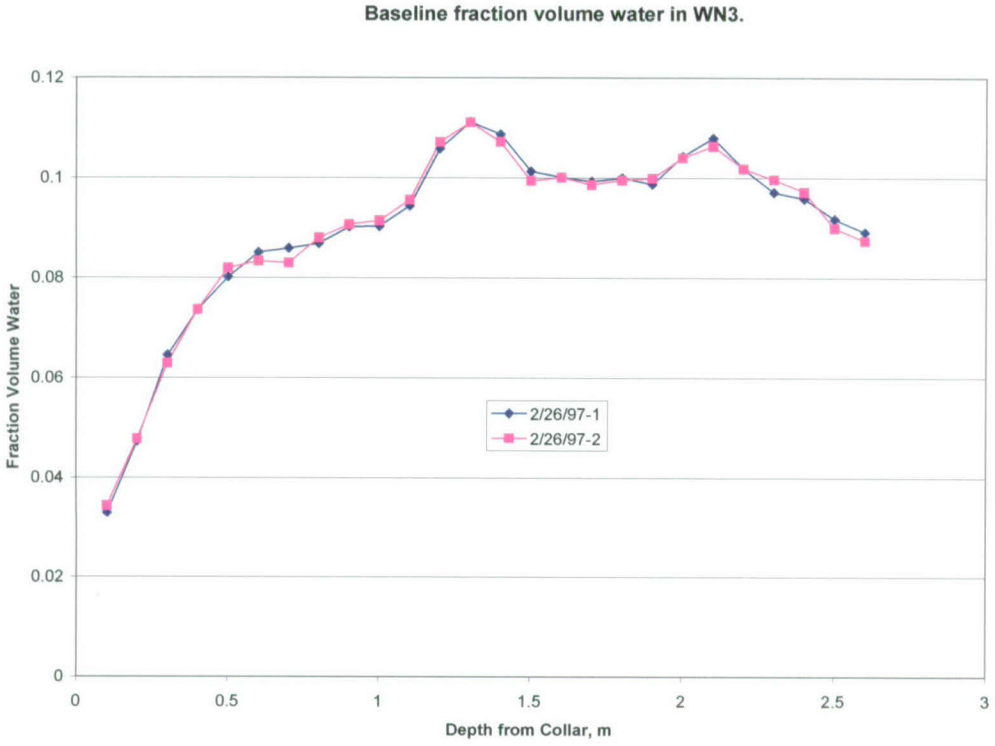

NOTE: As a function of depth from west face of the block.

Figure 6-25. The Baseline Moisture Content Measured in Hole WN3

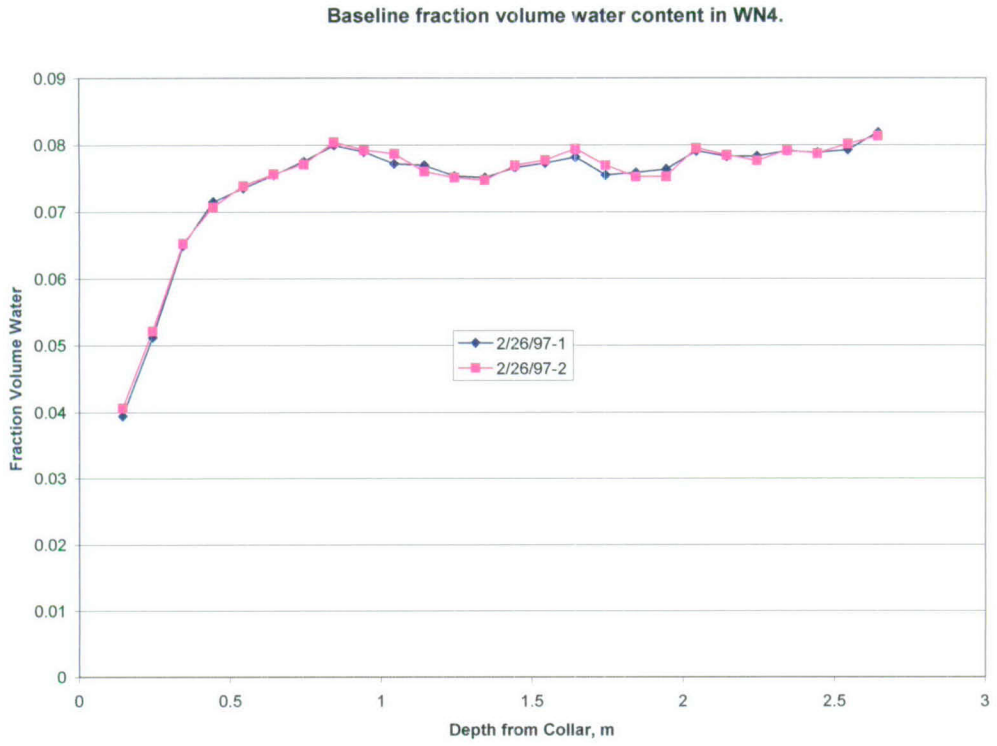

Figure 6-26. The Baseline Moisture Content Measured in Hole WN4 as a Function of Depth from the West Face of the Block

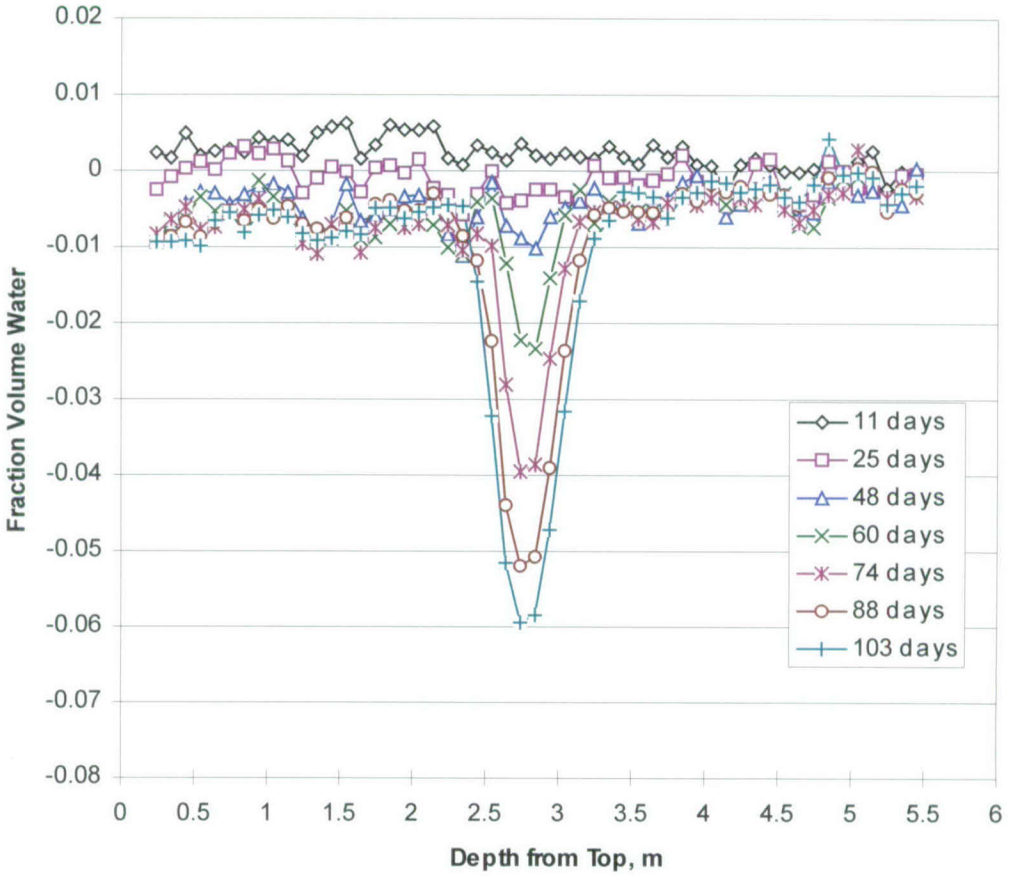

NOTE: Between the in-test and the baseline as a function of depth from the top of the block.

Figure 6-27. Difference Fraction Volume Water in Hole TN1 from March 11, 1997, to June 11, 1997

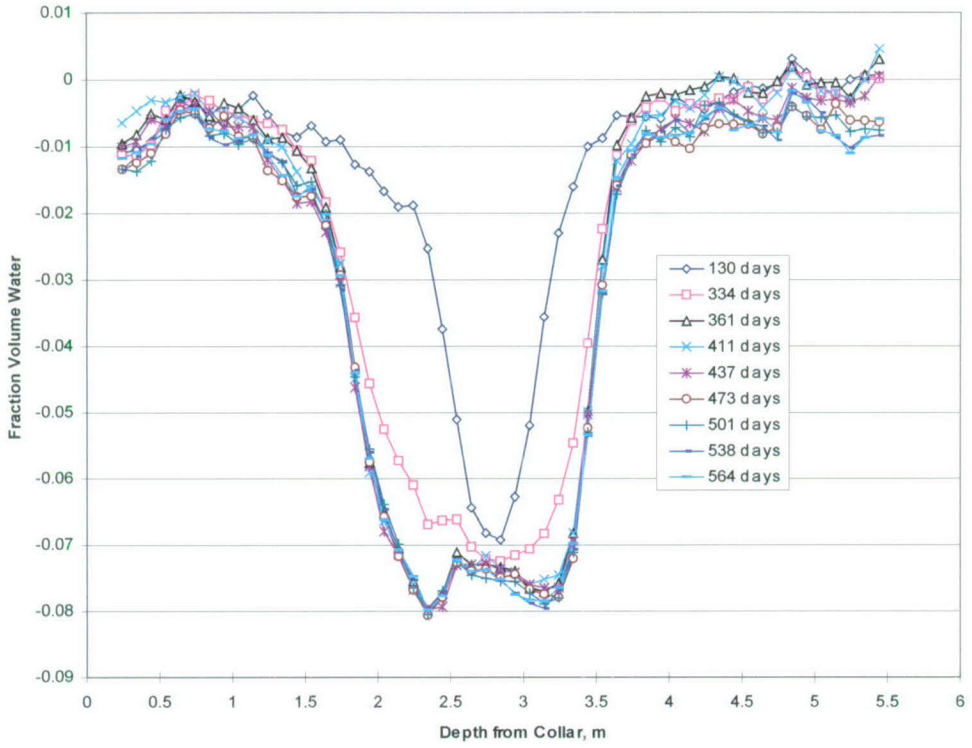

Figure 6-28. Difference Fraction Volume Water, Between the In-heat and the Baseline, in Hole TN1 as a Function of Depth from Top of the Block, from June 8, 1997, to September 15, 1998.

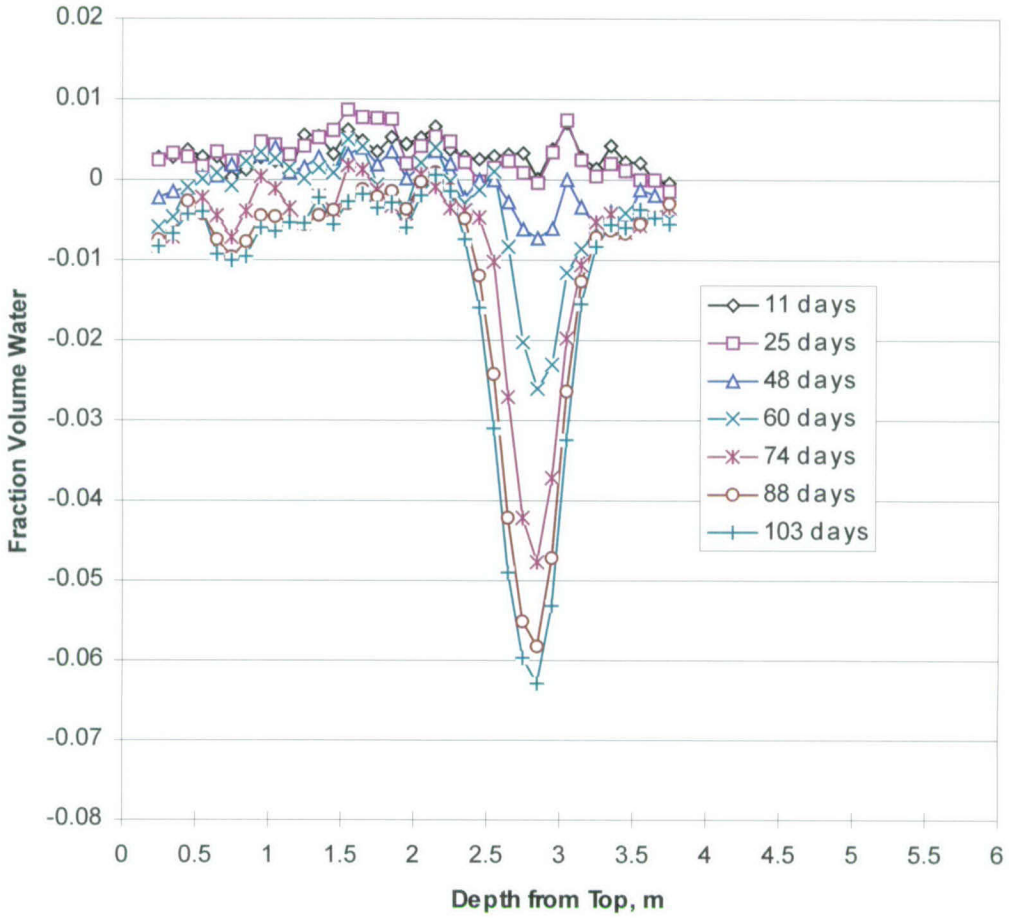

Figure 6-29. Difference Fraction Volume Water, Between the In-heat and the Baseline, in Hole TN2 as a Function of Depth from Top of the Block, from March 11, 1997, to June 11, 1997

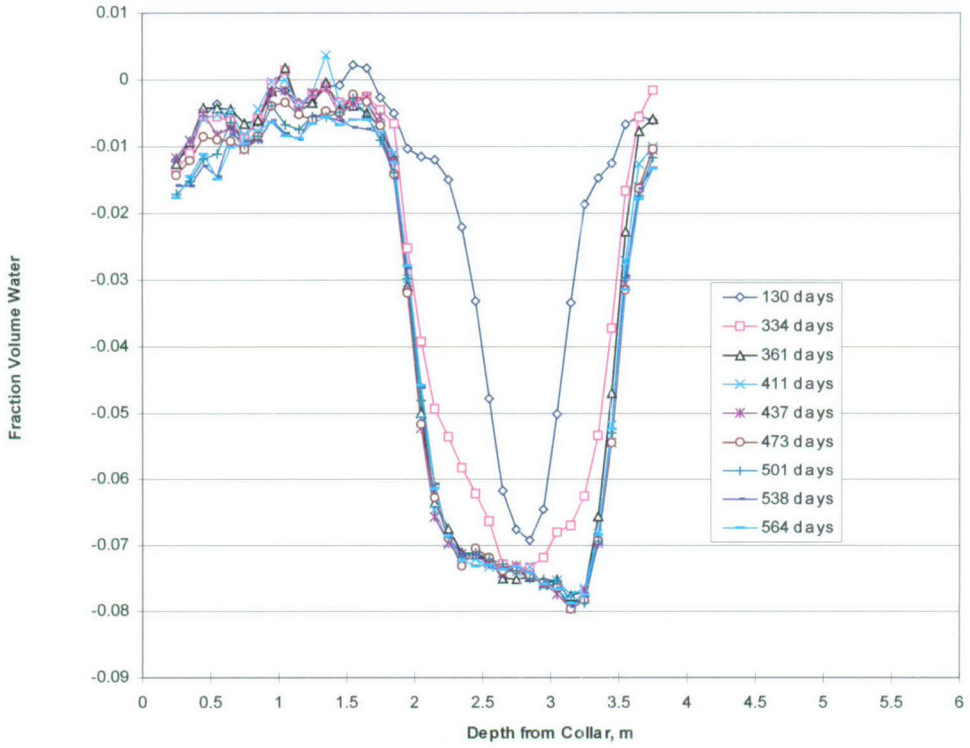

Figure 6-30. Difference Fraction Volume Water, Between the In-heat and the Baseline, in Hole TN2 as a Function of Depth from Top of the Block, from July 8, 1997, to September 15, 1998

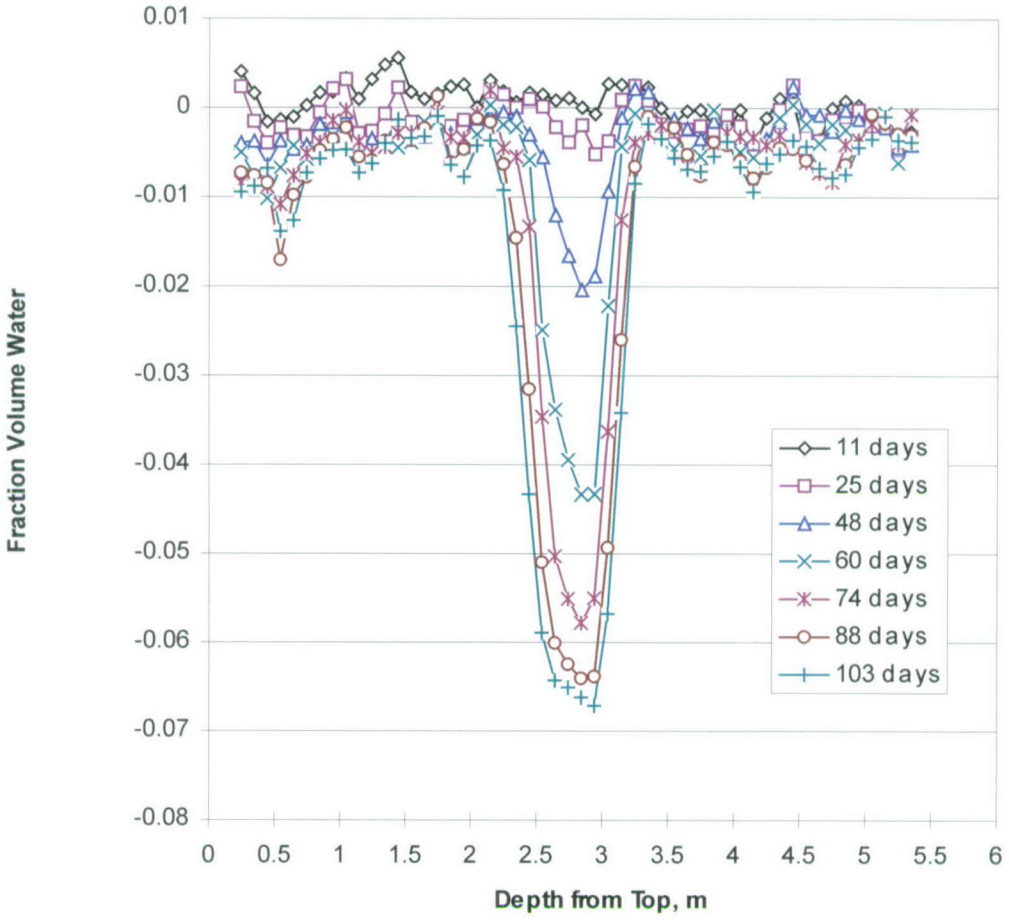

Figure 6-31. Difference Fraction Volume Water, Between the In-heat and the Baseline, in Hole TN3 as a Function of Depth from Top of the Block, from March 11, 1997, to June 11, 1997

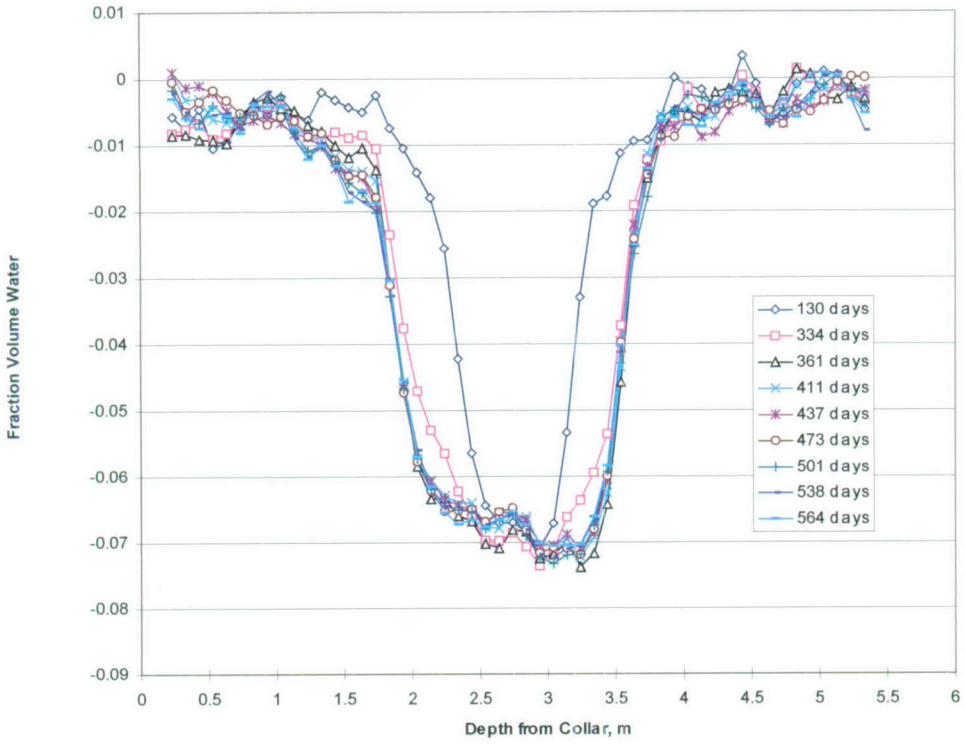

Figure 6-32. Difference Fraction Volume Water, Between the In-heat and the Baseline, in Hole TN3 as a Function of Depth from Top of the Block, from July 8, 1997, to September 15, 1998

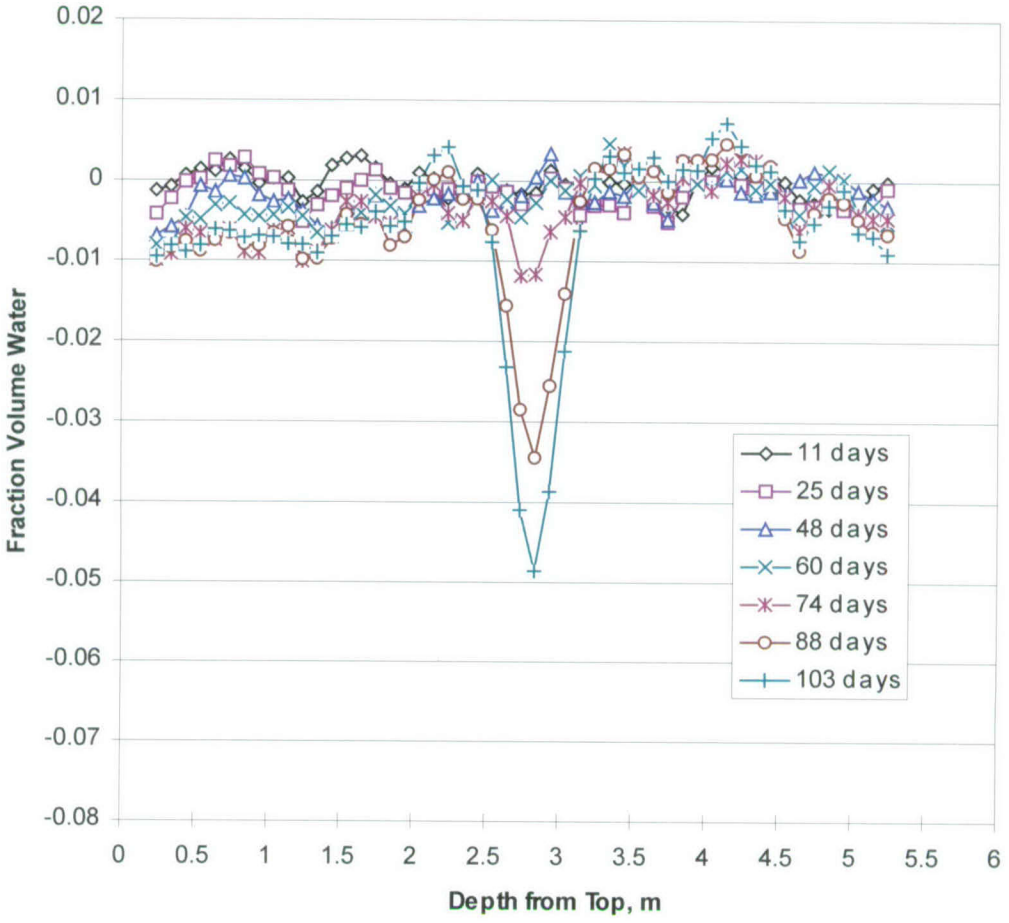

Figure 6-33. Difference Fraction Volume Water, Between the In-heat and the Baseline, in Hole TN4 as a Function of Depth from Top of the Block, from March 11, 1997, to June 11, 1997

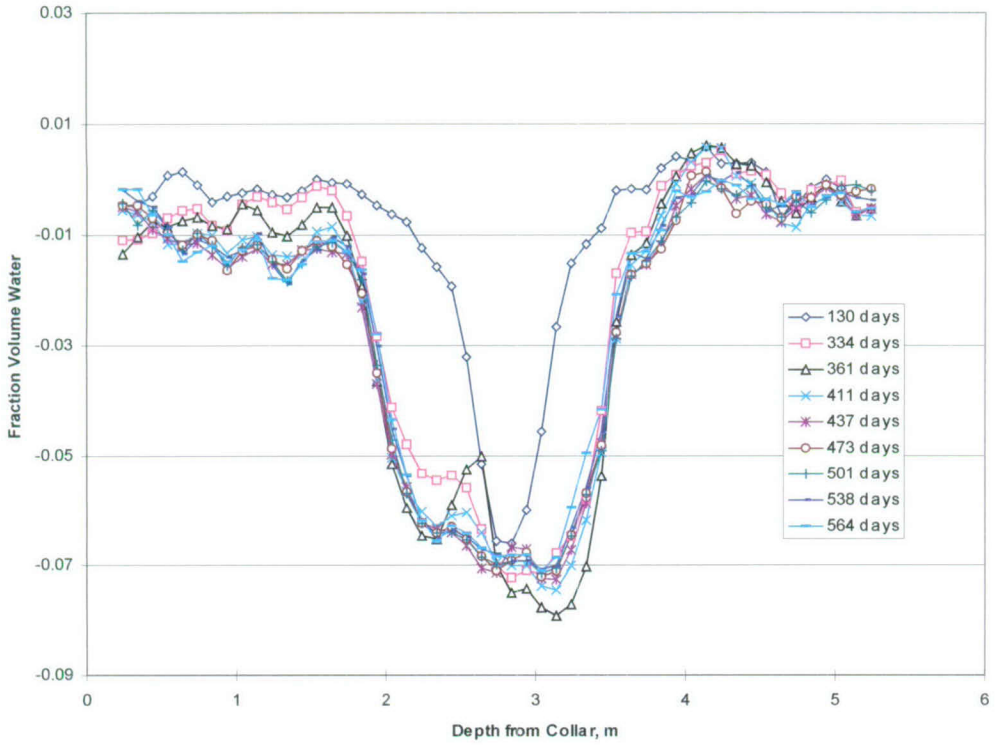

Figure 6-34. Difference Fraction Volume Water, Between the In-heat and the Baseline, in Hole TN4 as a Function of Depth from Top of the Block, from July 8, 1997, to September 15, 1998

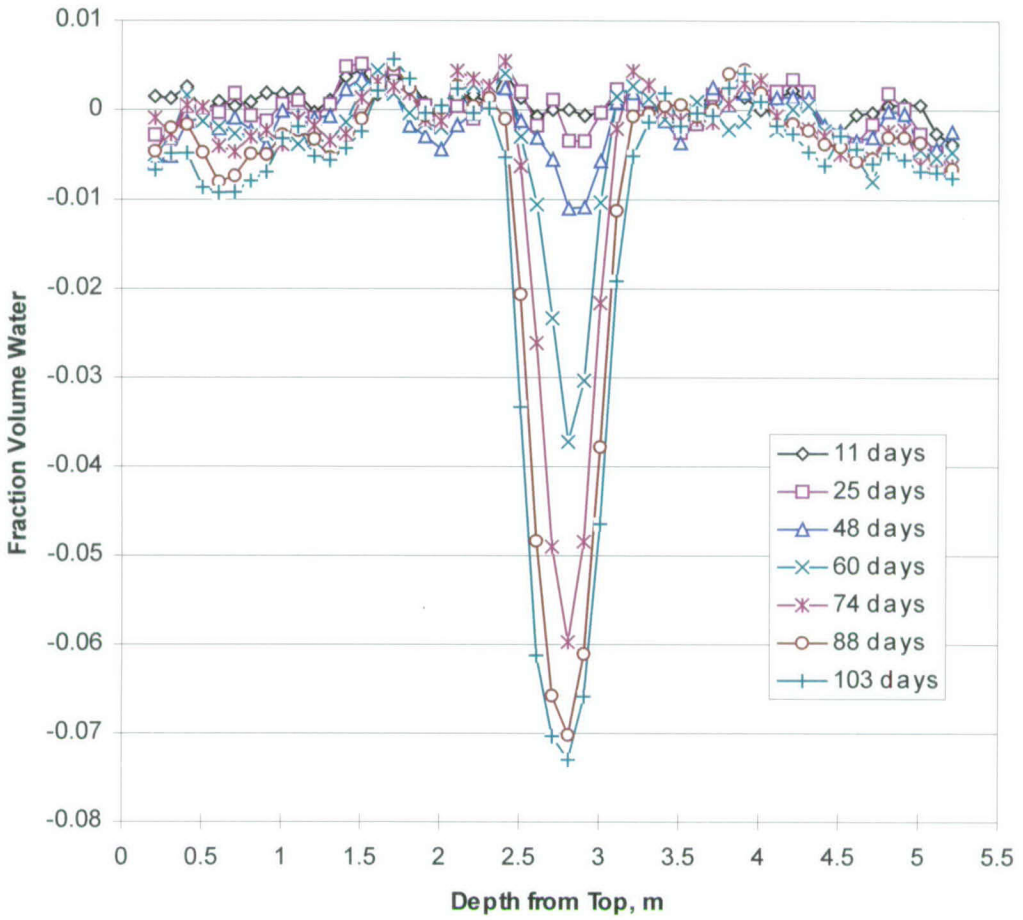

Figure 6-35. Difference Fraction Volume Water, Between the In-heat and the Baseline, in Hole TN5 as a Function of Depth from Top of the Block, from March 11, 1997 to June 11, 1997

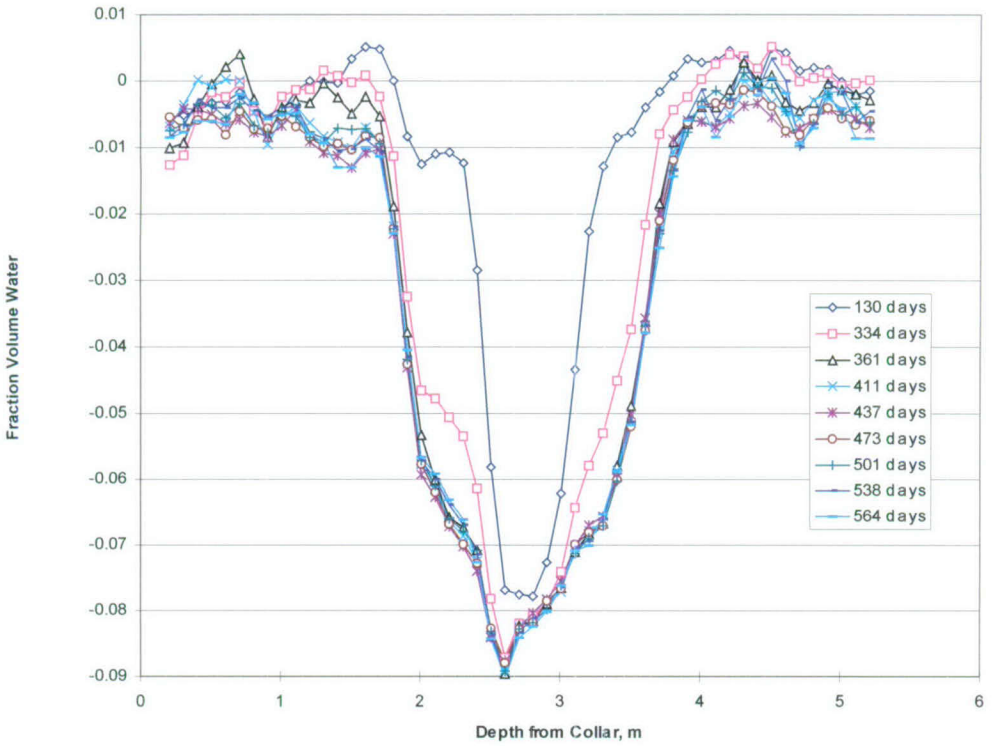

Figure 6-36. Difference Fraction Volume Water, Between the In-heat and the Baseline, in Hole TN5 as a Function of Depth from Top of the Block, from July 8, 1997, to September 15, 1998

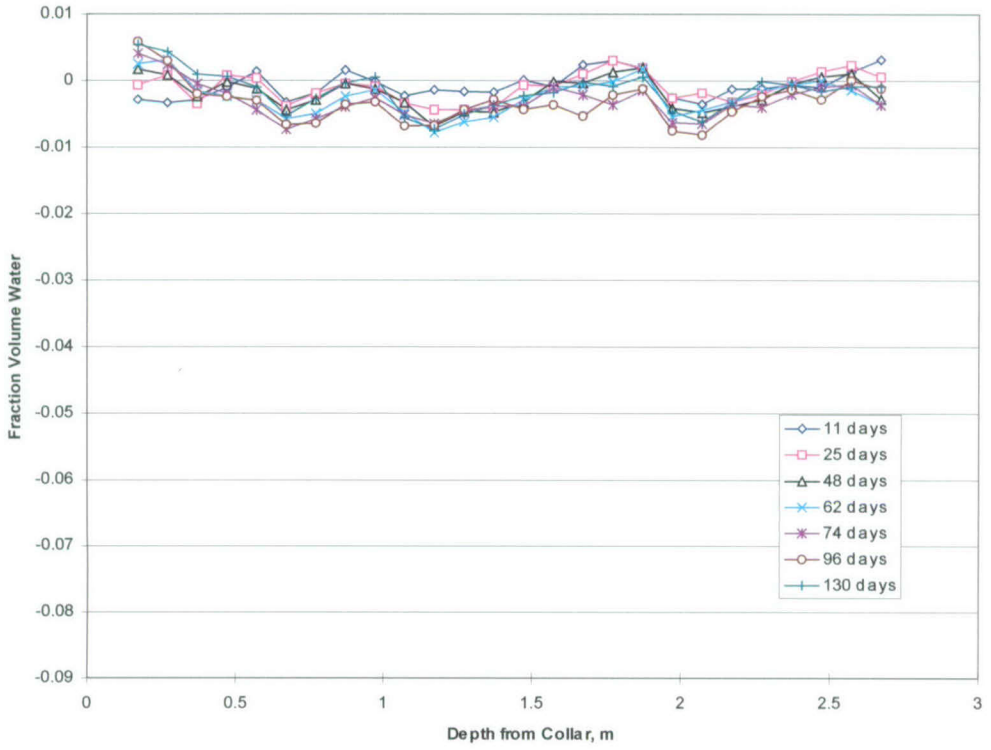

Figure 6-37. Difference Fraction Volume Water, Between the In-heat and the Baseline, in Hole NN1 as a Function of Depth from the North Face of the Block, from March 11, 1997, to July 8, 1997

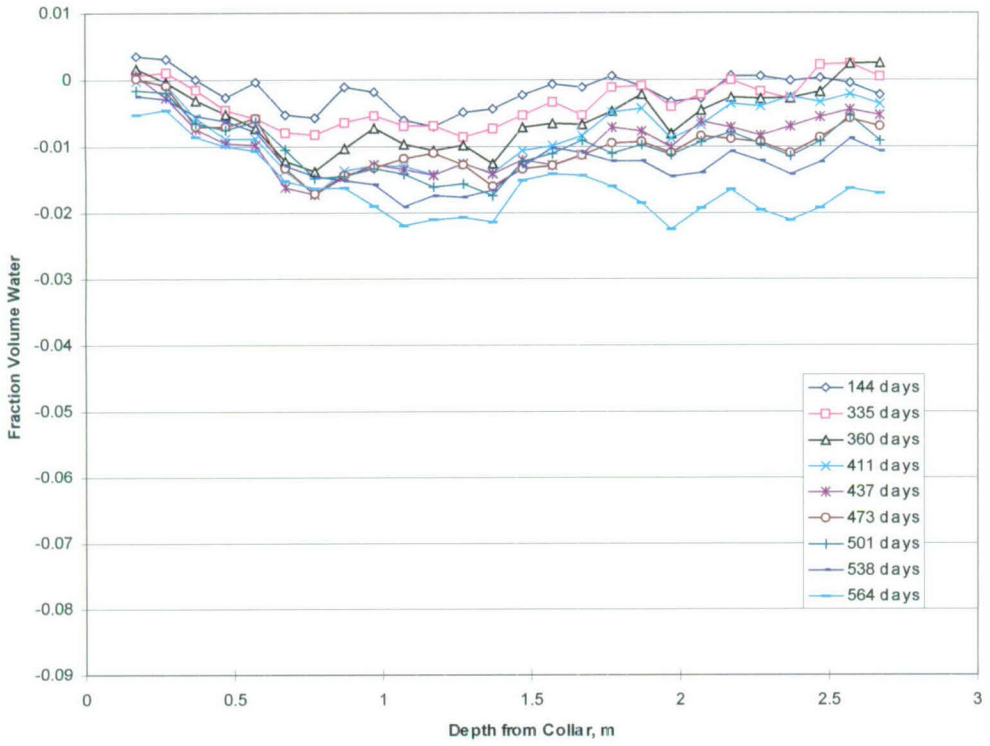

Figure 6-38. Difference Fraction Volume Water, Between the In-heat and the Baseline, in Hole NN1 as a Function of Depth from the North Face of the Block, from July 22, 1997, September 15, 1998

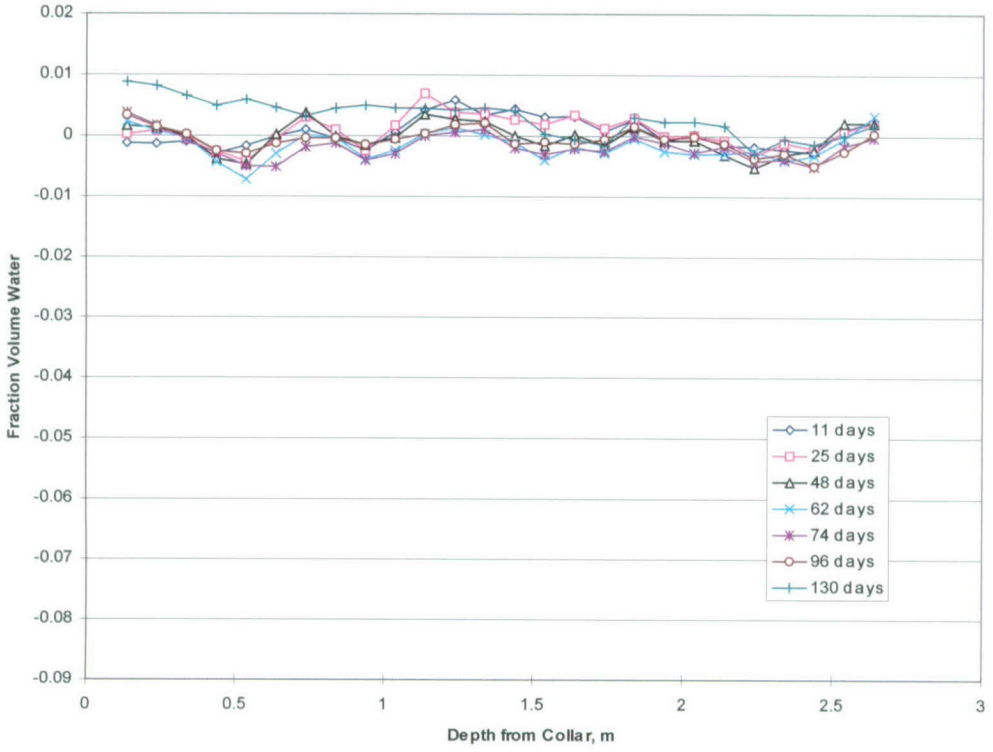

Figure 6-39. Difference Fraction Volume Water, Between the In-heat and the Baseline, in Hole NN2 as a Function of Depth from the North Face of the Block, from March 11, 1997, to July 8, 1997

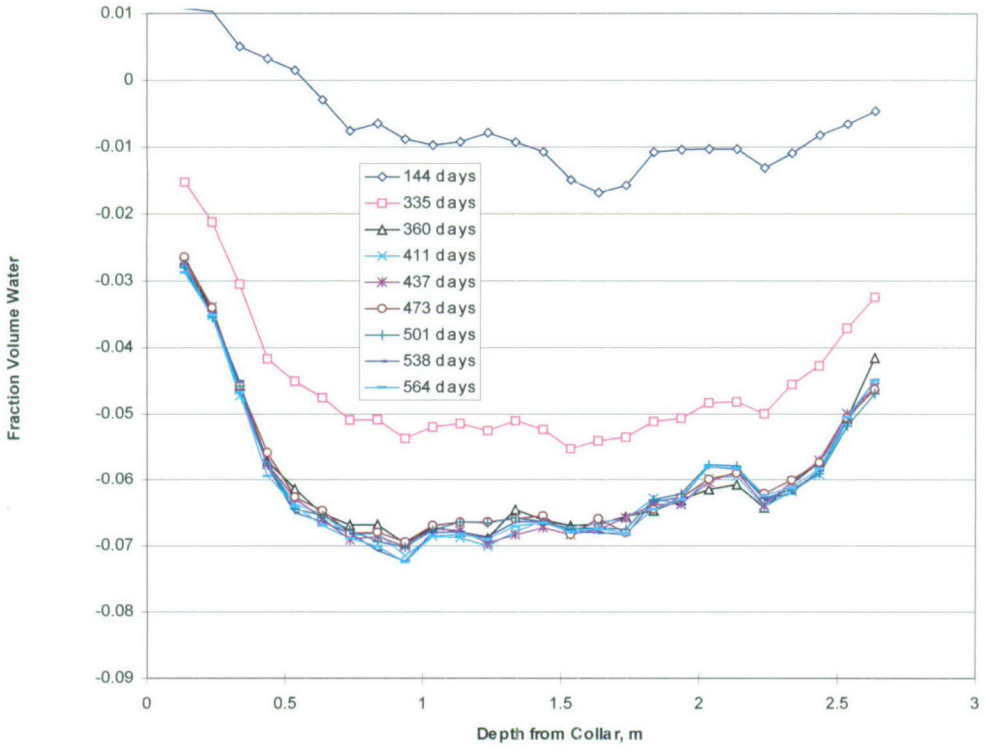

Figure 6-40. Difference Fraction Volume Water, Between the In-heat and the Baseline, in Hole NN2 as a Function of Depth from the North Face of the Block, from July 22, 1997, to September 15, 1998

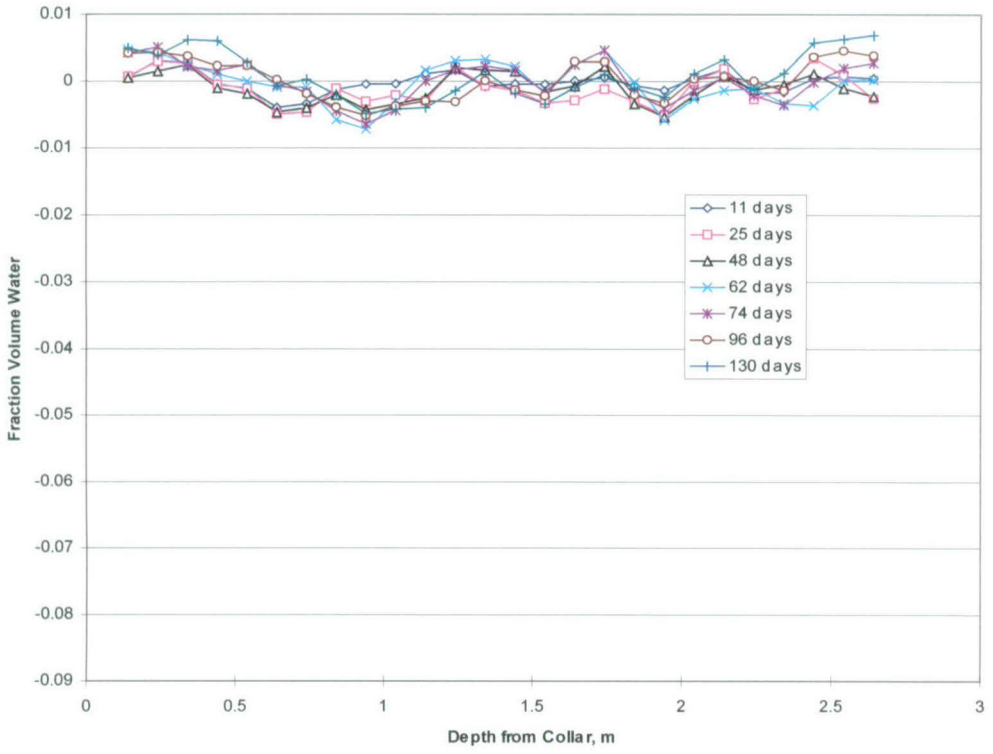

Figure 6-41. Difference Fraction Volume Water, Between the In-heat and the Baseline, in Hole NN3 as a Function of Depth from the North Face of the Block, from March 11, 1997, to July 8, 1997

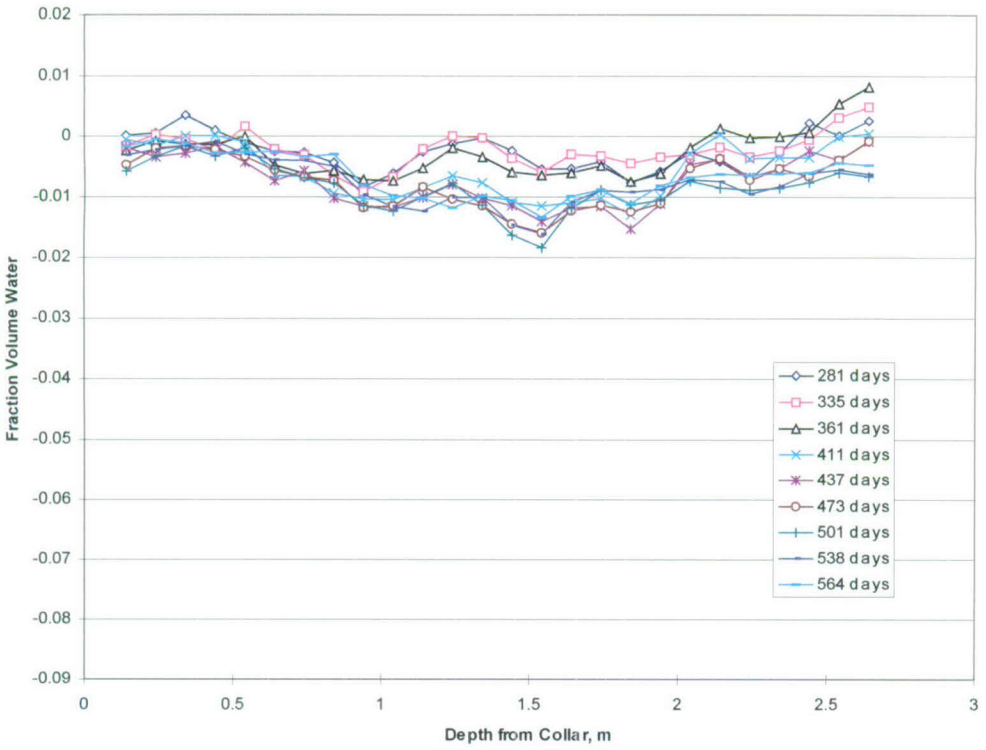

Figure 6-42. Difference Fraction Volume Water, Between the In-heat and the Baseline, in Hole NN3 as a Function of Depth from the North Face of the Block, from November 6, 1997, to September 15, 1998

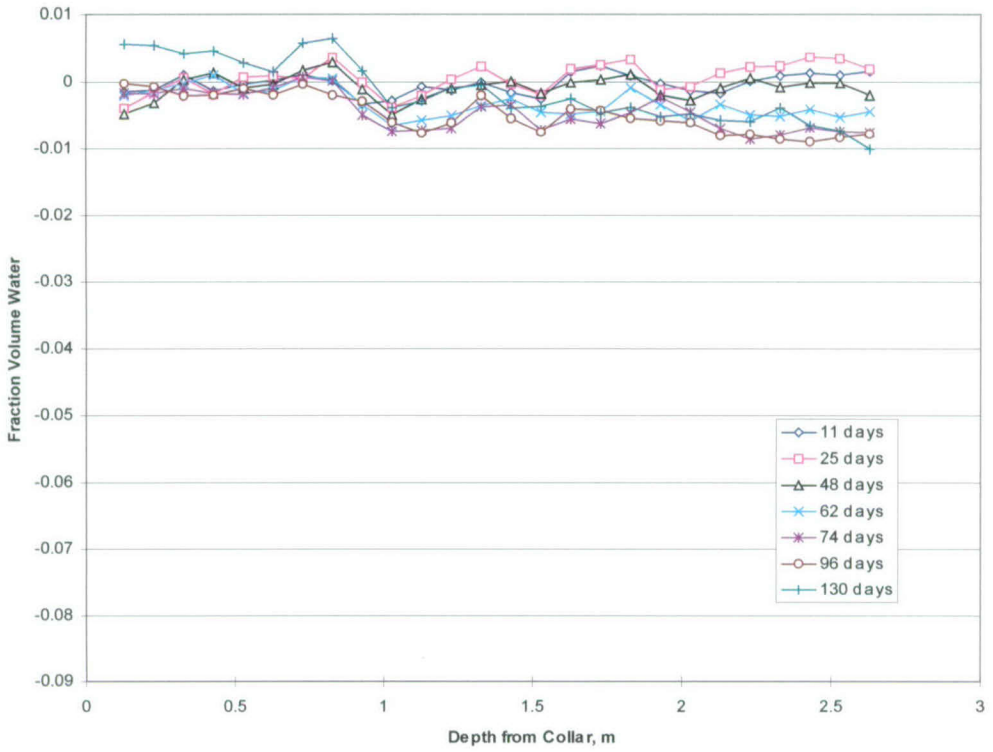

Figure 6-43. Difference Fraction Volume Water, Between the In-heat and the Baseline, in Hole NN4 as a Function of Depth from the North Face of the Block, from March 11, 1997, to July 8, 1997

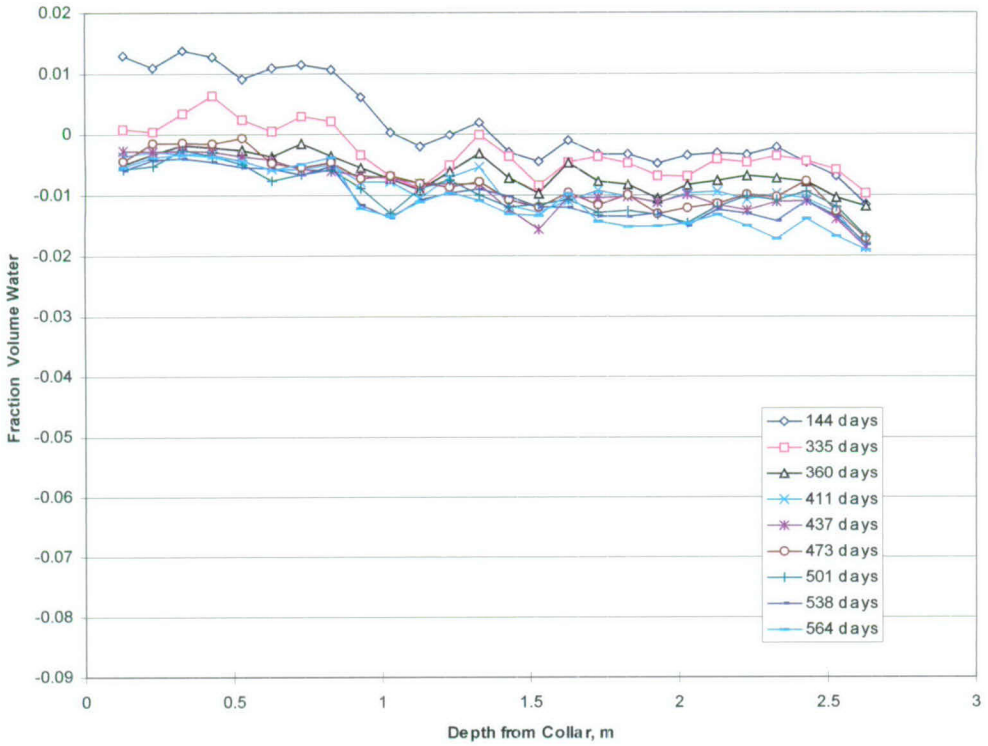

Figure 6-44. Difference Fraction Volume Water, Between the In-heat and the Baseline, in Hole NN4 as a Function of Depth from the North Face of the Block, from July 22, 1997, to September 15, 1998

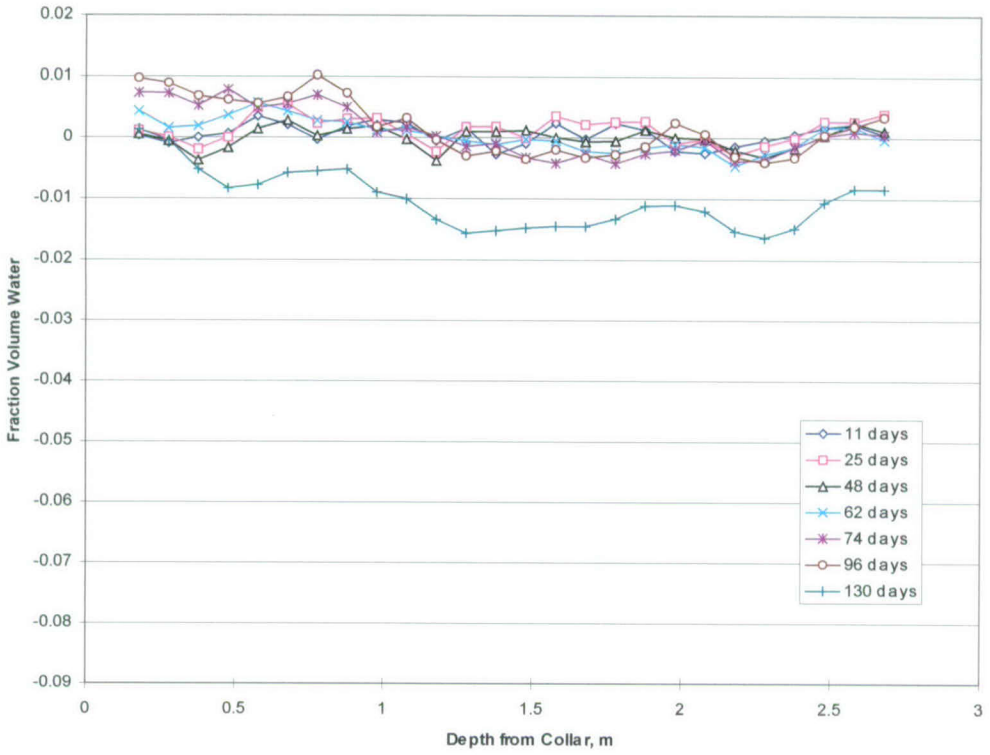

Figure 6-45. Difference Fraction Volume Water, Between the In-heat and the Baseline, in Hole NN5 as a Function of Depth from the North Face of the Block, from March 11, 1997, to July 8, 1997

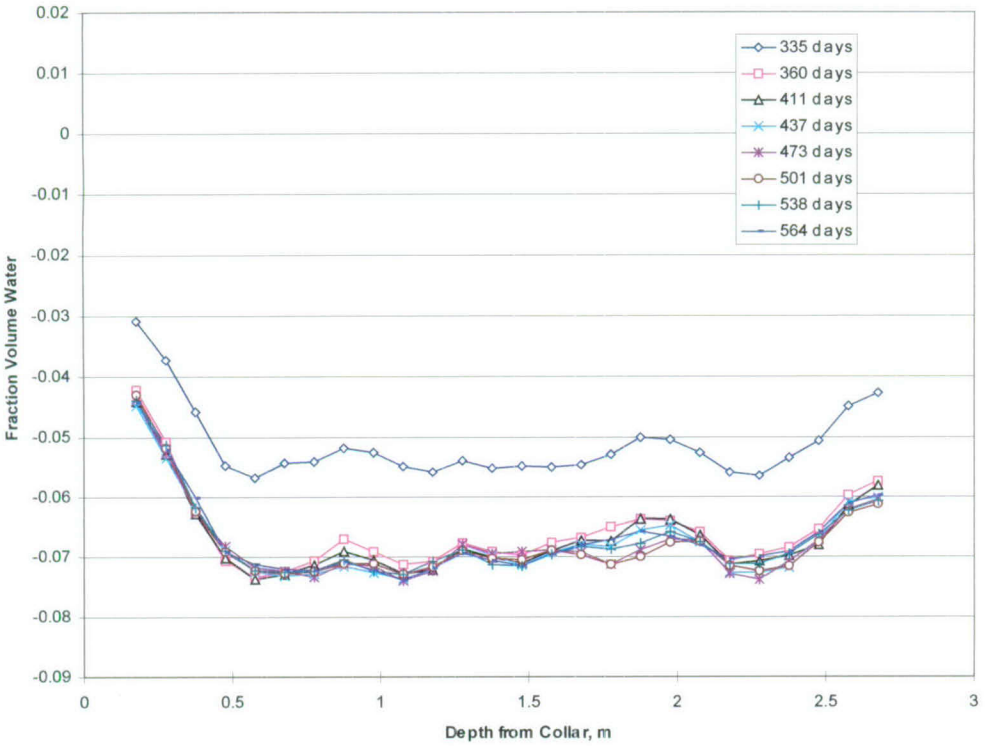

Figure 6-46. Difference Fraction Volume Water, Between the In-heat and the Baseline, in Hole NN5 as a Function of Depth from the North Face of the Block, from January 29, 1998, to September 15, 1998

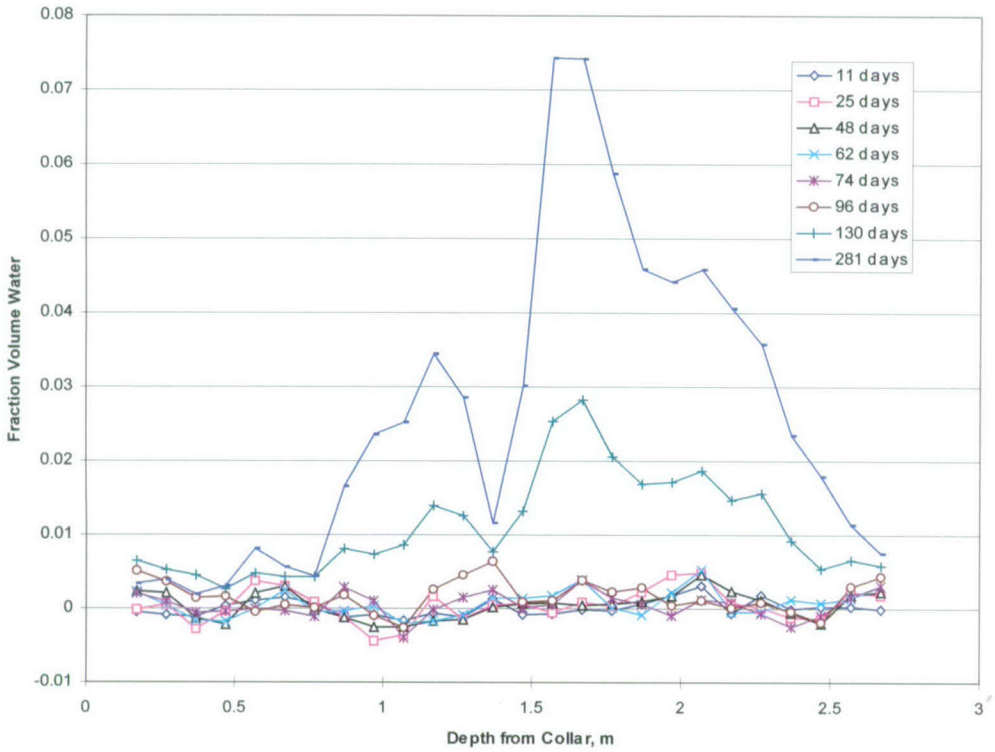

Figure 6-47. Difference Fraction Volume Water, Between the In-test and the Baseline as a Function of Depth from the North face of the Block, in Hole NN6 from March 11, 1997, to November 6, 1997

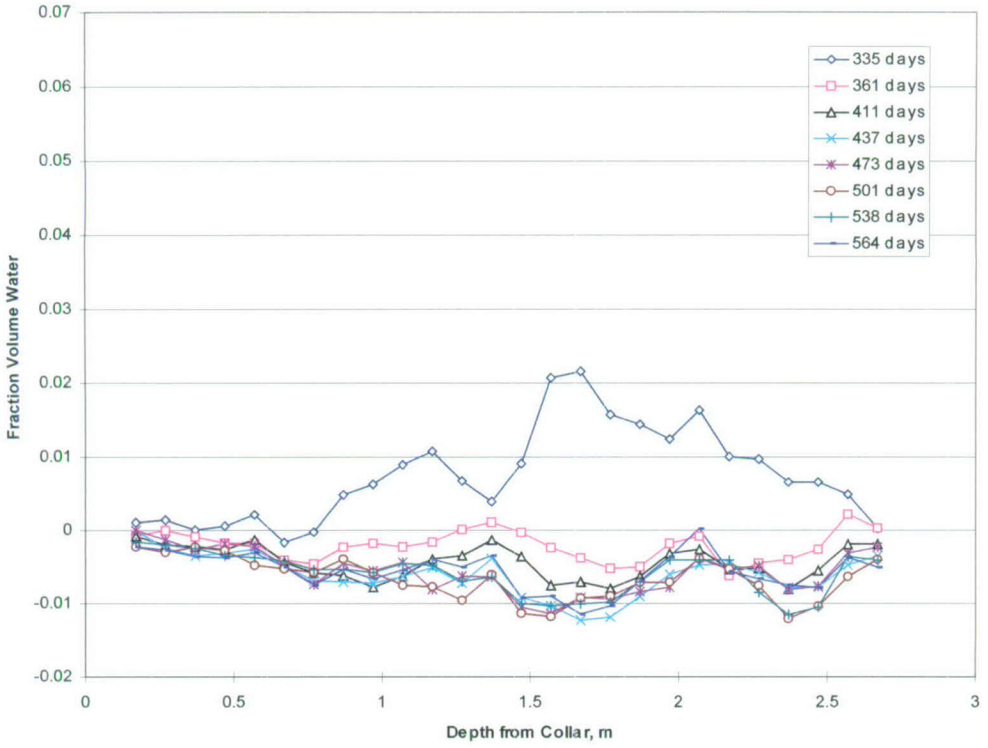

Figure 6-48. Difference Fraction Volume Water, Between the In-heat and the Baseline, in Hole NN6 as a Function of Depth from the North Face of the Block, from January 29, 1998, to September 15, 1998

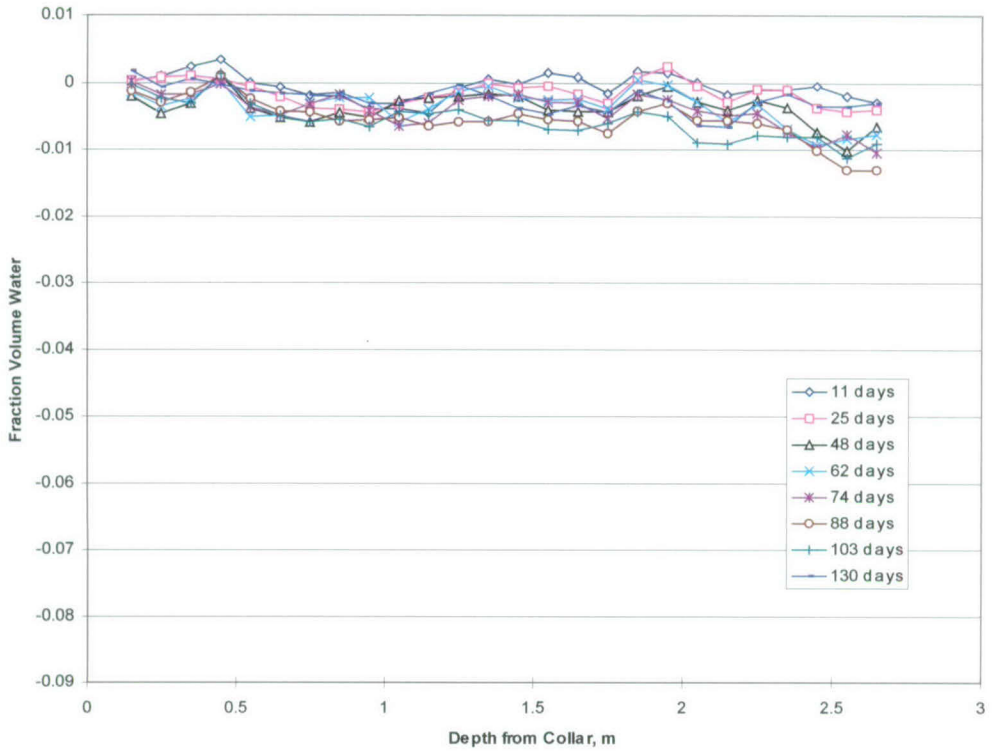

Figure 6-49. Difference Fraction Volume Water, Between the In-heat and the Baseline, in Hole WN1 as a Function of Depth from the West Face of the Block, from March 11, 1998, to July 8, 1997

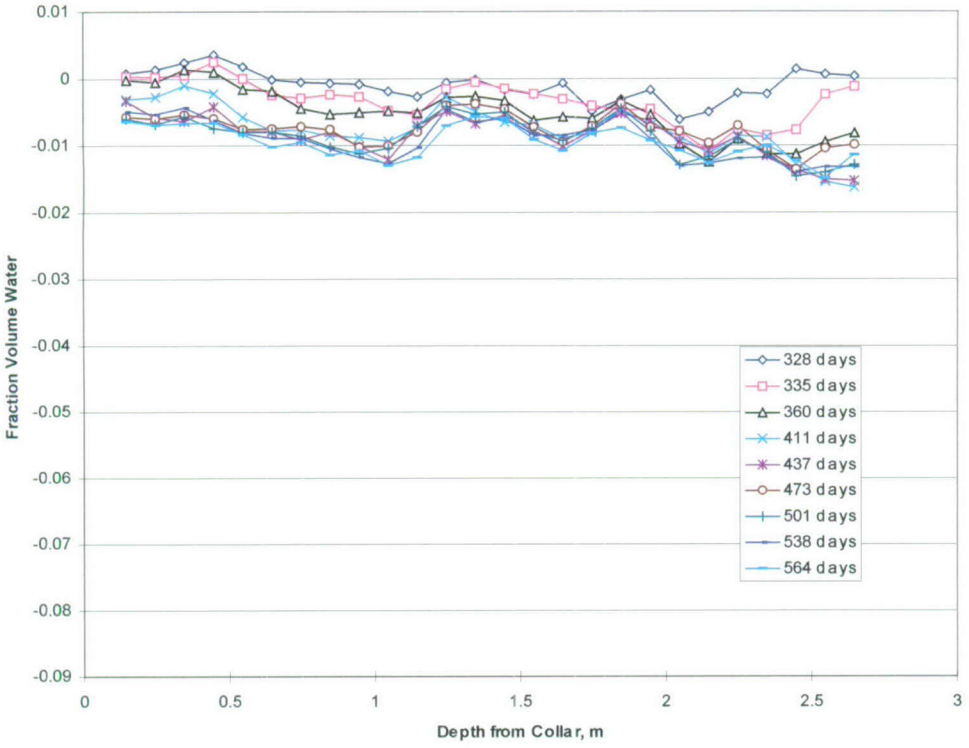

Figure 6-50. Difference Fraction Volume Water, Between the In-heat and the Baseline, in Hole WN1 as a Function of Depth from the West Face of the Block, from January 22, 1998, to September 15, 1998

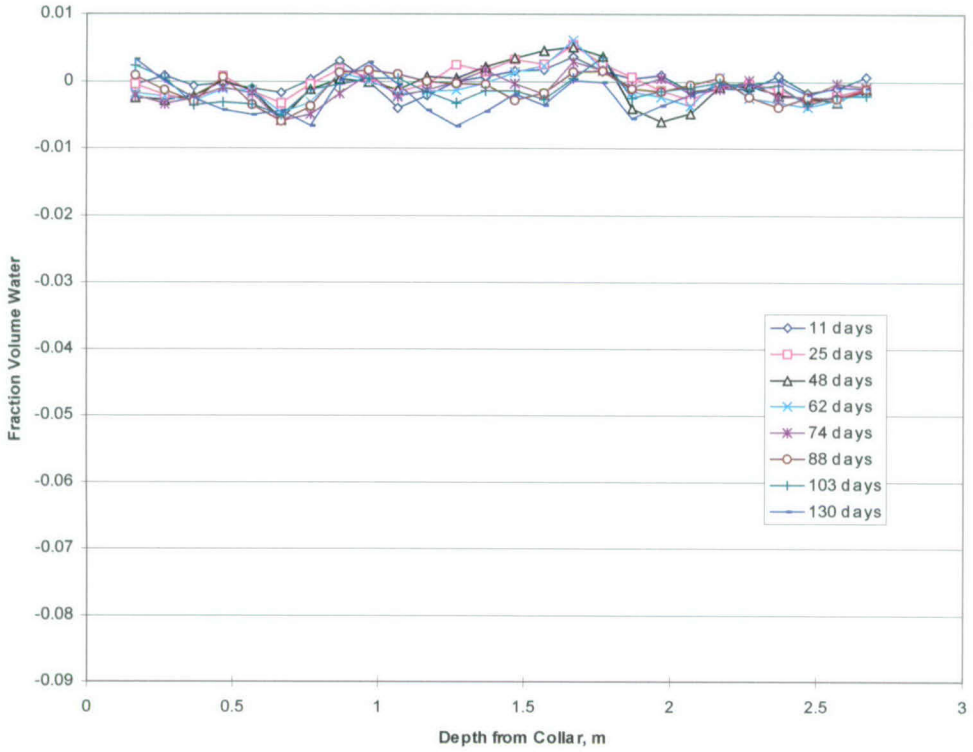

Figure 6-51. Difference Fraction Volume Water, Between the In-heat and the Baseline, in Hole WN2 as a Function of Depth from the West Face of the Block, from March 11, 1997, to July 8, 1997

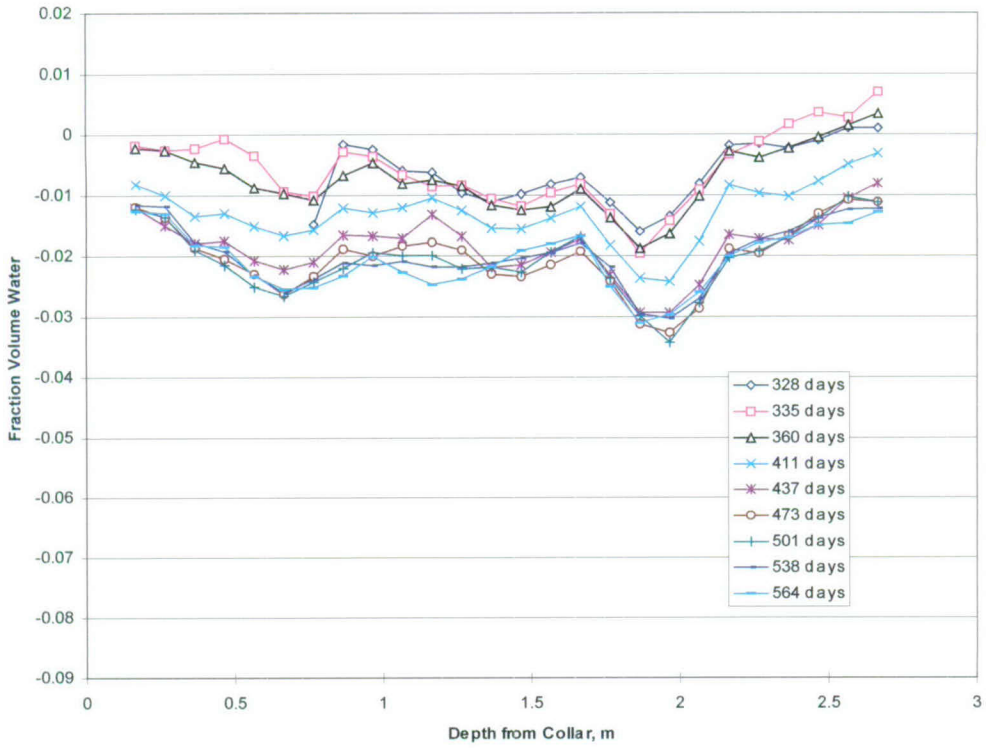

Figure 6-52. Difference Fracture Volume Water, Between the In-heat and the Baseline, in Hole WN2 as a Function of Depth from the West Face of the Block, from January 22, 1998, to September 15, 1998

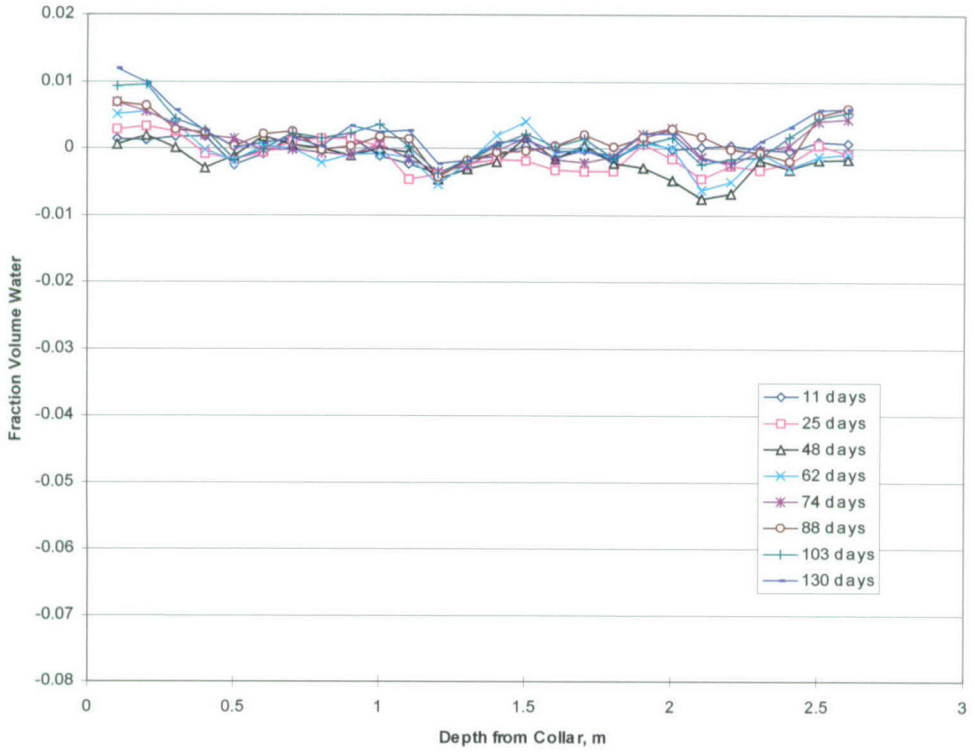

Figure 6-53. Difference Fraction Volume Water, Between the In-heat and the Baseline, in Hole WN3 as a Function of Depth from the West Face of the Block, from March 11, 1997, to July 8, 1997

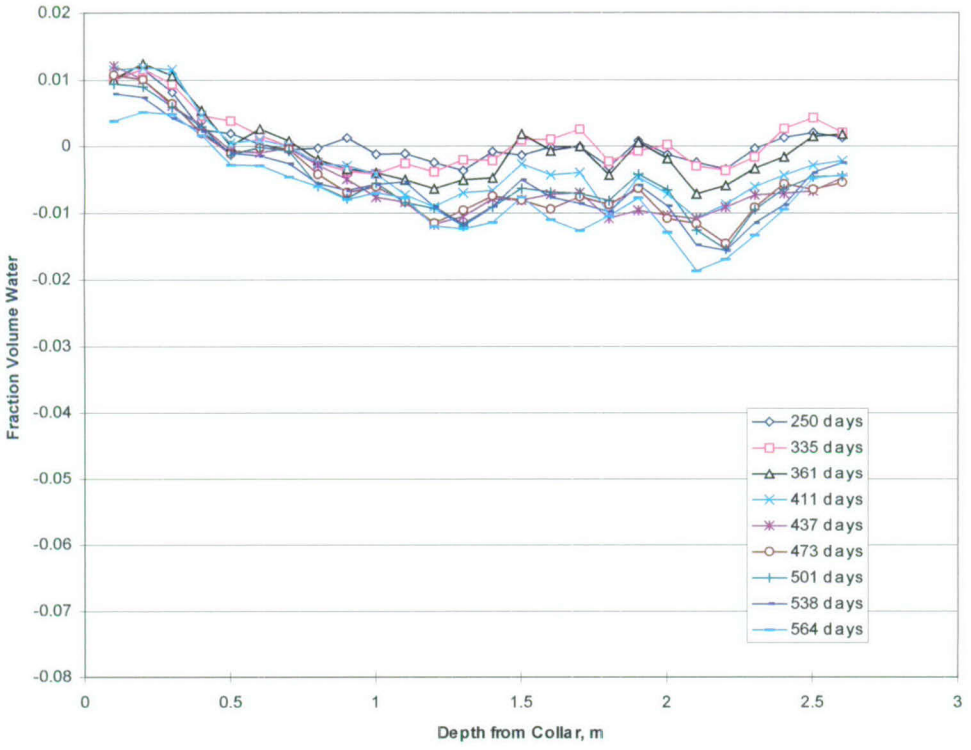

Figure 6-54. Difference Fraction Volume Water, Between the In-heat and the Baseline, in Hole WN3 as a Function of Depth from the West Face of the Block, from November 5, 1997, to September 15, 1998

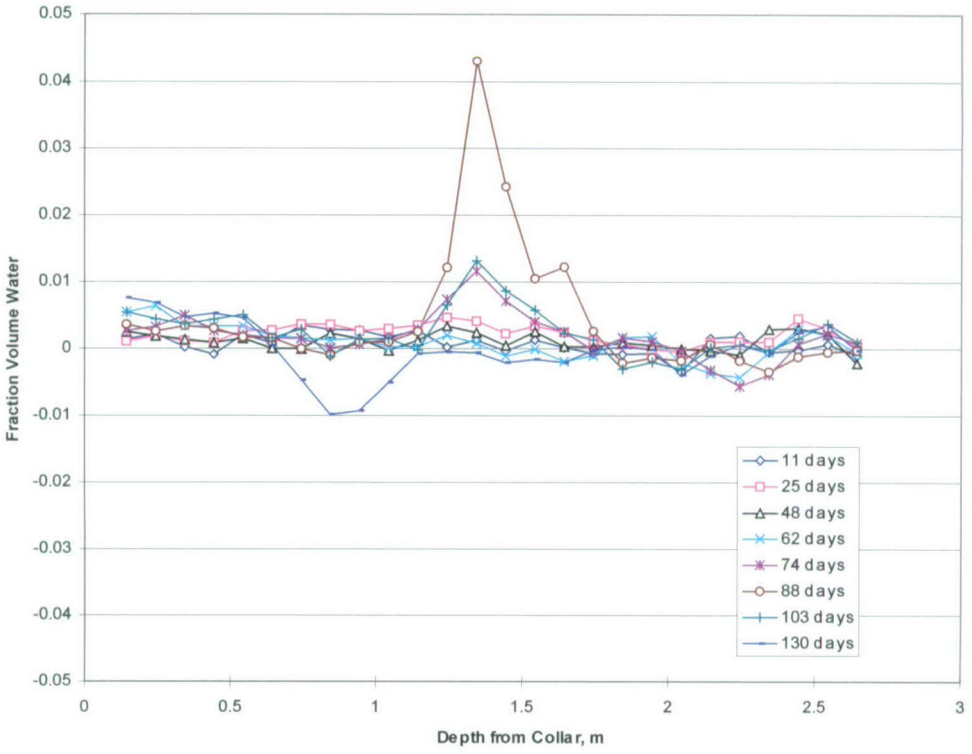

Figure 6-55. Difference Fraction Volume Water, Between the In-heat and the Baseline, in Hole WN4 as a Function of Depth from the West Face of the Block, from March 11, 1997, to July 8, 1997

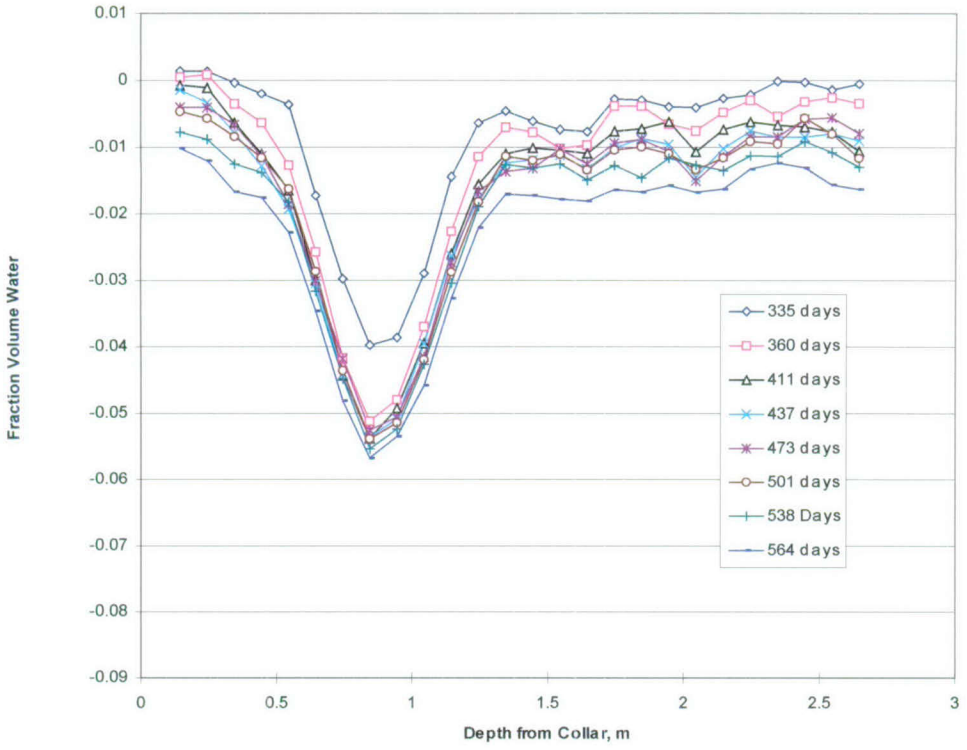

Figure 6-56. Difference Fraction Volume Water, Between the In-heat and the Baseline, in Hole WN4 as a Function of Depth from the West Face of the Block, from January 29, 1998, to September 15, 1998

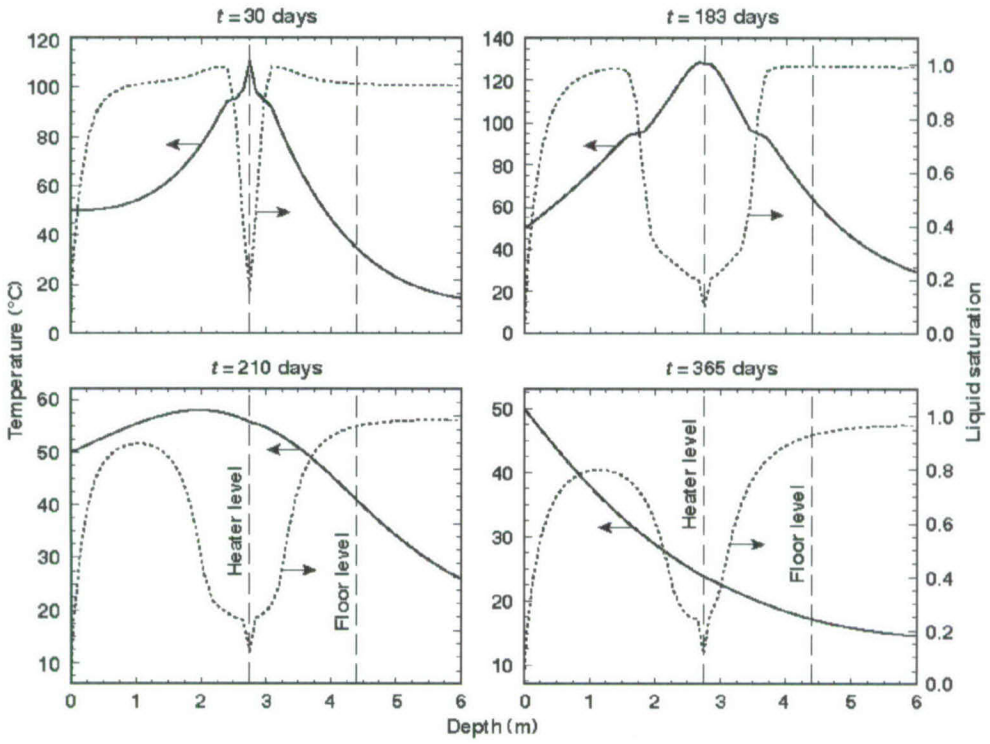

Figure 6-57. Pre-test Temperature and Liquid Saturation Calculated in Model Case A

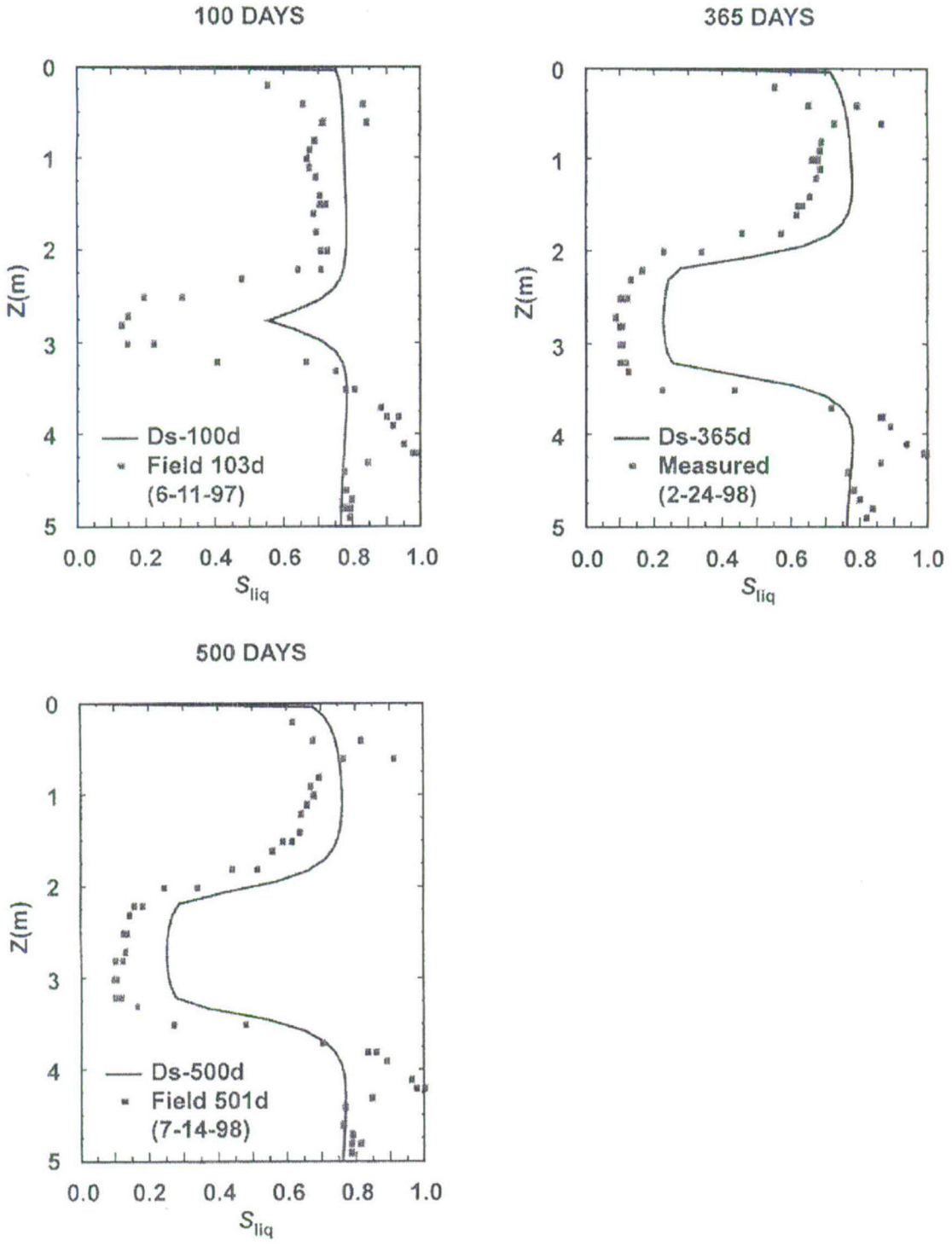

Figure 6-58. The Moisture Content Measured by Neutron in Hole TN3 Compared with the Model Calculations Using DS Property Set

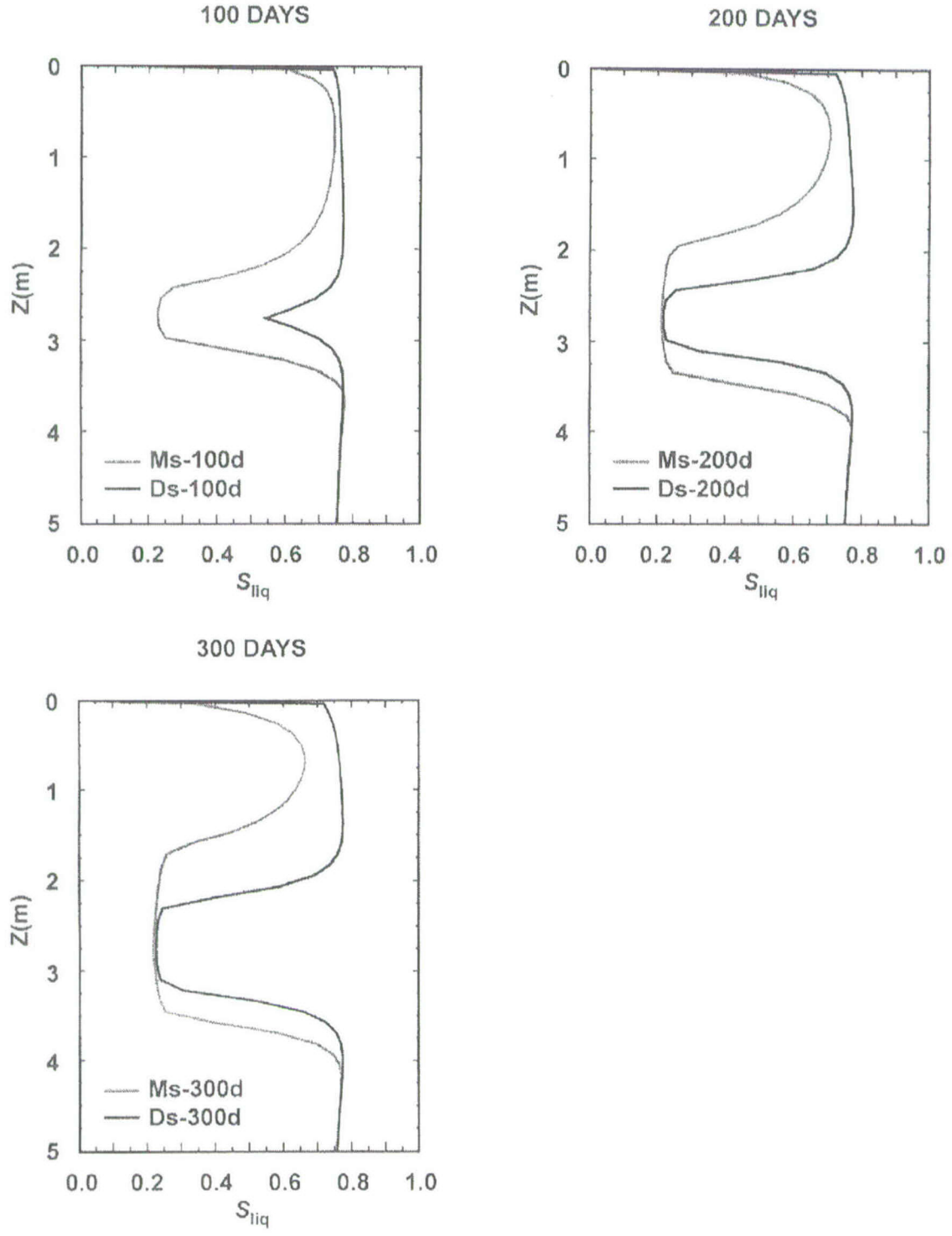

Figure 6-59. Comparison of Calculated Liquid Saturation of the LBT Along Hole TN3 Using MS Property Set and DS Property Set

7. GEOMECHANICS OF THE LBT

7.1 DEFORMATION MEASUREMENTS

7.1.1 Introduction

Six multiple-point borehole extensometers (MPBX) were deployed in the LBT. Each extensometer consisted of three or four borehole anchors connected to a surface collar by invar rods (Figure 7-1). The extensometers measured linear displacement relative to the surface collar. Linear variable differential transformers (LVDT) were used to measure the linear displacement. Extensometer TM-1 was emplaced in a vertical borehole, and the others were emplaced in horizontal boreholes, of which three were oriented north-south and two were oriented east-west (Figure 7-2, which is the same as Figure 3-13 but has been included again for easier reading.). The surface collars were located on the top, north and west faces. The first letter in the extensometer name denotes the face on which the surface collar is located. The anchors are numbered such that anchor 1 is nearest and anchor 4 is farthest from the collar. One of the north-south MPBX systems, NM-2, was emplaced slightly above the heater plane. The other horizontal MPBX systems were deployed as two orthogonal pairs, one pair near the base of the large block (NM-1 and WM-1) and the other pair (NM-3 and WM-2) about 1 m below the top. The horizontal MPBX systems spanned baselines of about 2.6 m. The vertical MPBX was a little more than twice as long. The extensometer collar and anchor coordinates are given in Table 7-1. The orientations, baseline lengths, and number of anchors of the MPBX systems are summarized in Table 7-2. An extensometer collar is shown in Figure 7-3.

Pre-heat MPBX measurements were conducted for several days before the heaters were energized on February 28, 1997. The LVDTs were zeroed before the heating was started. All of the extensometers performed well during the first few weeks, but problems developed over time beginning with NM-2, which is located near the heater plane. This extensometer failed early in the test and may have been adversely affected by high temperatures. Evidence of corrosion was noted on some of the invar rods in this hole at the conclusion of the LBT (Figure 7-4). The corrosion on the invar rods did not impact the mechanical integrity of the rods. Most of the extensometers performed well during the first 100 days of the test, during which temperatures rose rapidly and the largest thermal expansions occurred. The data from the first 100 days will therefore be examined in somewhat greater detail than those from the remainder of the test. Several extensometer transducers were replaced prior to cool-down, so that the large contractions that occurred after 375 days have also been captured. The data during the intermediate period, 100 to 375 days, are incomplete because of mechanical problems, but one extensometer, WM-2, performed well throughout the entire test, and its data provide a nearly continuous record of east-west deformation in the upper portion of the block.

7.1.1.1 The First 100 Days

The MPBX data show that the large block began expanding within hours after heating began. Horizontal displacements at selected days during the first two weeks are shown as a function of depth in Figure 7-5. These displacements are measured in different directions, either east-west (WM-1, WM-2) or north-south (NM-1, NM-2, NM-3). The lines are drawn as an aid to the eye only. The expansion at the heater plane level exceeded that measured elsewhere in the block

Table 7-1. MPBX Extensometer Collar and Anchor Coordinates. The Origin of the Coordinates Is the Southwestern Corner on Top of the Block

MPBX	Anchor	Serial No.	Calibration factor	Distance (m)	x (m)	y (m)	z (m)	Comment
NM-1	collar	--	--	0.000	2.743	3.048	-3.851	
	1	10515	9.65E-05	0.832	2.743	2.216	-3.851	
	2	12217	9.72E-05	1.595	2.743	1.453	-3.851	
	3	12218	9.59E-05	2.159	2.743	0.889	-3.851	
	4	12219	9.46E-05	2.616	2.743	0.432	-3.851	
NM-2	collar	--	--	0.000	0.911	3.048	-2.467	
	1	10535	9.60E-05	0.832	0.911	2.216	-2.467	removed
	2	10521	9.60E-05	1.595	0.911	1.453	-2.467	removed
	3	10526	9.62E-05	2.159	0.911	0.889	-2.467	removed
	4	10530	9.59E-05	2.616	0.911	0.432	-2.467	removed
NM-3	collar	--	--	0.000	0.314	3.048	-0.930	
	1	12224	9.61E-05	0.832	0.314	2.216	-0.930	
	2	12225	9.70E-05	1.595	0.314	1.453	-0.930	
	3	12226	9.60E-05	2.159	0.314	0.889	-0.930	
	4	12228	9.50E-05	2.616	0.314	0.432	-0.930	
WM-1	collar	--	--	0.000	0.000	2.172	-3.985	
	1	12227	9.61E-05	0.872	0.872	2.172	-3.985	
	3	10536	9.64E-05	2.086	2.086	2.172	-3.985	
	4	10517	9.51E-05	2.650	2.650	2.172	-3.985	
WM-2	collar	--	--	0.000	0.000	0.619	-1.235	
	1	10519	9.63E-05	0.832	0.832	0.619	-1.235	
	2	10527	9.57E-05	1.595	1.595	0.619	-1.235	
	3	10538	9.65E-05	2.159	2.159	0.619	-1.235	
	4	10534	9.52E-05	2.616	2.616	0.619	-1.235	
TM-1	collar	--	--	0.000	1.453	1.227	0.000	
	1	10518	9.51E-05	1.600	1.453	1.227	-1.600	
	2	10533	9.59E-05	3.124	1.453	1.227	-3.124	
	3	10528	9.45E-05	4.347	1.453	1.227	-4.347	
	4	10532	9.71E-05	5.413	1.453	1.227	-5.413	

Table 7-2. MPBX Orientations, Baseline Lengths, and Number of Anchors

Name	Orientation	Baseline length (m)	Anchors	Comment
NM-1	North-south	2.616	4	Near east face
NM-2	North-south	2.616	4	Near heater plane
NM-3	North-south	2.616	4	Near west face
WM-1	East-west	2.650	3	Near north face
WM-2	East-west	2.616	4	Near south face
TM-1	Vertical	5.413	4	Near center

during only the first five days. By Day 6, the east-west expansion 1 m below the top of the block matched the expansion at the heater plane level (0.7 mm), and the north-south expansion was only about 0.1 mm less. Much less expansion occurred near the base of the block, which is attached to the ground. Expansion rates near the heater plane and near the top of the block were as high as 0.2 mm/day during the first couple of days of heating, and gradually diminished to under 0.05 mm/day within three weeks (Figure 7-6). Expansion rates near the base peaked at around 0.05 mm/day in the first week and gradually diminished. By the end of the first two weeks, both the north-south and east-west displacements near the top of the block exceeded the north-south displacement at the heater plane level. The larger displacements near the top of the block were unexpected because the highest temperatures occur at the level of the heater plane.

Displacement histories during the first 100 days are shown for each extensometer in Figures 7-7 through 7-12. The displacements are measured relative to February 28, 1997, the day heating began, and the plotted values are daily averages for selected days. Each of the displacements is measured relative to the borehole collar, so that the anchor 4 displacements are cumulative, in that they are measured over the entire baseline. The displacement data show a rapid expansion of the block in all three measured directions during the first 30 or 40 days. The expansions continue throughout the 100-day interval but at a gradually diminishing rate.

The displacements for the lowest extensometer from the top, WM-1, are shown in Figure 7-7. MPBX WM-1 measures the east-west displacements of three anchors relative to a collar located on the west face near the north side of the block, about 1.25-m below the heater plane (See Table 7-1). The WM-1 displacements are relatively small; and east-west strains, calculated as the ratio of displacement to baseline length, are not uniform. The anchor 4 displacement at 100 days, of about 0.74 mm, represents a strain of 0.28×10^{-3} over the entire baseline of 2.65 m. However, the anchor 3 displacement is only about 0.4 mm at 100 days; this is distributed over a baseline of 2.09 m and represents a strain of about 0.20×10^{-3}. The relative displacement between anchors 3 and 4 at 100 days is about 0.34 mm over a baseline of 0.56 m, which yields a strain of about 0.60×10^{-3}. This strain, representing east-west deformation in the lower, northeast portion of the block, is about three times as large as the east-west strain along the rest of the WM-1 borehole and may indicate the opening of a fracture.

NM-1 is the other extensometer near the base of the block, and its record (Figure 7-8) also shows relatively small displacements at early times. NM-1 trends north-south about 1.1 m below the heater plane near the east face of the block. It is at about the same level as WM-1 and is orthogonal to it. The anchor 4 displacement of about 0.7 mm at 60 days was little changed 40 days later. Over the baseline of 2.616 m, the 0.7-mm displacement yields a strain of about 0.27×10^{-3}, nearly identical to the WM-1 anchor 4 strain. This suggests that the early deformation near the base of the block is essentially the same in the north-south and the east-west directions. An unexpected feature of the NM-1 record is the lack of relative displacement between two pairs of anchors. The anchor 1 and anchor 2 displacements are nearly identical, as are the anchor 3 and anchor 4 displacements. This suggests that no net strain occurred between anchors 1 and 2 or between anchors 3 and 4, and is an unexpected result, because temperatures were rising rapidly early in the heating phase of the test. Thermal expansion should cause the entire block to expand, so that positive net strains would be expected between each pair of anchors. The lack of relative displacement may indicate a problem with two or more of the NM-1 anchors, or closure of open fractures between the two pairs of anchors may have taken up the thermal expansion.

The large block contains many fractures and, because the overall displacements are so small, fracture closures of only about 0.1 mm would suffice to eliminate most of the relative anchor displacements.

MPBX NM-2 was located about 30 cm above the heater plane and experienced temperatures above 80°C a few days after heating began. The NM-2 displacement data are of low quality, and three of the four anchors ceased functioning entirely within the first 100 days (Figure 7-9). The anchor 4 data are probably the most reliable. They show a rapid expansion to about 1.3 mm within the first 40 days, more than twice that of the two lower extensometers (WM1 and NM1) at this time. Most of this displacement occurred in the first 10 days. The NM-2 anchor 4 displacement is about 0.8 mm at 10 days, compared to 0.25 mm for WM-1 or 0.3 mm for NM-1. The large and rapid expansion is in line with expectations because NM-2 is located close to the heater plane. Unfortunately, the anchor failed at Day 42.

MPBX WM-2 is located about 1.5 m above the heater plane near the south wall of the block, parallel and diagonally across from WM-1. The WM-2 data are of very good quality (Figure 7-10). The displacements increased rapidly during the first 40 days, then continued to rise at a much-reduced rate. The anchor displacements track each other well over time. The displacement data show expansion over each segment of the extensometer baseline. The displacements and strains are much larger than those recorded near the base of the block and, after six days, are even larger than those recorded by NM-2 near the heater plane. The WM-2 anchor 4 displacement at Day 100 is about 2.1 mm, which translates to a strain of about 0.80×10^{-3}, nearly three times as large as the WM-1 anchor 4 strain. At Day 40, the WM-2 anchor 4 displacement (1.9 mm) and strain (0.74×10^{-3}) are clearly larger than the NM-2 displacement (1.3 mm) and strain (0.47×10^{-3}). The WM-2 strains are relatively uniform, ranging from 0.7×10^{-3} to 0.8×10^{-3} over the entire baseline, except for anchor 1, which is much larger at 1.4×10^{-3}. The large anchor 1 strain may indicate the opening of a fracture in the upper, southwest corner of the large block in the early days of the test.

MPBX NM-3 is located about 1.8 m above the heater plane and about 0.9 m below the top of the large block. The borehole collar is on the north face near the west wall, diagonally across from NM-1. The quality of the NM-3 data (Figure 7-11) is generally good, although inferior to WM-2. The displacements measured over the longer baselines (anchors 3 and 4) are similar in magnitude to those measured by anchors 3 and 4 of WM-2, but the short baseline displacements are smaller. The anchor 2 displacements are even smaller than those for anchor 1, despite being made over a baseline about twice as long and, as such, are somewhat suspect. The other three anchors yield north-south strains ranging between 0.6×10^{-3} for anchor 1 and 0.9×10^{-3} for anchor 4. As the strain for WM-2 anchor 4 is about 0.8×10^{-3}, deformation near the top of the block during the first 100 days was essentially the same in the north-south and the east-west directions.

MPBX TM-1 is emplaced in a vertical borehole. The borehole collar is located near the center of the top face of the large block. MPBX TM-1 appears to have performed well for the first 80 days or so, but the anchors began to fail shortly thereafter, and only anchor 2 was functioning after Day 120 (Figure 7-12). The TM-1 record shows increasing displacements, until 80 days, as the rock heated up over time. Larger displacements were recorded for the longer baseline anchors. The anchor 4 strain at 100 days, which is measured over a 5.4 m baseline, is about 0.3×10^{-3}. This is considerably smaller than the horizontal strains measured near the top of the

block and slightly larger than the horizontal strains measured by NM-1 and WM-1 near the bottom.

The anchor 4 strains over the first 100 days are shown for all MPBXs in Figure 7-13. The contractions that occurred at Days 24 and 41, most evident in the data for upper MPBXs, are probably due to brief cooling episodes that resulted from temporary power outages. The strains fall into three categories: small strains for the vertical and two lower MPBXs, large strains for the two upper MPBXs, and intermediate strain for NM-2, located near the heater plane. The base of the large block is still attached to the ground, which accounts, at least in part, for the relatively small strains near the base.

7.1.1.2 Day 100 to Day 375

Displacement records are incomplete during this interval because several MPBXs experienced mechanical problems or failed completely. However, enough data were gathered that general trends can be discerned, at least for the upper two extensometers, WM-2 and NM-3, and for one of the lower extensometers, WM-1. Overall, the MPBX displacements follow the temperature trend through time, as can be seen by comparing anchor 4 displacements for these extensometers with temperature records for RTDs at similar depths (Figures 7-14 through 7-16). The RTD temperatures rose rapidly during the first 50 days, then more gradually until Day 220 into the test, apart from dips on Day 104 and Day 186. Displacements increased rapidly during the first 50 days and peaked at about Day 220, when the heater power was reduced. The upper RTD (TT2-22) temperature then declined by about 10 degrees and remained relatively constant, except for a dip at Day 340, until cool-down began at Day 375. Temperatures fell rapidly during cool-down. The data for the upper extensometers follow a similar pattern: displacements drop slightly after Day 220, then remain nearly level until Day 375, and drop sharply afterward. The lower RTD (TT1-8) temperature appears to have fallen more or less continually during the Day 220 to Day 375 interval, and the lower MPBX (WM-1) also shows more or less continual contraction during this time, followed by a steep drop on cool-down.

The drop in temperature that began at Day 104 was probably related to reflux of steam/water along the TT1 RTD column (Section 5.4.3). Temperatures near the intersection of borehole TT1 and the heater plane dropped rapidly to the boiling point (Figure 7-17). The temperature response indicates that water came in contact with dry rock near the heater plane at this time. This water would have traveled along a fracture, because the matrix permeability of the tuff is too low to account for the sudden drop in temperature at the heater plane. The upper, east-west extensometer, WM-2, may have captured a transient signal related to the passage of fluids in a fracture at this time. A small double pulse can be seen at Day 105 in the WM-2 displacement records in Figure 7-17. The double pulse is present at Day 105 in the signals from all four anchors, which indicates that the displacement transient originated between the borehole collar on the west wall and the first anchor 0.83 m to the east. The borehole collar moved outward, away from the anchors. An enlarged image of the WM2 double pulse signal is shown in Figure 7-18, along with temperature data from nearly the same depth (1.2 m) as the WM-2 borehole. The displacement transient occurred at about the same time as a brief drop in temperature at 1.2-m depth in borehole TT1. It seems unlikely that the small drop in temperature at this depth, or the large drop at the depth of the heater plane, explains the displacement transient, because the sense of the displacement (expansion initially) is opposite to that expected for the temperature

change. The magnitude of the double pulse displacement is quite small, under 0.05 mm, and it may represent a temporary opening or shear motion along a fracture, either of which would increase permeability. Presumably, this fracture intersected the surface of the large block near the upper southwest corner. The WM-2 borehole would then pass through it within 0.83 m of the west wall and would also likely intersect borehole TT1, so that water traveling downward through the fracture would come into contact with several of the TT1 RTDs.

The drop in temperature at Day 220 was due to a reduction in the heater power. A rainstorm triggered the temperature drop at Day 186. The drop in temperature at Day 186 is correlated with extensometer displacements in the upper portion of the large block (Figure 7-19). The correlation is especially good for extensometer NM-3, which passes closer to borehole TT1.

7.1.1.3 Cool-down

Repairs were made to the TM-1 and NM-1 extensometers shortly before the beginning of the cool-down phase. As a result, good displacement records exist over the cool-down for each of the MPBX systems, except NM-2, which wasn't repaired. The cool-down displacements show that the block contracted rapidly in all directions after the heaters were turned off. Records for individual extensometers, except NM-2, are given in Figures 7-20 through 7-24. Anchor 4 strains are shown in Figure 7-25 for comparison. The two upper MPBXs contracted more than the two lower MPBXs, as expected, since they lengthened considerably more during the heating phase. Contraction along the vertical extensometer was comparable to that of the upper horizontal extensometers, but the vertical extensometer has a longer baseline. The displacement during cool-down for the two lower extensometers was under 1 mm.

The upper MPBXs did not contract as much during cool-down as they lengthened in the heating phase. NM-3 contracted about 1.5 mm, and WM-2 contracted about 1.8 mm, whereas both had expanded about 2.4 mm during the heating phase, so that there has been a net displacement of a few tenths of a millimeter in the upper portion of the block. In contrast, one of the lower MPBXs, WM-1, returned almost exactly to its starting length. It is not possible to determine if positive or negative net displacements occurred for the lower MPBX (NM-1) or the vertical MPBX (TM-1) because these extensometers were repaired during the test, and they were zeroed to the current position instead of the prerepair conditions. However, by comparing the anchor 4 strains during the first 100 days (Figure 7-13) to those during cool-down (Figure 7-25), it can be seen that NM-1 contracted at least as much or more during cool-down (0.3×10^{-3}) as it lengthened (0.25×10^{-3}) during the early portion of the heating phase. The vertical extensometer (TM-1) contracted slightly less, recording an extension of 0.33×10^{-3} for anchor 4 during the first 100 days and a contraction of 0.22×10^{-3} during cool-down. In summary, the horizontal strains near the base of the block were small, essentially the same in the two horizontal directions, and were recovered during cool-down. The horizontal strains near the top of the block were large, isotropic, and were only partially recovered. The vertical strain was fairly small but only partially recovered during cool-down.

7.1.2 Large Block Thermal Expansion

7.1.2.1 Introduction

Rock thermal expansion coefficients are typically measured on laboratory specimens, which, because of their small size, usually exclude fractures and other heterogeneities that exist in situ. Brodsky et al. (1997) made a large number of such measurements on Topopah Spring tuff. Although laboratory-derived thermal expansion coefficients may accurately characterize the thermal expansivity of the rock matrix, they may not be representative of the rock mass. Fractures may close as a rock mass is heated and thereby lower bulk thermal expansion, so that laboratory-derived thermal expansion coefficients likely form an upper bound for in-situ thermal expansivity. Tighter constraints on in-situ thermal expansivity may be supplied by field measurements, but to date these are relatively rare. A few thermal expansion coefficients have been obtained from the Single Heater Test and are available in CRWMS M&O (1999). Temperature and MPBX displacement data from the LBT provide a much-needed opportunity to estimate thermal expansion coefficients for a fractured block of Topopah Spring tuff.

7.1.2.2 Data Reduction

Twelve dates, mostly within the first 83 days of heating, were chosen for thermal expansion calculations. The initial temperature was taken to be 11.6°C, based on the average of a large number of temperature measurements made prior to heating. Because temperatures were not measured in the MPBX boreholes, they had to be interpolated from temperatures measured at known RTD locations. Because the block was heated along a horizontal plane and insulated on its sides, the thermal gradients were primarily vertical, and the horizontal thermal gradients were small. Peak temperatures coincide with the heater plane, then fall off asymmetrically above and below, with the top surface temperature at 60°C. The vertical thermal gradients were generally steeper in the lower portion of the block because the upper surface temperature was maintained at or near 60°C for much of the test. Because the vertical thermal gradients are relatively large, no attempt was made to calculate thermal expansion coefficients in the vertical direction.

Invar steel rod extensions were calculated from the interpolated temperatures and the linear thermal expansion coefficients for invar steel, given in SNL (1997). The invar rod extensions, δ, are found as

$$\delta = \alpha(T)\Delta TL \qquad \text{(Eq. 7-1)}$$

where

$\alpha(T)$ is the invar thermal expansion coefficient,
ΔT is the temperature change, and
L is the length of the invar rod.

Extension is positive. The total displacements for each anchor were corrected for the rod thermal extension. Because the invar rods expand during heating, the anchor displacements measured at the borehole collars are smaller than the actual rock mass displacements by the rod extensions. The anchor displacements were divided by distance to give strains. These distances vary from

about 0.75 m for anchor 1 to about 2.6 m for anchor 4. The thermal expansion coefficients for anchor 4 tend to be more consistent because of the longer baseline.

Thermal expansion coefficients were found by regressing cumulative strains, measured from anchor 4 to the borehole collar, against the average temperature change for each extensometer (Table 7-3). The temperature changes were calculated as the weighted-average of the interpolated temperature changes at each anchor location, using the anchor spacings as the weights. Temperature changes were fairly uniform along the horizontal extensometers, and the weighted-average technique was intended to lessen still further the effect of horizontal thermal gradients on the calculated thermal expansion coefficients. However, no corrections were applied for the effects of the vertical thermal gradients or for the fact that the base of the block is still attached to the outcrop.

Table 7-3. Interpolated Average Temperatures for Horizontal MPBX Extensometers

	Interpolated temperatures (°C)				
Date	NM1-4	NM2-4	NM3-4	WM1-4	WM2-4
3/7/97	10.7	31.5	7.6	12.4	10.4
3/19/97	27.5	53.4	29.2	30.0	31.1
3/31/97	33.0	63.7	40.7	36.6	43.9
4/12/97	35.4	69.3	44.4	38.9	48.4
4/21/97	39.4	71.9	47.4	42.4	51.6
5/3/97	41.7	75.4	49.3	45.1	54.4
5/18/97	47.3	79.6	53.2	49.2	58.2
8/21/97	69.3	98.7	66.6	69.3	74.9
9/24/97	68.7	105.1	65.9	71.8	76.1
11/19/97	61.0	100.1	63.0	65.2	70.0
2/18/98	56.2	98.8	55.4	58.1	65.4
3/18/98	44.4	62.1	48.8	44.2	55.7

7.1.2.3 Results

Cumulative horizontal strains recorded by the MPBX extensometers during the early heating phase for the LBT are shown in Figure 7-26. The strains are plotted for the same dates used to estimate thermal expansion coefficients. The strains are quite isotropic—i.e., the north-south and east-west strains are nearly identical but vary by depth. Much larger horizontal displacements, and hence strains, were recorded near the top of the block than near the base, particularly during the first month of heating. The horizontal strains near the top of the block exceeded those recorded by extensometer NM-2 near the heating plane, even though the thermal pulse had not yet penetrated very far above or below the heater plane. The implication is that fractures in the relatively cool rock well above the heater plane were displaced more than in the hotter rock near the heater plane in the early portion of the test (See Section 7.2.2).

Anchor 4 strains are plotted against temperature changes in Figure 7-27, and lines are fit to the data using ordinary least squares. The anchor 4 strains were used to provide the longest possible baseline. The slopes of the fitted lines provide estimates of rock mass thermal expansion

coefficients. The estimated slopes, correlation coefficients, and standard errors of the regression fits are given in Table 7-4.

Table 7-4. Thermal Expansion Coefficients (CTE) and Fitting Statistics

MPBX	NM1-4	NM2-4	NM3-4	WM1-4	WM2-4
Slope (CTE)	6.586E-06	7.214E-06	1.420E-05	7.135E-06	1.085E-05
Correlation	0.999	0.996	0.989	0.998	0.990
Std. error	8.466E-08	6.669E-07	7.479E-07	1.391E-07	5.338E-07

The measured MPBX displacements, and hence the calculated thermal expansion coefficients, were found to increase from the base to the top of the large block. The coefficient values approximately double, from about 7×10^{-6} °C^{-1} in the bottom third of the block to about 15×10^{-6} °C^{-1} in the top third (Figure 7-28). The calculated thermal expansion coefficients in the two horizontal directions are fairly close, similar to the measured displacements.

7.1.2.4 Discussion

The overall horizontal deformation of the block revealed similar amounts of expansion in both the east-west and north-south directions. The expansion was essentially a positive, linear function of height above the base of the large block, independent of the temperature gradient above the heater plane. The latter result was unexpected because the hottest portion of the block is near the center. The MPBX extensometer data from the upper one-third of the block suggest that most of the deformation occurred in discrete, vertical zones, perhaps due to opening of vertical fractures in this region. Fracture gauge data indicate that several fractures opened more than 0.1 mm on the block surface during the test (Section 7.1.3). The fracture opening displacements were likely driven at least in part by block movement. Horizontal displacements in the lower portion of the block were restrained because the base of the block is attached to the ground, but the upper portion of the block was largely unconfined.

The thermal expansion coefficients calculated from the LBT extensometer data are somewhat higher than those for the Single Heater Test (CRWMS M&O 1999a). Despite the vast difference in scale, the thermal expansion coefficients obtained for the lower half of the large block are similar to those measured for 19 saturated TSw2 laboratory specimens by Brodsky et al. (1997). Over the 25° to 150°C temperature range, they found mean thermal expansion coefficients between 7.14×10^{-6} °C^{-1} and 9.98×10^{-6} °C^{-1}. Thermal expansion coefficients of about 7×10^{-6} °C^{-1} were calculated for the middle-to-lower portions of the large block for the first 83 days of heating (Table 7-4). The higher thermal expansion values obtained here for the upper portion of the large block are suspect, because a portion of the horizontal deformation recorded by the upper two MPBX extensometers may have been caused by opening of vertical fractures in the upper third of the block.

7.1.3 Fracture Monitors

Deformations of several major fractures that intersect the surface of the LBT block were monitored using three-component fracture monitors. The purpose of these gauges was to monitor the movement of fractures to gain information on the magnitude and direction of fracture

deformation during the test, especially as it relates to TH behavior. A fracture monitor gauge is shown schematically in Figure 7-29. This gauge consists of two steel fixtures that are mounted on either side of a fracture. One of the fixtures serves as the mounting block for three linear variable displacement transducers (LVDTs) that are mounted orthogonal to each other. The other fixture serves as the reference block. The gauges were mounted in T-shaped slots cut into the block. The slots were cut so that one LVDT would measure aperture change or deformation across the fracture in the plane of the face, while the other two LVDTs would measure sliding in orthogonal directions, parallel and perpendicular to the face. These are approximate measures of in-plane and normal deformations for the fractures. The fractures chosen were oriented perpendicular to the face as much as possible; thus the information can be used to supply estimates of fracture deformation parameters, such as dilation with sliding. Fracture monitor (FM) locations are shown for each face in Figures 7-30 through 7-33, and a few of the fracture locations are visible as T-shaped grooves in Figure 7-34. One of the installed gauges is shown in Figure 7-35.

The fracture monitors were installed on the four vertical faces of the block as follows:

- On the east face (see Figure 7-30), three FM gauges (EF2, EF3, and EF4) were mounted along a prominent vertical fracture located near the center of the face. One FM (EF1) was used to monitor deformation on the large horizontal fracture near the top of the block.

- FM locations on the north face are shown in Figure 7-31. FMs on this side were used to detect motion on the major subhorizontal fracture near the top of the block (NF-5) and in a subvertical fracture zone that was exposed in the center of the north face (NF2, NF3, and NF4).

- On the west face, FMs were used to monitor the subhorizontal fracture near the top (WF5), a subvertical fracture on the northwest side (WF1, WF2, and WF4), and a subhorizontal fracture near the bottom (WF3) on the northwest side (see Figure 7-32). Data for several fractures on the west face were not collected during the first 20 days of the test because of an instrumentation problem. Data were set to zero at Day 20 for these transducers.

- On the south face of the block, three fractures were monitored (see Figure 7-33). Fracture monitors SF-1 and SF-2 monitored one subvertical fracture, while SF-3 monitored a subhorizontal fracture on the lower southwest part of the block, and SF-4 monitored a subhorizontal fracture near the top.

7.1.3.1 Deformation on Vertical Fractures

The fracture aperture data recorded for vertically oriented fractures are plotted in Figure 7-36, along with temperatures measured at RTD TT1-14. This figure shows that a fracture opening of between 0.1 and 0.36 mm occurred at several locations, and that fracture closing between 0.002 and 0.16 mm occurred on several others. Moreover, for fractures that show opening, a substantial portion of the opening occurs within the first 40 days of heating. Opening and closing are observed on all faces of the large block. The maximum apertures for four of the opening

fractures occur near Day 300 at the end of the test. Most of these opening fractures show closing and reopening behavior associated with cool-down. However, one fracture, NF2, opens approximately 0.15 mm upon cool-down.

Approximately half of the fracture monitors also show fracture closing behavior during the heating period. As expected, the magnitude of closing is smaller and the nature of the closing signals is also different from opening fractures. Generally, closing behavior is smoother and less responsive to temperature. The fractures that close reach maximum closure sometime between Day 100 and 400. The closing fractures show little change during cooling.

Figure 7-36 also shows that decreasing aperture was recorded by many of the fracture monitors on vertical fractures on about Day 125. Data for Days 100 to 140 are shown in more detail in Figure 7-37, along with temperatures recorded at TT1-14. This figure shows that the closing of vertical fractures between Day 125 and 130 occurred at several locations. This deformation can be associated with thermal recovery subsequent to the TH event that started on Day 105.

Slip on vertical fractures is shown in Figure 7-38, along with temperatures at TT1-14. This figure shows that slip on vertical fractures ranged from 0.07 to 0.58 mm. For the FMs with the largest slip (NF-2, EF-3), slip followed the temperature quite closely, increasing rapidly upon initial heating and decreasing upon cooling. These two fracture monitors, along with EF2, also show opposite responses to the TH episode on Day 105. Slip increased on NF2 but decreased on EF3. This is associated with thermal recovery from the TH event. Fracture slip generally did not increase during the constant temperature portion of the test, except on EF4, where slip was observed at a steady rate until cool-down. Generally, slip is not recovered; however, the gauges with the most slip show some recovery.

Further analysis of the slip components shows that the largest slip deformations EF3, NF2, and EF-2 are associated with movement normal to the block face at each of these FM locations. For FMs showing total slip less than 2.5 mm, both components perpendicular and parallel to the block face contributed.

It is important to note that this analysis computes slip as a vector sum of distance recorded in two perpendicular directions, and the computed slip is not cumulative. Thus, this analysis provides a minimum estimate of the amount of slip.

The maximum and residual aperture and slip data have been tabulated for the fractures and are presented in Table 7-5. Figure 7-39 shows values of maximum and residual aperture for just the vertical fractures, listed according to distance below the top of the block. This figure shows that the largest fracture aperture changes were due to opening in the lower portion of the block. Fracture aperture in the upper portion of the block (within 1.85 m of the top) generally remained constant or showed closure. This figure also shows that at most of the FM locations the residual values of fracture aperture are only slightly smaller than the maximum value, indicating that the fracture deformation did not recover upon cool-down.

Figure 7-40 presents a histogram of the maximum and residual values of slip on vertical fractures. This figure is consistent with Figure 7-39 in that the maximum values of slip occurred in the lower part of the block. The minimum slip displacements are at 1.2 m from the top, with

Table 7-5. Maximum and Residual Fracture Slip and Aperture

Face	Fracture monitor	Fracture orientation	Depth (m)	Slip (max) (mm)	Slip (res) (mm)	Aperture (max) (mm)	Aperture (res) (mm)
E	EF1	H	-0.68	0.320	0.245	0.226	-0.045
E	EF2	V	-2.63	0.295	0.223	0.210	0.190
E	EF3	V	-3.37	0.575	0.260	0.350	0.275
E	EF4	V	-0.84	0.245	0.210	0.016	0.010
N	NF2	V	-2.70	0.570	0.230	0.360	0.310
N	NF3	V	-3.93	0.128	0.089	-0.050	-0.028
N	NF4	V	-0.87	0.143	0.117	-0.158	-0.146
N	NF5	H	-0.58	0.280	0.225	0.090	0.040
S	SF1	V	-1.18	0.122	0.120	-0.036	0.010
S	SF2	V	-1.92	0.184	0.140	0.170	0.150
S	SF3	H	-3.98	0.160	0.135	-0.063	0.000
S	SF4	H	-0.64	0.195	0.148	0.252	0.062
W	WF1	V	-1.85	0.109	0.109	-0.090	-0.072
W	WF2	V	-2.65	0.110	0.090	0.350	0.275
W	WF3	H	-3.95	0.050	0.030	0.050	0.050
W	WF4	V	-1.21	0.073	0.073	0.055	-0.040
W	WF5	H	-0.31	0.675	-0.020	0.350	-0.050

slip generally increasing above and below this level. Exceptions are FMs WF2 and NF3 located 2.65 and 3.93 m below the top of the block. Both are in fracture zones. Also note that except for the largest slip, most of the slip is not recovered, and at least 0.2 mm of slip is not recovered at four locations.

The larger aperture values at the bottom of the block are associated with larger slip values, and this may provide information on fracture properties, as discussed later in this section. However, the trend of increased opening with distance below the top is inconsistent with the MPBX data.

7.1.3.2 Deformation of Horizontal Fractures

Fracture monitors were also deployed on three subhorizontal fractures in the block. The most prominent of these was the large subhorizontal fracture near the top of the block that intersected all four faces. Smaller subhorizontal fractures were also instrumented on the west and south sides of the block (see Figures 7-32 and 7-33).

The fracture aperture deformations for these horizontal fractures are plotted along with temperature at TT1-14 as a function of time in Figure 7-41. Overall, aperture changes are less than or equal to 0.3 mm and are similar to those on vertical fractures.

Fracture monitors WF5, SF4, EF1, and NF5 monitor the large subhorizontal fracture near the top of the block. Figure 7-41 shows that opening was observed for these four FMs. The response of SF4 during the first 40 days was similar to that shown for vertical fractures in that the initial deformation followed temperature near the heater. Fracture monitors EF1 and NF-5 do not show significant movement until after 30–40 days of heating. Data for fracture monitor WF-5 were not recorded during the initial 20 days of heating. However, after Day 20 WF-5 followed the temperature at TT1-14 until Day 220, after which the fracture continued to open while

temperature remained constant. The most striking feature is that NF-5, EF-1, and WF-5 all show substantial spikes at the onset of the TH event at Day 105.

The association of fracture deformation with TH behavior is shown more clearly in Figure 7-42. This figure shows the aperture deformation of the large subhorizontal fracture, along with temperature of TT1-14 for 100–140 days. The figure shows that opening of the fracture at EF1 and NF5 preceded the thermal event by almost one day and that the fracture opened 0.1 mm at EF1 and 0.07 at NFS over a 2–3 day period and then closed back to original levels. Closing of fractures during initial thermal recovery is similar to behavior for the vertical fractures at this time.

Figure 7-41 shows that fracture monitors NF-5 and EF-1 also show similar behavior at Day 180 and at Day 340. The behavior is a spike associated with temperature drop followed by a closure. The spike at Day 180 can be associated with the TH event recorded by TT1-14. The aperture spikes at Day 340 are associated with at similar TH event recorded at RTD TT2-22, which is approximately 1.6 m above the heater plane.

Fracture monitors WF3 and NF3 recorded deformation of fractures lower in the block, and show overall fracture closing. These fractures show increased aperture closing during the thermal recovery at Day 125 (see Figure 7-42).

Finally spikes in aperture are associated with cool-down. In addition, fracture monitor data indicate that rock above the subhorizontal fracture near the top behaves as a unit; this may be because the heat exchanger and other hardware on top of the block serve as rigid connectors for rock blocks forming the top of the block.

Slip on horizontal fractures is shown in Figure 7-43 along with temperature for RTD TT1-14. This figure shows that slip on horizontal fractures lags the temperature at the heater plane. The values of slip are in the same range as for the vertical fractures, and for fracture #LBT-1 (see Table 4-2) slip increases sharply up to Days 50–60 and then levels off, except for WF5, for which slip continues to increase until very late in the test. Figure 7-44 shows slip measurements for horizontal fractures for Day 100 to Day 140. Fracture monitors WF5, EF1, and NF5 show slip events at Days 104-105, but the slip events are not as dramatic as the changes in aperture. WF5 shows slip recovery between Day 125 and Day 130 that is opposite the behavior shown by vertical fractures. SF4 and EF1 show increased slip during this period, more like vertical fractures. Spikes in data are also found at Day 180 and Day 340 (EF1, WF5, and NF5). WF5 reacts to cooling on Day 220 but thereafter slip continues to increase. WF5 recovers on cool-down, while SF3 shows more than 1 mm of slip increase on cool-down.

Maximum and residual deformation across horizontal fractures have been tabulated (see Table 7-5) and is plotted in Figure 7-45. This figure shows that for three of the four vertical large-block faces, the large horizontal fracture near the top opened more than 0.2 mm, but residual opening was much smaller. This is in contrast to the behavior of the vertical fractures. (Figure 7-39), which show small opening or even closing motions. It is important to note that all vertical measurements were made below this fracture.

Figure 7-45 also shows that the aperture deformation of the two lower horizontal fractures was very different from that of Fracture LBT-1. Figure 7-46 presents maximum and residual slip

along all monitored horizontal fractures. This figure shows that slip on one fracture (WF5) was very large (0.7mm) but was totally recovered upon cool-down. Slip of 0.2 to 0.3mm was recorded on the other three sides, and most of this slip was irreversible. The least amounts of slip erew recorded on the lowest fractures in the block. This, again, is in contrast to the vertical fracture data, which show more fracture slip lower in the block.

7.1.3.3 Summary of Fracture Monitor Results

The FM data show that the vertical and horizontal fractures responded somewhat differently. Fracture #LBT-1 opened coincidentally with the TH event at Day 105. Both vertical and horizontal fractures show closing during the thermal recovery from the TH events, that is, during periods of apparent refluxing.

Initial response for several of the FMs was associated with temperature at the heater plane. Overall FM deformations are consistent throughout the block, as indicated in Figure 7-47, which shows general block movements. FM data indicate that the top of the block moved to the east. Most of the FM deformation was not recoverable. The FM data are somewhat inconsistent with the MPBX data, as FMs indicate more deformation in lower portions of the block and less deformation the upper portions of the block.

7.1.4 Discussion and Summary

Analysis of the large block deformation has been conducted using data from six MPBX systems and approximately 20 fracture monitors. Results from both the MPBX systems (Figure 7-48) and the FMs (Figure 7-49) show that within a few hours of heater startup the block started expanding.

The MPBX data (Figure 7-48) show that most of the expansion has occurred in the upper third of the block and in the horizontal plane. In this region, horizontal strain of 0.0006 was observed through March 18, 1998. This is somewhat greater than the value of 0.0001 that is predicted in a TM simulation of the test (Blair, Berge, et al. 1996). Moreover, MPBX data from boreholes in this region show that most of the deformation occurred in discrete, vertical zones, which may be caused by the opening of vertical fractures in the upper portion of the block.

The central third of the block, although hotter than the upper third, shows less horizontal expansion. However, the observed strain of 0.0004 is in good agreement with the value of 0.0006 predicted for this zone after this period of heating. Finally, deformation in the lower third of the block was small, with total horizontal strain estimated as 0.0002. This is consistent with the predicted thermal expansion. Data for one of the horizontal holes also indicate that deformation occurred in a discrete, vertically oriented zone. The data also indicate that vertical strains are smaller than horizontal strains, and that the portion of the block above the heaters is moving upward as a unit.

In summary, thermal expansion of the block was evident a few hours after the start of heating, as verified by the fracture monitors and MPBX systems. The MPBX data indicate that, during the first month of heating, the upper third of the block expanded horizontally more than predicted on the basis of continuum assumptions, and much of the deformation took place in discrete zones, consistent with the opening of vertical fractures. In the middle and lower thirds of the block,

expansions were more consistent with predicted values. In the vertical direction, the upper two-thirds of the block (i.e., the portion above the heater horizon) extended as a unit.

7.2 SIMULATIONS

Three-dimensional distinct element analysis was performed to simulate MPBX deformations. The simulations will be discussed in chronological order. This work is documented in Blair, Berge, et al. (1996).

7.2.1 Distinct Element Analysis

A distinct element code (3DEC) (Itasca 1998) was used in this analysis to simulate TM behavior in a 3-D region of fractured rock forming the LBT. The distinct element method was chosen because it allows discrete fractures to be incorporated into the simulation. This is important because fracture movements can cause large local deformation and changes in permeability. Moreover, continuum approaches do not provide direct estimates for fracture deformation. The distinct element method also provides for calculation of joint behavior (normal and shear deformation) at specific points along a joint surface. Thus, this method can (a) handle redistribution of stress after shear slip occurs along a fracture, (b) provide insight into the primary mechanisms of fracture deformation over time, and (c) preserve the time history of fracture deformation. The 3DEC code can accommodate several constitutive material relations for blocks, and both Coulomb slip and continuous slip models for joints. The code can also be used to simulate an unfractured rock mass.

3DEC also has the capability to accept temperatures from external sources. This can be done by initializing the code for thermal analysis and then substituting temperatures from the external source into the 3DEC temperature array at each time step. Using this technique, the temperatures predicted using a robust TH code, such as NUFT, or a temperature field developed from field observations (e.g., the LBT) can be used to predict THM behavior.

7.2.1.1 Model Development

The spatial domain for the model is shown in Figure 7-50. This region has the same dimensions in cross section as the 2-D FLAC model discussed previously in Section 3.5.3. That is, the subsurface model domain extends 23 m beneath the large block and 23 m out from each vertical face beneath the surface.

7.2.1.2 Boundary Conditions

Roller boundary conditions were imposed on the four vertical sides and on the base of the subsurface region. These boundary conditions impose a zero displacement restriction on normal displacements along these surfaces but allow parallel (in plane) displacements. Thus, horizontal displacements are permitted along the base of the block, and vertical displacements are permitted along the sides. Fixed displacement boundary conditions provide an upper bound on thermal stresses because outward displacements of the model sides, which would relieve built-up stresses, are not allowed.

The base of the block was fixed in the vertical direction to prevent the rock at 23 m below the LBT from moving vertically. The top of the block is allowed to move vertically. This is appropriate because the LBT column is unconfined, whereas the base of the model is supported by the underlying rock. A fixed stress boundary condition, equal to atmospheric pressure, is applied to the top and sides of the LBT columnar region and to the ground surface region in the model.

7.2.1.3 Temperature Field and Calculation Times

Deformation of the LBT was calculated at times of 0, 10, 25, 55, 85, 115, 145, 182, 200, 275, 340, 350, 375, 385, 395, 410, 430, and 450 days after the start of heating. The temperatures in this analysis were derived from the TH analysis reported in Section 5.6. Files containing x,y,z locations and temperatures for the model region simulated by NUFT were obtained at each time. The NUFT model assumes symmetry in the block; consequently, these files contained values for one quadrant of the region simulated in 3DEC. The 3DEC calculation includes the entire volume of the block, because the fractures are not symmetric. A 3-D temperature field for 3DEC was produced from the NUFT temperatures by reflecting the temperatures about the appropriate vertical planes. This was done as follows. Temperatures from the NUFT model and their coordinates were input into EarthVision, v.5.1 along with an array of grid points generated by 3DEC for the LBT model domain at each calculation time. EarthVision performed a 3-D interpolation of the 3-D NUFT model temperatures to provide an interpolated temperature for each calculation time at each of the 3DEC model grid points. The grid point temperatures were then input into 3DEC as a separate input file for each calculation time.

7.2.1.4 Material Properties

Input parameters for the LBT simulation are provided in Table 7-6. Calculated or assumed parameters are listed in Table 7-7. The input bulk and shear moduli were calculated with the equations given below using values of rock mass elasticity modulus (24.71 GPa) and Poisson's ratio (0.21) taken from CRWMS M&O (1999b, Tables 10 and 11). The input values for joint normal stiffness and joint shear stiffness assume a joint spacing of 1 m and were calculated with a relationship given in the 3DEC User's Guide (Itasca 1998, Section 3, p. 94). The joint normal stiffness calculation used an intact rock elastic modulus of 33.03 GPa (CRWMS M&O 1999b, Table 8) and a rock mass elastic modulus of 24.71 GPa (CRWMS M&O 1999b, Table 10). Shear moduli for the joint shear stiffness calculation were obtained from the above elastic moduli and a Poisson's ratio of 0.21 (CRWMS M&O 1999b, Table 11). The other input parameter values were taken directly from the YMP Technical Data Management System. The input parameters are considered appropriate because they are derived from field and laboratory measurements of the host rock physical properties.

Table 7-6. Input Parameters and Data Tracking Numbers

Item No.	Description	Value	Units	Data Tracking Number
	Matrix properties			
1	Dry bulk density	2270	kg/m^3	MO0003SEPDRDDA.000
2	Intact rock elasticity modulus	33.03	GPa	MO9911SEPGRP34.000
3	Rock mass elasticity modulus	24.71	GPa	MO9911SEPGRP34.000
4	Poisson's ratio	0.21	none	MO9911SEPGRP34.000
	Joint properties			
5	Joint friction	41	degree	MO0003SEPDRDDA.000
6	Joint cohesion	0.09	MPa	MO9911SEPGRP34.000
7	Joint dilation angle	29	deg	MO9911SEPGRP34.000
8	Initial joint aperture	0.098	mm	LB990501233129.001
	Thermal properties			
9	Thermal conductivity	2.33	W/m-K	MO9911SEPGRP34.000
10	High thermal expansion coefficient	9.73E-6	deg C^{-1}	MO0004RIB00035.001
11	Low thermal expansion coefficient	5.27E-6	deg C^{-1}	SHT Final Report DTN
	Stress and stress gradient			
12	In-situ stress	0.1	MPa	MO0007RIB00077.000
13	Vertical stress gradient	0.023	MPa/m	MO0007RIB00077.000
	Input temperatures			
14	Input temperatures	various	deg C	LL000114004242.090

Table 7-7. Calculated or Assumed Model Parameters

Description	Value	Units
Matrix properties		
Rock mass bulk modulus	14.2	GPa
Rock mass shear modulus	10.2	GPa
Joint properties		
Joint tensile strength	0	MPa
Joint normal stiffness	98.1	MPa/mm
Joint shear stiffness	40.5	MPa/mm

In addition, the following assumptions were made for the LBT simulations:

- First, nominal dimensions and approximations were used in developing the geometric model and used throughout the modeling instead of exact design or as-built dimensions. This is because the limited sensitivity of the numerical simulations to slight dimensional variations in no way merits the use of exact dimensions.

- The initial model displacement prior to heating was assumed to be zero, and the initial stresses throughout the model were assumed to be in equilibrium with the applied boundary stresses and the gravitational gradient.

- Stress and temperature dependence of rock mass material properties was neglected in assessing deformation. Except for temperature dependence of the thermal expansion

coefficient, stress- and temperature-related changes to rock mass material properties are expected to have little impact on deformation in comparison to fracture displacements.

- Intact rock deformation is elastic and isotropic, such that bulk modulus, K, and shear modulus, G, can be calculated from the elastic modulus, E, and Poisson's ratio, ν, as:

$$K = E/\{3[1-(2\nu)]\} \quad \text{(Eq. 7-2)}$$

$$G = E/[2(1+\nu)] \quad \text{(Eq. 7-3)}$$

These relations are derived for linearly elastic, isotropic rock. Laboratory tests on intact rock samples from the repository horizon show them to behave as an elastic, isotropic material (Nimick et al. 1987, p. 32). The above equations of elasticity are from Jaeger and Cook (1979, p. 111). Moduli for blocks of rock forming the fractured rock mass may be lower and may generate lower stress levels than predicted.

Approximate normal and shear joint stiffness were calculated from information on joint spacing and elastic moduli for the fractured rock mass and intact portions of the rock. According to Itasca (1998, Section 3, p. 94), "If the jointed rock mass is assumed to have the same deformational response as an equivalent elastic continuum, then relations can be derived between jointed rock properties and equivalent continuum properties. For uniaxial loading of rock containing a single set of uniformly spaced joints oriented normal to the direction of loading, the following relation applies:

$$1/E_m = 1/E_r + 1/k_n s \quad \text{(Eq. 7-4)}$$

or

$$k_n = E_m E_r / s(E_r - E_m) \quad \text{(Eq. 7-5)}$$

where E_m = rock mass elastic modulus, E_r = intact elastic modulus, k_n = joint normal stiffness, and s = joint spacing. A similar expression is used for joint shear stiffness:

$$k_s = G_m G_r / s(G_r - G_m) \quad \text{(Eq. 7-6)}$$

where G_m = rock mass shear modulus, G_r = intact rock shear modulus, and k_s= joint shear stiffness."

And "Joint shear deformation followed a Coulomb slip model. This model provides a linear representation of joint stiffness and yield limit and is based upon elastic stiffness; frictional, cohesive and tensile strength properties and dilation characteristics common to rock joints. The model simulates displacement-weakening of the joint by loss of cohesive and tensile strength at the onset of shear or tensile failure" (Itasca 1998, p. 73).

Fractures used in the simulations were taken from the LBT fracture data set described in Section 4. Particular fractures used in the simulations are discussed below. The fractures were assumed to have no tensile strength. Fractures are very weak in tension, and any reasonable value for fracture tensile strength will be close to zero, which is the default value for the 3DEC program. Chen (1999, Table 3) used a fracture tensile strength of 0.04 MPa in an UDEC analysis of drift stability at Yucca Mountain. This value was intended as a reasonable average value for fracture tensile strength (Chen 1999, p. 761). The minimum fracture tensile strength is assumed here to enhance changes in fracture aperture and permeability.

7.2.1.5 Simulations

A series of simulations was conducted to evaluate the effects of the number of fractures and the Coefficient of Thermal Expansion (CTE). The simulations are listed in Table 7-8, and the geometry of the model domain for the various simulations is shown in Figure 7-50.

Table 7-8. Summary of LBT TM Simulations

Model #	No. of Fractures	CTE ($x10^{-6}$/°C)	Comment
1	0	5.27	Continuum model
2	6	9.73	High CTE with six major fractures
3	6	5.27	Low CTE with six major fractures
4	7	5.27	Same as 3 with one additional fracture
5	28	5.27	All fractures included in fracture analysis

7.2.1.6 Results

The 3DEC model was configured to produce displacement values at the locations of the MPBX anchors discussed in Section 7.1.1. Comparisons were made for most of the MPBX holes for the first 100 days of heating, as this is the period when MPBX results were most reliable. Comparisons were also made for the cool-down phase, for which new transducers were installed into some of the MPBX units. Data for the entire test are used for WM2 and NM3. Simulated deformation in the vertical direction is compared with observed displacement for anchor 4 in TM1 (TM1-4), as shown in Figure 7-51 for the first 100 days of heating. This figure plots results for each simulation along with the observed displacement and shows that while Model 2 (Table 7-8) with high CTE matches the early thermal deformation up to Day 20, it overpredicts the deformation at 100 days by more than a factor of 2. Predictions produced by the other four models, with a lower CTE, are quite acceptable. The continuum and fractured models produce similar estimates, and the response of all of these models lags the observed deformation during the first 40 days. Thus, the number of fractures had very little effect on predicted deformation in the vertical direction.

Predicted deformation during cool-down is compared with field measurements at anchor TM1-4 in Figure 7-52. The predicted displacements were "corrected" to the observed value at Day 375. This plot shows that the continuum model (Model 1) fits both the shape and magnitude of the observations, while Model 3, with six fractures, also approximates the observations quite well. Model 2 (high CTE) overpredicts the contraction during cool-down, but not as badly as it overpredicted the expansion during the first 100 days.

MPBX holes NM1 and WM1 were located close to the bottom of the block and in orthogonal directions. Measured and predicted displacements for Anchor NM1-4 are plotted in Figure 7-53. At this location, Model 3 provides the best match to the observations. Model 2 overpredicts displacement by nearly a factor of 2, while the continuum model (Model 1) underpredicts the deformation. Models 1, 3, 4 and 5 bracket the observed values, with Model 1 underpredicting for the first 100 days and Models 4 and 5 overpredicting at Day 100. This plot indicates that adding one fracture (Model 4) caused more displacement at this location, but adding many fractures (Model 5) caused underprediction during the first 25 days and overprediction after Day 25.

Results for NM1-4 during cool-down are shown in Figure 7-54. Again, the data have been "corrected" to fit the observed value at Day 375. The correction for NM1-4 was different than the others because the field data were also shifted to avoid a negative displacement at the end of the test. At this location, Model 3 (low CTE) matches the magnitude of the displacement but does not accurately predict the cooling path. Model 2 (high CTE) overpredicts the displacement and best approximates the slope of the curve during the first 20 days of cooling. Models 1, 4, and 5 underpredict the amount of recovery during cool-down. The least contraction is predicted by Model 5, the highly fractured rock mass.

Data and predictions for the first 100 days of heating for WM1 are shown in Figure 7-55. This plot shows similar results to Figure 7-53 in that Model 2 overpredicts by nearly a factor of 2, and Models 1, 3, 4 and 5 bracket the behavior. The highly fractured model (Model 5) best approximates the response during the first 20 days, Models 3 and 4 overpredict the displacement during the first 10 days, but are within about 0.05 mm of the observed displacement at Day 100. Model 1 underpredicts the displacement by between 0.1 and 0.15 mm throughout this time interval.

Modeling results for WM1 during the cool-down period are shown in Figure 7-56. The cool-down simulations have again been "corrected" to the observed value at Day 375, as only relative displacements can be determined. These results are similar to those for NM1-4 in that the continuum model (Model 1) most closely approximates the observed cool-down. The high CTE model (Model 2) overpredicts the deformation, while the other models underpredict the displacement. Interestingly, these results show that adding fractures to the model causes less recovery during cool-down. This suggests fracture slip is essentially unrecoverable under unconfined stress conditions.

Figure 7-57 presents simulated and observed displacements for borehole NM2 that was located near the heater plane. This figure shows that the continuum model (Model 1) underpredicts the displacement for anchor NM2-4, while the high CTE model (Model 2) predicts the deformation relatively well during the first 10 days, but overpredicts the magnitude of the total deformation at Day 40 by nearly a factor of 2. Models 3, 4 and 5 produce similar results, and both Models 4 and 5 cross over the observed deformation at Day 40. Of these three models, Model 5 provides the best fit to the data for the first 40 days, indicating that rock in this region is highly fractured. It would be safer not to conclude anything from the NM2 data. Model 5 does a nice job of fitting the WM1-4 data during the first 25 days, but it could be argued that Model 1 fits the WM1 data just as well by Day 100.

The MPBX instrumentation in borehole WM2 functioned throughout the test, and data for anchor WM2-4 are shown along with simulated displacements for the entire test in Figure 7-58. This figure shows that, for this anchor, Models 3 and 4 did a very good job of predicting the deformation over much of the test duration. Model 3 predicts slightly less displacement than Model 4, and from Day 50 to Day 100 Model 4 is closer to the observations, while from Day 120 to Day 220 Model 3 fits slightly better. Models 3 and 4 also capture the cool-down relatively well. They underpredict the total amount of cool-down, by 0.4 mm, and also show some contraction of the block about Day 270 that is not reflected by the observation. Models 1 and 5 both underpredict maximum deformation by significant amounts (1.6 and 1 mm respectively). Model 2 overpredicts the maximum deformation but does show the best fit to the displacements during the first 20 days of heating. Model 5 does not show contraction with cool-down, and Model 1 underpredicts the magnitude of the cool-down displacement. Model 2 correctly predicts the relative change in displacement during cool-down (1.8mm), but the final value of 2.6 mm of displacement is too high.

Continuous data are also available for borehole NM3, anchor NM3-4, and these data are shown with the model predictions in Figure 7-59. It is important to note that the fracture intersected borehole NM3 at a high angle near the north face of the block. This borehole is the highest horizontal MPBX borehole in the block. This figure shows that while the measured displacement for NM3-4 is similar to that for WM2-4 (maximum between 2.5 and 3mm), all of the models underpredict the measurement. This is considerably different from the other comparisons. This figure show that adding one fracture to Model 3 to create Model 4 did increase the displacement at this location, but the increase was only a small fraction of the amount needed to compare well with the observed displacement. As expected, the continuum calculation Model 1 produced values similar to those predicted for WM2-4. The low displacement for this anchor indicates that Models 3 and 4 are missing one more key fractures. Moreover, the highly fractured Model 5 predicts less deformation than Model 4, indicating that different fractures make significantly different contributions to the deformation. This indicates that in the simulation, this portion of the block behaved more like a continuum, while the actual block response was that of a fractured medium. (While adding 21 fractures hurt the fit, having no fractures didn't help either.) The continuum model shows the least deformation.

The results discussed above indicate that Models 3 and 4 provide the best overall fits to the observations. Model 1 fits the results at the bottom of the block relatively well, and this is consistent with the results of Blair and Wood (1998), who compared observed MPBX displacements with the continuum model simulations discussed in Section 3.5.3. These authors concluded that the block could be modeled as a continuum below the heater plane, but not in the region above the heaters.

The difference between the measured and predicted deformation during the first 50 days of heating is of interest because it relates to the transient response of the rock to the temperature field. Figures 7-53 and 7-55 show that for horizontal boreholes near the base of the block, deformation in Models 3 and 4 lead the observed displacements during the first 20 days. Figures 7-57, 7-58, and 7-59 show that the observed deformation leads the predictions during the first 40 to 60 days of heating. Predicted and observed results for Anchor WM2-4 for the first 100 days of heating are replotted in Figure 7-60 along with temperature data for the plane of the heater (TT1-14) and the plane of WM2 (TT1-22) respectively. This figure shows that the observed

deformation can be correlated with temperature at the heaters. However, Figure 7-60 also shows that the predicted deformation is correlated with temperature at the borehole location, at least for the first 30 days.

The correlation with heater temperature is consistent with the behavior of many of the fracture monitors discussed in Section 7.1.2. This indicates that movement of the rock above the heater plane is due to a far-field effect, and may imply that movement along fractures serves to propagate deformation.

7.3 POST-TEST ANALYSIS

7.3.1 Introduction

This section presents ultrasonic velocity, uniaxial compressive strength, and elastic moduli measurements on two suites of core samples (pre-test and post-test), taken from the large block. During field testing, the large block was heated internally to a peak temperature of 140°C over a period of several months (Lin et al. 1997). The heating was accomplished with 2.4-m-long, 300-W heaters emplaced in five 3.8-cm-diameter horizontal boreholes at the 2.75-m level of the block. Elevated temperatures and high thermal gradients may have induced grain boundary scale microcracks in the tuff, particularly near the borehole heaters where conditions were most extreme. Thermal microcracking would contribute to the mechanical degradation of the rock, leading to a loss of strength and a reduction in elastic modulus. A loss of mechanical strength in the rock surrounding emplacement drifts would have adverse consequences for repository performance. The purpose of this work was to ascertain if measurable mechanical degradation did result around at least one of the heater boreholes during the LBT. Two suites of samples were collected. One suite, consisting of cores from one of the heater boreholes, was never exposed to elevated temperatures and will be termed the "pre-test" suite. The other suite, from overcore of the same borehole, experienced the highest temperatures and thermal gradients attained during the LBT and will be termed the "post-test" suite.

7.3.2 Methods

7.3.2.1 Sample Selection and Preparation

Two sample suites were collected from large block cores stored in the YMP Sample Management Facility at the Nevada Test Site. The pre-test suite consists of 11 cores taken from heater borehole UE-25 EH4. Borehole UE-25 EH4 was one of five horizontal heater holes emplaced at the 2.75-m level from the top of the large block. The second post-test suite consists of 12 subcores from UE25 FR PTC OC#1, a 25.4-cm-diameter overcore of borehole UE-25 EH4. The overcore samples were taken within 80 mm of heater borehole UE-25 EH4, and each should have experienced essentially the same thermal history, including the peak temperature of 140°C. All samples have the same axial orientation, since the overcore was taken parallel to the heater hole. Any preexisting anisotropy in rock strength or elastic properties should therefore be consistent for both sets of samples. Two views of the post-test coring activities are given in Figures 7-61 and 7-62.

The test specimens were prepared following ASTM standard procedures (ASTM 1997a). A 3:1 height-to-diameter ratio was chosen to be consistent with Blair, Berge et al. (1996). Because the

heater core was only 21 mm in diameter, the pre-test specimens were cut to a length of 63.5 mm. The post-test overcore specimens were prepared from 25-mm-diameter cores and were therefore cut to a length of 76.2 mm. The cores were visually inspected during specimen preparation, and all specimens having visible fractures were rejected. The specimen ends were ground flat and parallel to 0.02 mm using a precision grinder. The specimens were stored under a partial vacuum for over two weeks, then vented with dry nitrogen gas. The dry specimens were weighed with a calibrated Mettler AE240 mass balance, and their dimensions were measured with digital calipers. Densities were calculated by dividing mass by volume. The mean dry density for the pre-test and post-test samples are 2.281±0.014 and 2.285±0.014 g/cc respectively. They are statistically the same; no thermal fracturing effect is evident in the density data.

7.3.2.2. Ultrasonic Velocity Measurements

Travel time of ultrasonic waves were measured using standard through-transmission techniques consistent with ASTM guidelines (ASTM 1997b). The ultrasonic system was checked, prior to the measurements on the tuff specimens, by measuring compressional and shear wave travel times through an aluminum reference standard. Input signals were supplied by a Panametrics model 5058PR pulse-generator with the input voltage set to 200 V. Matched pairs of Panasonics transducers, model V114 (1.0 MHz) for compressional and model V155 (5.0 MHz) for shear waves, served as transmitters and receivers. Honey was used as the transducer couplant. The received signals were amplified 40 dB with a Panametrics 5660B pre-amplifier and digitized at 10-bit resolution with a LeCroy 9430 150-MHz digital oscilloscope. The travel times were manually picked on the oscilloscope screen. All of the travel-time measurements were performed twice as a simple check on data integrity. Three digitized waveforms, one compressional and two shear, were stored on the hard drive of a Mac IIcx for each specimen. Shear waveforms were recorded for two orientations, one parallel and the other orthogonal, to the sample scribe line.

The measured travel times were imported into an Excel spreadsheet, and velocities were calculated by dividing specimen lengths by travel time. Dynamic Young's modulus, E, was calculated as:

$$E = [\rho V_p^2 (3V_p^2 - 4V_s^2)]/(V_p^2 - V_s^2) \qquad \text{(Eq. 7-7)}$$

and dynamic Poisson's ratio, ν, as:

$$\nu = (V_p^2 - 2V_s^2)/[2(V_p^2 - V_s^2)] \qquad \text{(Eq. 7-8)}$$

where ρ is density, V_p is compressional velocity, and V_s is shear velocity. Two moduli are sufficient to characterize fully the elastic properties of an isotropic material but are insufficient for an anisotropic material, for which additional velocity measurements at different angles are required. Because the degree of anisotropy is not known for the sample specimens, the calculated moduli should be regarded as a potential indicator of fracture damage in the specimens rather than as an estimate of the material elastic properties.

7.3.2.3 Compressive Strength Tests

The compressive strength test procedures followed ASTM guidelines (ASTM 1997c). The specimens were tested in the same 100-ton-capacity loading frame used by Blair, Kelly, et al. (1996b). A 50-ton Enerpac hydraulic ram mounted at the base of the reaction frame supplied the axial load. Hydraulic oil was supplied to the ram through a metered valve to control the loading rate. Several trials were performed with an aluminum test piece to determine the proper valve setting for a nominal strain rate of 10^{-5} s^{-1}. The test assembly consisted of a hemispherical swivel platen at the sample base, the test specimen, and two flat-top platens. The platens were 25.4 mm in diameter. Each test specimen was positioned in the loading column using two aluminum alignment fixtures. After a small load was applied, the operator checked the alignment of the loading column and repositioned the specimen if necessary. The fixtures were removed before each test.

The load was measured with a 55,000-lb spool type strain-gauged load cell for the first five tests (specimens OC-877-01 to OC-877-05). This load cell was damaged at the end of the fifth test and replaced with a similar, 80,000-lb load cell. The load cell sensitivities are 4.42 mV/V/lb and 3.03 mV/V/lb, respectively. Both load cells were calibrated by Bechtel Nevada one month prior to the compressive strength tests. The difference in load cell sensitivity is of little significance, particularly in comparison to the heterogeneity of the sample materials. A constant 10-V DC excitation voltage was provided to the load cell by a Hewlett Packard 6205C power supply. Vertical displacement of the loading ram piston was measured with two Bourns model 80294 LVDTs mounted to the loading frame. The LVDTs were excited with constant 10-V DC power. The ambient temperature was measured during the tests with an Omega type J thermocouple.

The data acquisition system was controlled by a National Instruments (NI) LabVIEW version 4.1 software program on a Dell XPS D266 personal computer. Data were recorded at one-second intervals during the tests and included room temperature, the load cell and LVDT excitation voltages, load cell output voltage, and LVDT output voltages. The signal lead wires were attached to NI model 1303 terminal boards, configured to read the input voltages in differential mode. Signal amplification and multiplexing were performed under software control by two NI SCXI 1100 modules in an NI 1000 chassis. The input signals were digitized with an NI PCI-MIO-16XE-50 16-bit data acquisition board and stored along with a time stamp on the hard drive of the Dell computer.

After the tests, the time, ambient temperature and output voltages were imported into an Excel spreadsheet. The load cell output voltages were converted to axial load using sensitivity and voltage offset values given on the calibration sheets supplied by Bechtel Nevada. Axial stress was calculated by dividing axial load by the specimen's initial cross-sectional area. No correction was made for the very small change in specimen diameter with loading. The LVDT voltages were converted to centimeters of displacement using sensitivity factors derived from the LVDT calibrations, then converted to strains by dividing by the specimen length. Specimen strain rates were calculated by dividing incremental strains by the sampling interval. Young's modulus was calculated as the slope of the tangent line to the axial stress-strain curve at half the measured compressive strength, following standard ASTM procedures (ASTM 1997). A standard stress-strain plot was produced for each specimen. Two representative stress-strain plots are given in Figure 7-63.

7.3.3 Results

Compressional and shear velocities and calculated dynamic moduli are given for pre-test and post-test specimens in Tables 7-9 and 7-10 and are plotted as histograms in Figures 7-64 and 7-65. The average compressional and shear velocities are nearly identical for both sample suites. The average compressional velocities of the post-test and pre-test cores are 4.86 ± 0.05 km/s and 4.87 ± 0.04 km/s, respectively. The average shear velocities of the post-test and pre-test cores

Table 7-9 Pre-test Specimen Densities, Velocities, and Dynamic Moduli

Specimen	Density	P Velocity	S Velocity	Young's modulus	Poisson's ratio
	(g/cm^3)	(km/s)	(km/s)	(GPa)	
HC-071-05	2.290	4.83	3.27	52.7	0.08
HC-072-12	2.271	4.84	3.19	51.5	0.12
HC-074-26	2.308	4.88	3.25	53.6	0.10
HC-075-44	2.258	4.80	3.14	50.1	0.13
HC-075-47	2.274	4.80	3.23	51.5	0.09
HC-076-61	2.299	4.75	3.22	51.3	0.08
HC-076-65	2.255	4.80	3.18	50.5	0.11
HC-077-77	2.272	4.81	3.21	51.5	0.10
HC-077-80	2.290	4.87	3.21	52.7	0.11
HC-077-83	2.276	4.77	3.18	50.6	0.10
HC-077-87	2.272	4.81	3.23	51.6	0.09
HC-077-89	2.285	4.82	3.25	52.2	0.08
mean	2.279	4.81	3.21	51.6	0.10
std. dev.	0.015	0.04	0.04	0.97	0.02

Table 7-10 Post-test Specimen Densities, Velocities, and Dynamic Moduli

Specimen	Density	P Velocity	S Velocity	Young's modulus	Poisson's ratio
	(g/cm^3)	(km/s)	(km/s)	(GPa)	
OC-877-01	2.265	4.88	3.29	53.2	0.08
OC-877-02	2.287	4.84	3.21	52.1	0.11
OC-877-03	2.293	4.87	3.24	53.1	0.10
OC-877-04	2.307	4.83	3.20	52.4	0.11
OC-877-05	2.291	4.89	3.22	53.0	0.12
OC-877-06	2.269	4.84	3.15	50.9	0.13
OC-877-07	2.293	4.80	3.18	51.4	0.11
OC-877-08	2.284	4.81	3.20	51.6	0.10
OC-877-09	2.263	4.77	3.12	49.6	0.12
OC-874A-06	2.298	4.93	3.15	52.7	0.16
OC-874B-01	2.269	4.87	3.22	52.4	0.11
OC-874B-02	2.302	4.93	3.18	53.2	0.15
mean	2.285	4.86	3.20	52.1	0.12
std. dev.	0.014	0.05	0.05	01.05	0.02

Table 7-11 Pre-test Specimen Strain Rates and Static Mechanical Properties

Specimen	Strain rate ($x10^6$ s^{-1})	Compressive strength (MPa)	Axial strain at failure ($x10^3$)	Young's modulus (GPa)
HC-071-05	14.6	156.2	10.1	24.0
HC-072-12	13.7	115.3	6.75	25.1
HC-074-26	14.7	206.4	9.27	30.4
HC-075-44	13.5	132.5	4.83	26.7
HC-075-47	16.6	142.2	4.58	28.8
HC-076-61	15.7	200.4	7.93	25.0
HC-077-77	18.3	105.5	6.30	19.5
HC-077-80	12.1	149.3	7.79	24.9
HC-077-83	12.3	139.6	8.69	26.3
HC-077-87	21.2	198.0	8.38	25.4
HC-077-89	23.5	201.0	8.96	25.6
mean	16.0	158.8	7.6	25.6
std. dev.	3.48	36.71	1.71	2.75

Table 7-12. Post-test Specimen Strain Rates and Static Mechanical Properties

Specimen	Strain rate ($x10^6$ s^{-1})	Compressive strength (MPa)	Axial strain at failure ($x10^3$)	Young's modulus (GPa)
OC-877-01	7.3	197.3	9.22	34.4
OC-877-02	7.3	223.6	11.4	30.4
OC-877-03	5.6	266.7	7.51	35.4
OC-877-04	9.5	198.0	7.37	35.4
OC-877-05	9.8	207.0	7.26	33.1
OC-877-06	12.0	114.0	4.83	26.3
OC-877-07	14.5	158.8	6.43	26.4
OC-877-08	11.1	150.5	5.75	27.8
OC-877-09	14.2	145.1	6.48	25.5
OC-874A-06	7.3	207.6	8.43	24.7
OC-874B-01	9.9	178.6	7.32	26.2
OC-874B-02	10.0	145.8	6.84	32.4
mean	9.7	182.7	7.40	29.8
standard dev.	2.6	42.11	1.63	3.94

are 3.20 ± 0.05 km/s and 3.21 ± 0.04 km/s, respectively. Neither velocity difference is statistically significant. Mean elastic moduli also differ by less than one standard deviation. The calculated average Young's moduli are 51.7 ± 0.97 GPa and 52.15 ± 1.05 GPa for the pre-test and post-test cores respectively. The average Poisson's ratios are 0.10 ± 0.02 and 0.12 ± 0.02 for the pre-heat and post-test cores respectively.

Most of the stress-strain plots were fairly linear to failure, and all but one of the test specimens failed at an axial stress over 100 MPa. Compressive strength results are given in Tables 7-11 and 7-12 and are plotted as histograms in Figure 7-66. Because of the failure of the 55,000-lb load cell, the data of the first five specimens in Table 7-12 should be treated as non-Q and, therefore, for reference only. The mean compressive strength for all 11 pre-test samples is 158.8 ± 36.7 MPa. The mean compressive strength for the post-test samples is 182.8 ± 42.1 MPa, or 157.1 ± 29.4 MPa if the first five samples in Table 7-12 are not included. The compressive strengths of the pre-test and the post-test cores are statistically the same.

Calculated static Young's moduli are included in Tables 7-11 and 7-12 and are plotted as histograms in Figure 7-67. Average static Young's moduli of 25.6 ± 3.9 GPa and 29.8 ± 2.7 GPa were calculated for the pre-test and post-test specimens, respectively. The average Young's modulus of the last seven post-test samples in Table 12 is 2.70 ± 2.5 MPa. The Young's modulus of the pre-test and the post-test samples are statistically the same.

7.3.4 Discussion

Our results indicate no statistically significant differences in dry density, ultrasonic compressional and shear velocities, or compressive strength between the thermally cycled post-test and the nonthermally cycled pre-test cores. The post-test samples appear to be stiffer than the pre-test samples by about one standard deviation. However, thermally induced cracking is expected to make the rock more, rather than less, compliant, so the difference is likely the result of pre-existing sample heterogeneity. The dynamic Young's moduli calculated from the velocity measurements are considerably larger than the static Young's moduli determined from the stress-strain curves, as is generally the case for rocks under low confining pressures.

Uniaxial compressive strength and elastic wave velocities for Topopah Spring tuff have been measured previously by others. In general, our results are similar to those obtained in the earlier studies, which further suggests that the LBT thermal cycle did little to damage these rocks. Summing up a number of the earlier tests on tuff specimens from the proposed repository horizon, Wilder (1993) concluded that "these data indicate that the intact rock is quite strong, with a uniaxial strength of 155 ± 59 MPa and a high Young's modulus." Although there is clearly a lot of scatter in the data, our compressive strength results for the thermally cycled post-test specimens (183 ± 42 MPa) are at least on the high side of the range. If the data of the first five specimens in Table 7-12 are not considered, our mean compressive strength of the overcore specimens (157.1 ± 29.4 MPa) agrees well with the previous results. More recently, Martin et al. (1993) have performed ultrasonic velocity and uniaxial compressive strength measurements on six Topopah Spring tuff specimens. Their strength data are not comparable to ours because they used a much slower loading rate (10^{-9}/s), but the velocity data are comparable. Their compressional velocities, measured on dry specimens, averaged 4.59 km/s, about 5% lower than our results.

Our compressive strength tests were designed to be similar to those of Blair, Kelly, et al. (1996). The same length-to-diameter ratio (3:1) and nominal loading rate were used. Specimen preparation procedures were similar. The loading frame and much of the other testing equipment were the same. Blair, Kelly, et al. (1996) tested two groups of 15 samples: an irradiated group and a control group. They found mean compressive strengths of 139 ± 73 MPa for the irradiated

group and 154 ± 36 MPa for the control group. Our compressive strength values of 158 ± 37 MPa for the pre-test samples and 183 ± 42 MPa for post-test samples are in very good agreement with their results (Figure 7-68). Our Young's modulus values, 25 ± 3 GPa for the pre-test core and 30 ± 5 GPa for post-test core, are similar to values obtained by Blair, Kelly, et al. (1996) and to values contained in the YMP Reference Information Base (DOE 1990), as shown in Figure 7-69.

7.3.5 Conclusions

No statistically significant differences in dry density, ultrasonic velocity, compressive strength, or Young's modulus were observed between the thermally cycled post-test and nonthermally cycled pre-test suites. The dry densities, ultrasonic velocities, uniaxial compressive strengths, and elastic moduli obtained for these specimens are also similar to those obtained for Topopah Spring tuff in other laboratory studies. No evidence was found that the tuff specimens were damaged in the LBT.